CHANNEL MODELING AND CHARACTERIZATION FOR VISIBLE LIGHT COMMUNICATIONS: INDOOR, VEHICULAR AND UNDERWATER CHANNELS

A Dissertation

by

Farshad Miramirkhani

Submitted to the

Graduate School of Sciences and Engineering
In Partial Fulfillment of the Requirements for
the Degree of

Doctor of Philosophy

in the
Department of Electrical and Electronics Engineering

Ozyegin University
June 2018

CHANNEL MODELING AND CHARACTERIZATION FOR VISIBLE LIGHT COMMUNICATIONS: INDOOR, VEHICULAR AND UNDERWATER CHANNELS

Approved by:

Professor Murat Uysal, Advisor,
Department of Electrical and Electronics Engineering
Ozyegin University

Associate Professor Fatih Ugurdag,
Department of Electrical and Electronics Engineering
Ozyegin University

Assistant Professor Ahmet Tekin,
Department of Electrical and Electronics Engineering
Ozyegin University

Assistant Professor Tuncer Baykas,
Department of Computer Science and Engineering
Istanbul Medipol University

Associate Professor Ertugrul Basar,
Department of Electronics and Communication Engineering
Istanbul Technical University

Date Approved: 15 May 2018

To

(My wife and parents for their love, endless support and encouragement)

ABSTRACT

Despite the increasing attention on visible light communications (VLC) systems, there is a lack of proper visible light (VL) channel models. This is a serious concern since channel modeling is the very first step for efficient, reliable, and robust VLC system design. This dissertation focuses on channel modeling and characterization study for indoor, vehicular and underwater VLC. Our study is based on Zemax®; a commercial optical and illumination design software. Although the main purpose of such software is optical system design, we take advantage of the ray tracing features of this software which allows an accurate description of the interaction of rays emitted from the lighting source within a specified confined space. The simulation environment is created in Zemax® and enables us to specify the geometry of the environment, the objects within as well as the specifications of the sources (i.e., LEDs) and receivers (i.e., photodiodes). For a given number of rays and the number of reflections, the non-sequential ray tracing tool calculates the detected power and path lengths from source to detector for each ray. These are then imported to Matlab® and processed to yield the channel impulse response (CIR). In contrary to existing works which are mainly limited to ideal Lambertian sources and purely diffuse reflections, our approach is capable to obtain CIRs for any non-ideal sources as well as specular and mixed specular-diffuse reflections. Furthermore, we can precisely reflect the presence of objects and wavelength-dependent reflection characteristics of surface materials in channel study.

In the first part of this thesis, we propose a realistic indoor channel modeling approach and carry out a detailed channel characterization study. We also investigate the effect of user mobility and receiver orientation on CIRs. In the second part of this thesis, we present VLC channel models for vehicle-to-vehicle (V2V) and vehicle-to-infrastructure (V2I) taking into account the asymmetrical pattern of headlamp and street lights, reflections from road surfaces and weather conditions. We further develop a closed-form path loss expression for V2V VLC channel for different weather conditions. In the last part of this thesis, we carry out a detailed underwater optical channel modeling and characterization study taking into account the reflection characteristics of the sea surface and sea bottom as well as the water characteristics, i.e., extinction coefficient, and scattering phase function of particles. We develop a closed-form path loss expression as an explicit function of water type, beam divergence angle and receiver aperture diameter and validate the accuracy of the proposed expression through Monte Carlo simulation results.

ÖZET

Görünür ışık haberleşmesi (visible light communication-VLC) sistemlerine olan artan ilgiye ragmen, uygun görününür ışık (visible light-VL) kanal modelleri eksikliği mevcuttur. Verimli, güvenilir ve dirençli VLC sistem tasarımı için ilk adım kanal modelleme olduğundan, bu eksiklik ciddi bir sorundur. Bu tezin odağı, içmekan, taşıtlara ilişkin, ve sualtı VLC için kanal modelleme ve nitelendirme çalışmalarıdır. Çalışmamız, ticari bir optik ve aydınlatma tasarımı yazılımı olan Zemax® tabanlıdır. Bu yazılımın ana amacı optik sistem tasarımı olmasına ragmen, biz bu yazılımın, belirli bir kapalı alanda, bir aydınlatma kaynağından yayılmış olan ışınların etkileşimlerini hassas bir şekilde tarif eden, ışın takibi özelliklerinden faydalanıyoruz. Zemax®'te oluşturulan simülasyon ortamı, ortamın geometrisini, ortamda bulunan nesneleri, ve ayrıca kaynakların (yani LEDler) ve alıcıların (yani fotodiyotlar) teknik özelliklerini nitelendirmemize imkan tanımaktadır. Belirli bir sayıda ışın ve yansıma sayısı için, ardışık olmayan ışın takibi aracı, her ışın için saptanan gücü ve kaynaktan detektöre olan yol uzunluğunu hesaplar. Bu veriler daha sonra Matlab®'e aktarılır ve kanal dürtü yanıtlarını (channel impulse response-CIR) elde etmek üzere işlenir. Genel olarak ideal Lambertian kaynaklar ve sadece dağınık yansımalar ile sınırlı olan mevcut çalışmaların aksine, bizim yaklaşımımız, herhangi bir ideal olmayan kaynak, ve ayrıca dik açılı ve dik açılı-dağınık karışık yansımalar için de kanal dürtü yanıtlarını elde edebilmektedir. Dahası, ortamda nesnelerin mevcudiyetini ve dalgaboyuna bağımlı yansıma karakteristiklerini de kanal çalışmasına yansıtabilmekteyiz.

Bu tezin ilk kısmında, gerçekçi bir içmekan kanal modelleme yaklaşımı sunuyor ve detaylı bir kanal niteleme çalışması yürütüyoruz. Aynı zamanda kullanıcı hareketliliği ve alıcının baktığı yönün CIRlar üzerindeki etkisini de araştırıyoruz. Tezin ikinci kısımda, farların ve sokak lambalarının asimetrik modellerini, yol yüzeyinden yansımaları ve hava koşullarını da dikkate alarak araçtan araca (vehicle-to-vehicle–V2V) ve araçtan altyapıya (vehicle-to-infrastructure–V2I) VLC kanal modellerini sunuyoruz. Ayrıca, farklı hava koşullarında V2V VLC kanalı için kapalı yapıda bir yol kaybı ifadesi ortaya koyuyoruz. Bu tezin son kısmında, deniz yüzeyinin ve tabanının yansıtma karakteristiklerini, ve ayrıca suyun karakteristiklerini (yani, sönüm katsayısı, ve parçacıkların saçılım faz fonksiyonu) de hesaba katarak, detaylı bir sualtı optik kanal modelleme ve nitelendirme çalışması yürütüyoruz. Yol kaybının, su tipine, ışın demeti sapma açısına, ve alıcı açıklığı çapına bağlı bir fonksiyon olan kapalı yapıda bir ifadesini geliştiriyor ve ortaya konan bu ifadenin doğrulunu Monte Carlo simülasyon sonuçları ile onaylıyoruz.

ACKNOWLEDGMENTS

I would like to thank my supervisor, Prof. Murat Uysal, for the patient guidance, encouragement and the invaluable insights and suggestions he has provided throughout my time as his Ph.D. student. I have been extremely lucky to have a supervisor who cared so much about my work, and who responded to my questions and queries so promptly. I will never forget his support and for providing me numerous opportunities to learn and develop as a researcher. I will continue to be influenced by his rigorous scholarship, clarity in thinking, and professional integrity. My sincere gratitude is also reserved for Prof. Erdal Panayirci who has been much more than a professor to me.

I am truly grateful to the members of my dissertation committee, Dr. Fatih Ugurdag, Dr. Ahmet Tekin, Dr. Tuncer Baykas and Dr. Ertugrul Basar for their time serving on my committee and carefully reviewing my dissertation.

I must express my gratitude to Niloofar, my wife, for her continued support and encouragement. She experienced all of the ups and downs of my research and has been a constant source of inspiration, without which I would not have come this far.

Last, but not least, I would like to thank to my mother and father, for their love and encouragement. Words cannot express the feelings I have for my parents for their constant unconditional support, both emotionally and financially.

TABLE OF CONTENTS

LIST OF TABLES

LIST OF FIGURES

CHAPTER I

INTRODUCTION

1.1 Motivation

The demand for high-speed and ubiquitous broadband wireless access has spurred an immense growth in mobile data traffic. The increasing number of smart devices in different form factors and capabilities combined with the worldwide adoption of social media and advanced multimedia applications are the primary contributors to this growth. Recent market analysis [1] reports that the global mobile data traffic is up 63% in 2016 and will increase sevenfold between 2016 and 2021.

The design of future wireless communication networks that cope with the ever growing mobile data traffic is recognized as a major technical challenge that wireless engineers face today. To address the needs of future wireless networks, various solutions are currently being discussed and proposed [2]. One particular solution is network densification that allows the same spectrum to be spatially reused. While densification through the use of small cells brings significant capacity, interference eventually imposes a fundamental limit. Through advances in physical layer design, such as massive multiple-input multiple-output techniques, some improvements in spectral efficiency are also possible. Regardless of the efficacy of network densification and potential spectral efficiency gains, much more bandwidth is required to cope with the predicted data traffic growth. This can be achieved by moving up to higher carrier frequencies. Current wireless access systems (cellular, WiFi) mostly work in the radio

frequency (RF) band below 6 GHz. However, this spectral band is almost fully occupied and heavily regulated. In an effort to yield more bandwidth, ongoing research efforts focus on the upper segments of the RF band with a particular emphasis on millimeter frequencies up to 300 GHz.

A more radical approach to address the shortcomings of current wireless access systems is to deploy optical bands. In particular, the expected wide scale availability of light emitting diodes (LEDs) in the near future opens the door for so-called visible light communication (VLC) [3]. VLC is based on the principle of modulating LEDs at very high speeds that are not noticeable by human eye. This lets the use of LEDs for wireless communication purposes in addition to their primary purpose of illumination. VLC operates at unlicensed optical bands and offers a large bandwidth capacity. Therefore, VLC can be utilized as a complementary wireless access technology where excess capacity demands of cellular or WiFi networks can be offloaded.

In addition to indoor illumination, LEDs are increasingly deployed for outdoor applications, particularly for exterior automative lightning. VLC is therefore considered a potential means for vehicular connectivity [4-6]. The current research activities and standardization efforts on vehicle-to-vehicle (V2V), vehicle-to-infrastructure (V2I) and infrastructure-to-vehicle (I2V) communications have mainly focused on the use of RF technologies [7-9]. The impact of current V2V and V2I communications on the RF spectrum usages is low, but this is expected to significantly increase in the near future with the widespread adoption of Intelligent Transportation Systems (ITSs). Limited RF bands can quickly suffer from high interference levels when hundreds of vehicles located in the same vicinity try to communicate simultaneously. Furthermore, RF-based vehicular communications experience longer delays and lower packet rate because of the channel congestion. VLC can be used a scalable and reliable wireless access

technology for vehicular networks.

Another potential usage area of VLC is underwater communication. Underwater wireless transmission can be achieved through radio, acoustic, or optical waves. Radio frequency waves suffer from significant attenuation in water, which seriously limits the transmission range to very short distances with practical antenna sizes. On the other hand, acoustic waves can support transmission ranges on the order of kilometers and become the typical choice in the commercially available underwater modems. Acoustic systems however fall short with their low data rates (kilobits per second) for emerging bandwidth-hungry underwater applications such as image and real-time video transmission. As diverse and data-heavy underwater applications emerge, VLC [10, 11] has emerged as a powerful alternative and/or complementary to acoustic counterparts.

1.2 Fundamentals of VLC Systems

VLC systems employ visible light for communication that occupy the spectrum from 380 nm to 780 nm corresponding to a frequency spectrum of 384 THz to 789 THz. Hence the physical optical principles can be applied to the VLC systems. In fact, the carrier in VLC is the visible rays used for illumination. VLC is typically characterised by a non negative and non-coherent signal transmission. It respects the communication principle in which three main parts are considered: a transmitter, a channel and a receiver.

The modulated signal, added to a DC voltage is used to power the LED, this constitutes the transmitter. The LED in its operation produces the light and at the same time, convey the information through the channel. The receiver is made of the photodetector (PD) and the demodulator. The PD detects the light and produce an electrical signal composed of the message plus noise.

In VLC systems, the transmitter groups, in one module, the data source, the modulation module and the LED. The last two elements are the very important elements in a VLC transmitter. Two types of LEDs are used in VLC systems: The single-colour LED and the multicolour LEDs. The multicolour LED groups in one package multiple single-colour LEDs. The most used multicolour LED is the red-green-blue (RGB) LED. In multi-carrier systems, each of the colour LEDs included in the package represents an antenna, corresponding to one channel. There are as many channels in the system as there are LEDs in the package. Hence, a given number of colour-LEDs will provide the same number of distinct channels. Consequently, the RGB-LED transmitter is seen as a special multichannel transmitter that can be used to deploy multicarrier modulation techniques. For example, with a single RGB-LED, a three-by-three multiple inputs-multiple outputs technique is applicable over the VLC channel.

In communication, the channel represents the space between the transmitter and the receiver. It is characterised by its ability to transmit the carrier signal, and, it is influenced by many factors such as attenuation, interference and noise. In VLC technology, the channel is the space between the LED and the PD. Two main types of channels are considered in VLC communication systems: the single VLC channel involving a single LED and a single PD, and the multichannel VLC systems in which the transmitter is made of multicolour LEDs. In this second case, the PD is made of more than one detector, each of them being sensitive to a colour from the transmitter.

The main element in the VLC receiver is the photo-detector used to collect the light radiation. Two main types of photodetectors are used in VLC receivers: the photo-diode and the phototransistors. The digital camera, consisting of an array of photo transistor is a good device for receiving VLC signal in smart devices such as smart phones and laptops. A complete receiver system made of components such as the

concentrator, the optical filter, the amplifier and the equaliser, necessary to capture the maximum light needed to convert the received signal into message. The rays pass through the concentrator and the optical filter before they reach the proper detector core.

1.3 Dissertation Outline

Despite the increasing attention on VLC systems, there is a lack of proper visible light (VL) channel models. This is a serious concern since channel modeling is the very first step for efficient, reliable, and robust VLC system design. The main objective of our work is to develop realistic VLC channel models for indoor, underwater and outdoor mediums. Our study is based on Zemax®; a commercial optical and illumination design software. Although the main purpose of such software is optical system design, we take advantage of the ray tracing features of this software which allows an accurate description of the interaction of rays emitted from the lighting source within a specified confined space.

The simulation environment is created in Zemax® and enables us to specify the geometry of the environment, the objects within as well as the specifications of the sources (i.e., LEDs) and receivers (i.e., photodiodes). For a given number of rays and the number of reflections, the non-sequential ray tracing tool calculates the detected power and path lengths from source to detector for each ray. These are then imported to Matlab® and processed to yield the channel impulse response (CIR).

In the first part of our work, we focus on indoor channel modeling. Our proposed approach is capable to obtain CIRs for any non-ideal sources unlike the earlier works building upon the use of Lambertian sources. Furthermore, diffuse, specular and mixed reflections can be easily taken into account. In addition, we can precisely reflect the presence of objects and wavelength-dependent reflection characteristics of surface

materials in channel modeling. To confirm the accuracy of our approach, we first demonstrate that our approach yields the same CIR as in the literature under the assumption of purely diffuse reflections and ideal Lambertian source. We then discuss the effect of specular and mixed cases.

As case studies, we consider various indoor environments with different transmitter specifications (i.e., single vs. multiple transmitters, array type) and receiver specifications (i.e., location, rotation). For environments under consideration, we obtain CIRs and present a channel characterization study where channel parameters such as channel DC gain, path loss, and root mean square (RMS) delay spread are obtained. We then make one-to-one comparisons between infrared (IR) and visible light CIRs for the same environments to emphasize the differences between two optical bands.

In the second part of our work, we address vehicular VLC channel modeling for ITS usage scenarios. We carefully take into account the effect of practical light sources (i.e., the asymmetrical pattern of headlamp and street lights) and operating conditions (i.e., reflections from road surfaces) as well as weather conditions in our channel modeling study. For various configurations such as vehicle-to-vehicle, traffic light-to-vehicle and street lamp-to-vehicle, we obtain CIRs and calculate channel DC gain, RMS delay spread and path loss. Furthermore, we develop a closed-form path loss expression for V2V VLC channel in different weather conditions.

In the third and final part of our work, we carry out a detailed underwater optical channel modeling and characterization study taking into account the presence of human and man-made objects such as autonomous underwater vehicle (AUV). The reflection characteristics of the sea surface and sea bottom as well as the water characteristics, i.e., extinction coefficient and scattering phase function of particles, are precisely

considered. For various underwater scenarios with different transmitter/receiver specifications (i.e., viewing angle, aperture size) and different depths from the sea surface, we obtain CIRs and calculate associated channel parameters. Based on CIRs, we further develop a closed-form path loss expression as an explicit function of water type, beam divergence angle and receiver aperture diameter.

Several of the main ideas in this dissertation have already been published by the author in the course of his research. A realistic indoor VLC channel modeling approach taking into account the practical issues such as wavelength dependency of reflection coefficients, different types of reflections (diffuse, specular and mixed cases of diffuse and specular), non-ideal Lambertian sources and higher order number of reflections is presented in [12, 13]. The channel models for four usage scenarios (i.e., workplace, office room with secondary light, living room, and manufacturing cell) considered in the IEEE 802.15.7r1 Technical Requirements Document are presented in [14-18]. These were endorsed by IEEE 802.15.7r1 as reference channel models. A mobile indoor VLC channel model is presented in [19]. A closed-form path loss expression for V2V VLC channel in different weather conditions is given in [20]. A realistic underwater VLC (UVLC) channel model taking into account the presence of human and man-made objects is presented in [21]. A closed-form UVLC path loss expression as an explicit function of water type, beam divergence angle and receiver aperture diameter is given in [22].

1.4 Organization

The rest of dissertation is organized as follows. In Chapter II, we first review the existing indoor channel modelling approaches and highlight their shortcomings. Then, we propose a VLC channel modeling approach based on non-sequantial ray tracing

features of Zemax® and present a comprehensive channel characterization study for various indoor environments. In Chapter III, we present vehicular VLC channel models for various configurations such as vehicle-to-vehicle, traffic light-to-vehicle and street lamp-to-vehicle. In Chapter IV, we focus on underwater VLC channel modeling and carry out a channel characterization study for various underwater environments. Finally Chapter V concludes and summarizes this dissertation.

CHAPTER II

CHANNEL MODELING AND CHARACTERIZATION FOR INDOOR VISIBLE LIGHT COMMUNICATIONS

2.1 Introduction

There is a rich literature on indoor infrared channel modeling based on various approaches such as recursive calculation [23-27], geometric-based models [28-32] and Monte Carlo ray tracing (MCRT) [31-34]. It should be emphasized that there exist significant differences between visible and infrared wavelengths. Therefore, the IR channel models cannot be applied to VLC channel modeling in a straightforward manner. For example, an IR source can be approximated as a monochromatic emitter while a white light LED source is inherently wideband (380 nm-780 nm). This calls for the inclusion of wavelength-dependency of source in VLC channel modeling [3, Ch. 6]. Furthermore, in IR communication, the reflectance of materials is typically modelled as a constant. On the other hand, the wavelength dependency of the reflectance of materials should be taken into consideration in the visible light spectrum. Therefore, proper modifications are needed for VLC channel modeling [35-47].

In this chapter, we first present a literature overview of the existing IR and VLC channel models. After we highlight the shortcomings of existing works, we present our VLC channel modeling approach.

2.2 Infrared Channel Modeling

2.2.1 Recursive Channel Models

The first optical wireless channel in an indoor environment was described in [23] with diffused optical radiation at a wavelength of 950 nm wavelength for a distance of up to 50 m. Within the indoor environment, various reflecting surfaces are modelled as Lambertian reflectors. The simulations in [23] are only accounted for first order reflections. A more accurate impulse response analysis was presented in [24] by considering higher order of reflections. In this method, the room surfaces (i.e., walls, floor and ceiling) are discretized into small cells. Then, a single ray from the source emits and the ray bounces are tracked until it reaches detector (see Fig. 1). For each reflection, the power and delay is calculated (i.e., CIR for that specific reflection). The overall CIR can be then obtained as summation of CIRs for all reflections as

$$\begin{aligned} h^{(k)}(t;S,R) &\approx \sum_{i=1}^{N} h^{(0)}(t;S,\varepsilon_i) \otimes h^{(k-1)}(t;\varepsilon_i,R) \\ &= \frac{n+1}{2\pi} \sum_{i=1}^{N} \frac{\rho_i \cos^n(\phi)\cos(\theta)}{d^2} \\ &\quad .\mathrm{rect}(2\theta/\pi) h^{(k-1)}\left(t - d_i/v; \{\mathbf{r},\hat{\mathbf{n}},1\}, R\right) \Delta A \end{aligned} \tag{1}$$

where k is the order of reflection; $S = \{\mathbf{r}_S, \hat{\mathbf{n}}_S, n\}$ is the arbitrary source with position of $\mathbf{r}_S$, orientation of $\hat{\mathbf{n}}_S$ and mode number of n; $R = \{\mathbf{r}_R, \hat{\mathbf{n}}_R, A_R, FOV\}$ is the arbitrary receiver with position of $\mathbf{r}_R$, orientation of $\hat{\mathbf{n}}_R$, area of A_R and field of view of FOV; ε_i is the ith small cell; ρ_i is the reflectivity of the ith small cell; ΔA is the area of small cells; N is the total number of small cells; ϕ is irradiance angle; θ is incident angle; d is the distance between source and receiver and v is the speed of light. Here, $\hat{\mathbf{n}}$ is the normal to the surface at position $\mathbf{r}$. For reflections of the order higher than

three, this model proves to be prohibitively expensive in terms of system memory requirements and total computation time.

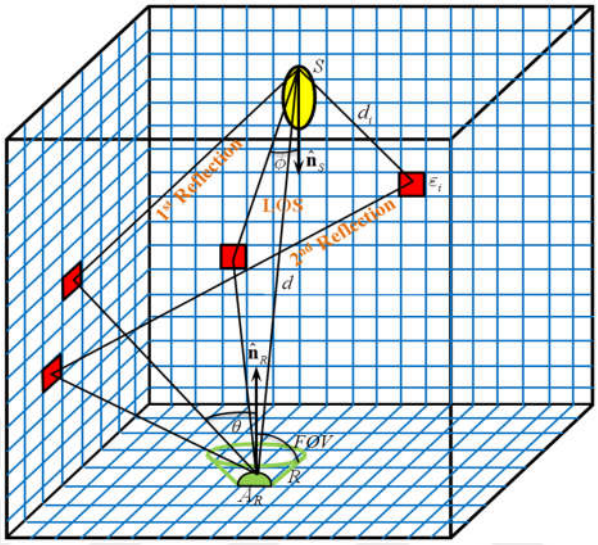

Figure 1: Recursive method

To address this issue, DUSTIN algorithm [25] was proposed which slices the impulse response into time steps rather than into the number of reflections. This approach results in reduction of both the memory requirement and the number of operations required to calculate the complete impulse response. The works in [24, 25] were however limited to empty indoor environment. The iterative site-based method [26, 27] was proposed to consider the effect of man-made objects. In this method, each piece of furniture is assumed to have a cubic rectangular shape with surface areas parallel with room walls. Objects with many different shapes can also be formed by combining a number of cubic and cubic rectangular-shaped objects.

2.2.2 Geometric-Based Channel Models

In an effort to obtain a closed form expression for the IR channel, the geometric-based channel models were proposed. The Ceiling bounce model proposed in [28] provided a closed form expression for CIR by considering diffuse reflections assuming

that the transmitter and receiver are co-located in panels parallel to the floor towards the ceiling. The geometric parameters of the room as well as the reflectance values were included. This model translates the effect of multiple reflections into loss of optical power at the receiver (i.e., path loss) and the RMS delay spread of the signal arriving at the receiver after multiple reflections. Since this model does not account for the presence of obstructions, it is not expected to be highly accurate.

In [29], the IR channel was modeled using Ulbricht's integrating sphere as a geometric-based model. The CIR in this method is defined as a combination of diffuse components and a direct LOS component. To account for complete channel response, the LOS impulse response is superimposed on the diffuse impulse response.

In [30], the received optical power with Ceiling bounce model was formulated and then compared with measurements. Since the frequency sweep method was used for the measurements, the comparison was done in frequency domain. The results presented therein demonstrated that the fluctuations of CIR in large frequencies cannot be predicted very well with Ceiling bounce model. Therefore, more accurate channel model was presented in [30] as a combination of primary reflections and higher-order reflections. The Gamma probability density function is selected as the matching function of the primary reflection impulse response and the function parameters are related to the physical parameters of the room. A spherical model is further used to calculate the CIR of higher-order reflections. It was demonstrated that the bandwidth characteristics are dominated by the response of the primary reflection rather than the higher-order reflections. It was also shown that the bandwidth depends on the radiation angle and is larger if the radiation angle is narrower.

2.2.3 MCRT Channel Models

In contrast to recursive and geometric-based methods [24-30], MCRT algorithm allows for the evaluation of the impulse response for environments with complex geometries with no meaningful increase in computational cost, especially when a large number of reflections are considered. The MCRT was first proposed in [31]. This method involves discretization of room surfaces (i.e., walls, floors, ceiling) into small cells, ray generation based on a given statistical distribution (distribution type depends on the source) and then tracking of each ray until it reaches detector to calculate the detected power and associated delay (see Fig. 2). In [31], the results obtained with MCRT were compared with those obtained through classical recursive method. It is demonstrated that higher order reflections can be considered in a reasonable simulation time while the recursive method is limited to third order reflections.

In conventional MCRT, there is no limitation on the number of reflections that can be considered. However, the probability that the rays will reach the receiver is not high, and so a very large number of rays needs to be traced. To address this issue, modified Monte Carlo (MMC) algorithm has been introduced in [32], where each reflection of the rays is used to calculate a LOS contribution to the receiver from the reflecting point, thus utilizing each ray multiple times instead of only once. This leads to a lower number of generated rays from the source to calculate an impulse response. The algorithm is purely sequential and iterative, and hence this method is very fast. However, the impulse response obtained in this way contains some variance because of the random nature of the direction of the rays. This variance decreases as the number of rays is increased.

Another important parameter in modeling of the surface materials (walls, ceiling, furniture, etc) is the type of reflections. In [32], a diffuse-to-mirror ratio (DMR) as a function of the roughness of the material depending on the incidence angle was defined, which determines the amount of the incoming power that is specularly reflected or scattered. In [33], a MCRT simulation was performed with the software tool Specter by Integra Inc. in a geometric computer-aided design (CAD) cabin model. The geometric models of the objects in the setup, the materials' reflection characteristics on the objects and the definition of key properties of light sources and detectors were defined as the input parameters. Mathematical models were then developed for LOS and NLOS path losses along particular paths, including estimation of the path loss exponent and the shadowing component. The shadowing is modelled according to a log-normal distribution.

In [34], the CIR was evaluated with combination of recursive method and MCRT which utilize the accuracy of recursive approach in addition to the speed of Monte Carlo analysis. The first order reflections contain the most significant amount of power in CIR (depending on the configurations) so they are calculated by recursive method and higher order reflections which are the limitations of recursive method, are calculated with modified Monte Carlo ray tracing (MMCRT). In this method, the room is discretized into small cells to evaluate the first order reflections by recursive method and then from each reflection point (small cells) multiple rays are generated to evaluate higher order reflections by MMCRT.

A comparison of IR channel models discussed so far is provided in Table 1.

Table 1: Comparison of existing indoor IR channel models

	Method	**Modeling of Reflectance**	**Number of Reflections**	**Other Assumptions**
[24]	Recursive	Fixed reflectance	Third order	- Purely Lambertian reflections - Empty room - Ideal Lambertian source
[25]	Recursive (DUSTIN algorithm)	Fixed reflectance	Not mentioned	- Purely Lambertian reflections - Empty room - Ideal Lambertian source
[26]	Recursive (Iterative site-based)	Fixed reflectance	Third order	- Purely Lambertian reflections - Room with objects - Ideal Lambertian source
[27]	Recursive (Iterative site-based)	Fixed reflectance	High order (>10)	- Purely Lambertian reflections - Room with objects - Ideal Lambertian source
[28]	Geometric-based (Ceiling bounce)	Fixed reflectance	First order	- Purely Lambertian reflections - Empty room - Ideal Lambertian source
[29]	Geometric-based (Sphere model)	Fixed reflectance	High order (>10)	- Purely Lambertian reflections - Empty room - Ideal Lambertian source
[30]	Geometric-based (Ceiling bounce & sphere model)	Fixed reflectance	High order (>10)	- Purely Lambertian reflections - Empty room - Ideal Lambertian source
[31]	Monte Carlo ray tracing	Fixed reflectance	High order (>10)	- Diffuse, specular and mixed reflections - Empty room - Ideal Lambertian source
[32]	Modified Monte Carlo ray tracing	Fixed reflectance	High order (>10)	- Diffuse, specular and mixed reflections - Empty room - Ideal Lambertian source
[33]	Monte Carlo ray tracing	Fixed reflectance	High order (>10)	- Diffuse, specular and mixed reflections - Cabin with objects - Ideal Lambertian source
[34]	Combined recursive & Monte Carlo ray tracing	Fixed reflectance	High order (>10)	- Purely Lambertian reflections - Empty room - Ideal Lambertian source

2.3 VLC Channel Modeling

Inspired from the IR channel models, various VLC channel modeling studies were carried out in the literature (see Table 2).

2.3.1 Recursive Channel Models

In [35], the recursive method proposed in [24] was adopted to obtain CIR in VL band, but fixed reflectance is assumed. While this can be justified for infrared wavelengths, wavelength dependency should be considered for realistic channel modeling in VLC. In [36], in an effort to reflect the effect of wavelength dependency in channel modeling, the reflectance values were calculated as the average of wavelength dependent coefficients over the VL band. In [37], the wavelength dependency explicitly was taken into account in recursive method to determine the CIR of an empty room. However, similar to [35, 36], the work in [37] was also limited to the assumptions of only purely diffuse reflections and ideal Lambertian source which might not hold true for many practical cases. In [38], a modified version of the recursive method was proposed to integrate the non-ideal Lambertian source with distinct source radiation patterns. The angular distribution of two commercial LEDs, i.e., NSPW345CS from Nichia and LUXEON Rebel from Lumileds Philips, are analytically characterized and the effect of source modeling on path loss, RMS delay spread and channel bandwidth are investigated.

In contrast to the well-known time-domain methods, a novel frequency-domain method was proposed in [39]. In this approach, the channel transfer functions of diffuse components and direct line-of-sight (LOS) component are obtained. Then, a recursive linear time-invariant (LTI) system is constructed based on all transfer functions for all the light (LOS and diffuse) that originally stems from the transmitter and that is

impinging on all surface elements. In other word, the convolutional operation of recursive method in time-domain is exchanged with multiplication of channel transfer functions in frequency-domain. This approach leads to a closed expression for the infinite sum of all contributions of arbitrarily high reflection order.

2.3.2 Geometric-Based Channel Models

Geometric-based models were also proposed for VLC channels. Particularly, in [40], analytical method with low computational complexity for calculating the non-line-of-sight (NLOS) CIR in a cuboid room was proposed. The analytical results showed that the proposed method offers very high accuracy for the dominated first order multi-path components. In [41], a field of view (FOV) geometry-based single bounce (GBSB) model for VLC channels was proposed. The simplifying assumptions of fixed reflectance values with purely diffuse reflections and ideal Lambertian source were assumed in [40, 41]. In [42], a regular-shaped geometry-based multiple bounce model (RS-GBMB) for VLC channels was proposed. The proposed model employs a combined two-ring model and ellipse model, where the received signal is constructed as a sum of the LOS, single-, double-, and triple bounced rays of different powers.

2.3.3 MCRT Channel Models

In [43], a MCRT simulation tool was proposed to obtain the CIR for VLC assuming Lambertian sources. The wavelength dependency of reflectance was taken into account. In addition, the effect of mixed diffuse and specular reflections was modeled with Phong's model. The computational efficiency of simulations are improved by first dividing the simulation environment into sub-cubes of equal size and second with parallelizing the simulation algorithm based on an equal and static distribution of the rays generated at the emitter among the available processors, i.e.,

assigning the rays to each processor by means of a uniform distribution.

Reflection model has an important impact on the channel properties, since both channel gain and multipath interference are directly affected by reflections. Therefore, the selection of the reflection model used in the channel characterization is a critical decision in order to achieve realistic and accurate channel estimation. In [44], the integration of new reflection models into MMCRT was proposed for the high-level of specular reflection components. These models are based on bidirectional reflectance distribution function (BRDF) theories, such as Blinn's or Lafortune's models, which are frequently used in 3D image rendering. The effect of different BRDF models, i.e., Lambertian's, Phong's, retroreflective Phong's and Lafortuneon's models, on the bandwidth of the VLC systems was investigated.

Table 2: Comparison of existing indoor VLC channel models

	Method	**Modeling of Reflectance**	**Number of Reflections**	**Other Assumptions**
[35]	Recursive	Fixed reflectance	Third order	- Purely Lambertian reflections - Empty room - Ideal Lambertian source
[36]	Recursive (Iterative site-based)	Averaged Reflectance	Fourth order	- Purely Lambertian reflections - Room with objects - Ideal Lambertian source
[37]	Recursive	Wavelength dependent	Third order	- Purely Lambertian reflections - Empty room - Ideal Lambertian source
[38]	Recursive	Fixed reflectance	Third order	- Purely Lambertian reflections - Empty room - Ideal Lambertian source as well as two distinct source radiation patterns
[39]	Recursive	Fixed reflectance	High order (>10)	- Purely Lambertian reflections - Empty room - Ideal Lambertian source
[40]	Geometric-based	Fixed reflectance	First order	- Purely Lambertian reflections - Empty room - Ideal Lambertian source
[41]	Geometric-based (FOV-GBSB)	Averaged Reflectance	First order	- Purely Lambertian reflections - Room with virtual scatterers - Ideal Lambertian source
[42]	Geometric-based (RS-GBMB)	Fixed reflectance	Third order	- Purely Lambertian reflections - Empty room - Ideal Lambertian source
[43]	Monte Carlo ray tracing	Wavelength dependent	High order (=10)	- Diffuse, specular and mixed reflections - Room with objects - Ideal Lambertian source
[44]	Modified Monte Carlo ray tracing	Fixed reflectance	Third order	- Diffuse, specular and mixed reflections - Empty room - Ideal Lambertian source
[45]	Photon tracing	Fixed reflectance	High order (>10)	- Diffuse, specular and mixed reflections - Room with objects - Non-ideal Lambertian source

2.4 Methodology for Indoor VLC Channel Modeling

As summarized in Table 2, majority of existing works ignore wavelength dependency of source in VLC channel modeling. Furthermore, most studies are limited to the assumption of only purely diffuse reflections and ideal Lambertian source which might not hold true for many practical cases.

In this section, we propose a realistic VLC channel modeling approach to overcome such limitations and present several CIRs for various indoor environments based on the proposed approach. Our study is based on Zemax®; a commercial optical and illumination design software [46]. Although the main purpose of such software is optical system design, we take advantage of the ray tracing features of this software which allows an accurate description of the interaction of rays emitted from the lighting source within a specified confined space.

The simulation environment is created in Zemax® and enables us to specify the geometry of the environment, the objects within as well as the specifications of the sources (i.e., LEDs) and receivers (i.e., photodiodes). For a given number of rays and the number of reflections, the non-sequential ray tracing tool calculates the detected power and path lengths from source to detector for each ray. These are then imported to Matlab® and processed to yield the CIR. Our results demonstrate that our approach yields the same CIR as in [37] under the assumption of purely diffuse reflections and ideal Lambertian source. Our approach is further capable to obtain CIRs for any other (non-ideal) source types as well as specular and mixed specular-diffuse reflections.

Fig. 2 provides an overall summary of major steps followed in the adopted channel modeling methodology [13]. In the first step, we create a three dimensional simulation environment where we can specify the geometry of the indoor environment,

the objects within, the reflection characteristics of the surface materials and the specifications of the light sources and detectors. In the second step, we use non-sequential ray tracing feature of Zemax® to calculate the detected power and path lengths from source to detector for each ray. In the third step, we import this data to Matlab® and obtain the CIRs for the environment under consideration. Further details for each step are elaborated in the following.

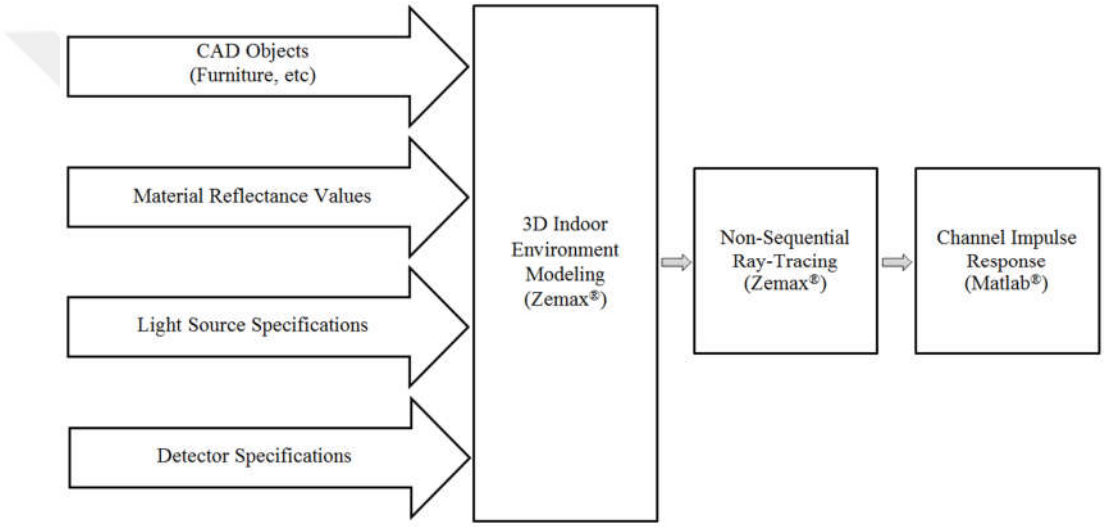

Figure 2: Steps in indoor VLC channel modeling and characterization

To model the simulation environment, we need to specify the dimensions and shape of the indoor environment, furniture and objects within, type of surface materials (coating) as well as the properties and locations of the transmitter (LED) and receiver (photodiode). The indoor environment (i.e., office room, living room, etc) is created using Zemax® "Part Designer" which is an interface that allows to create and manipulate user-defined three dimensional geometries. The CAD objects can be imported in the software to model furniture and any other objects within the indoor environment. "Table Coating Method" in the software further allows defining the wavelength-dependent reflectance of surface coating for each material [12, 13]. As

noted earlier, wavelength dependency is particularly important in VL band. To emphasize the difference characteristics between IR and VL spectral bands, reflectance values for some typical materials are presented in Fig. 3. As observed, the reflectance of most materials can be safely assumed to be a constant in IR band for most practical purposes while the wavelength dependency needs to be taken into account for VL band.

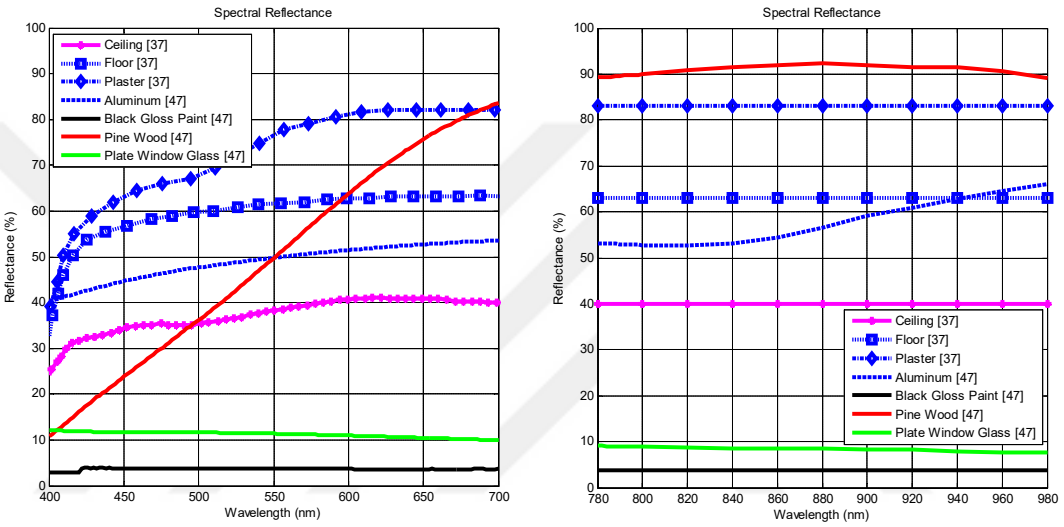

(a) (b)

Figure 3: Spectral reflectance of various materials (a) in VL band and (b) in IR band [37], [47]

Another important parameter in modeling of surface materials (walls, ceiling, furniture etc) as earlier noted is the type of reflections. As an example, Fig. 4 shows three different types where purely diffuse, specular and mixed reflections are observed. In Zemax®, we can take into account the specific type of reflection by "scatter fraction (SF)" parameter that determines the value of diffuse reflections in materials. This parameter changes between 0 and 1 such that zero indicates the purely specular reflections and unity indicates purely diffuse case.

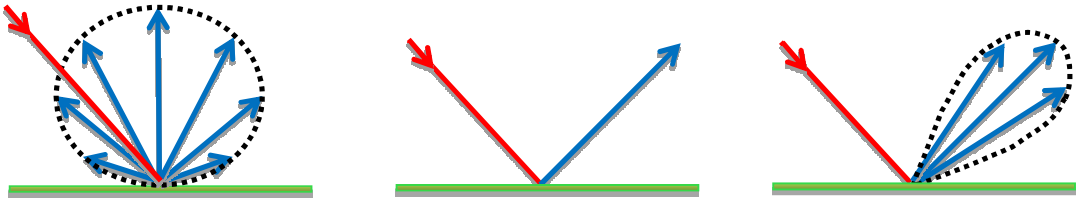

(a) (b) (c)

Figure 4: (a) Purely diffuse reflections, (b) specular reflections and (c) mixed reflections

In addition to realistic modeling of surface materials, Zemax® also allows the use of realistic light sources. Several commercially available light sources are available in Radiant Source Model (RSM) database [46]. RSM file for a light source contains the measured radiant or luminous intensity of the source as a function of wavelength, position, and angle. As such, this file can be accurately used to characterize the behavior of the light source in both near- and far-fields. As an example, Fig. 5 depicts relative power distribution of VL and IR LEDs selected from RSM database within their working wavelength range. The VL LED (see Fig. 5.a) is a Cree Xlamp® MC-E White LED with Lambertian distribution and a viewing angle of 120° [48]. The IR LED (see Fig. 5.b) is an OSRAM® SFH 4283 IR 880 nm LED with the same viewing angle and Lambertian distribution [49]. It can be observed from Fig. 5.b that the full width at half maximum (FWHM) spectral bandwidth of IR LED is approximately 75 nm. On the other hand, in Fig. 5.a shows that, unlike the IR LED, the VL LED has a large spectral bandwidth from 400-800 nm.

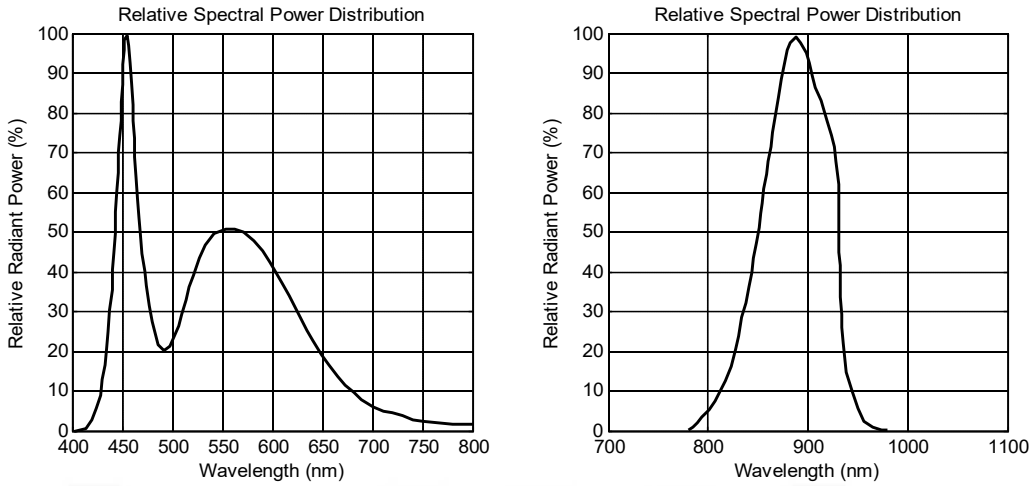

(a) (b)

Figure 5: Relative spectral power distribution of (a) Cree Xlamp® MC-E White LED and (b) OSRAM® SFH 4283 IR 880nm

In Zemax®, detectors can be modeled as planar surfaces, curved surfaces or three-dimensional volumes which store the different data types such as incoherent irradiance, coherent irradiance, coherent phase, radiant intensity, radiance and true color photometric. Moreover, the data is available in radiometric and photometric units such as watts, lumens, lux, phot and footcandles. In our simulations, we use a rectangular surface with specified dimensions as a receiving element (i.e., "Detector Rectangle" function in Zemax®).

After we create the simulation environment in Zemax®, we use its non-sequential ray tracing feature to determine the CIR. In ray tracing approach, rays are traced along a physically realizable path until they intercept an object. The LOS response is straightforward to obtain and depends upon the LOS distance. Besides the LOS component, there are a large number of reflections among ceiling, walls, and floor as well as any other objects within the environment. The way that non-sequential rays are traced depends on the source properties including polarization state, coherence

length, initial phase, position and direction of rays of light emanating from non-sequential sources. The random ray tracing methods used in Zemax® are mainly based on Monte Carlo analysis [50, 51] and Sobol sampling the latter of which is used for speeding up ray tracing [52, 53]. The main parameters in ray tracing are the number of rays (N_r) and the number of reflections (k). The number of reflections in Zemax® is adjusted through "Relative Minimum Intensity". For example, if this parameter is set to 10^{-5}, the software runs until the ratio of the intensity of last segment with respect to the first segment becomes 10^{-5}.

The non-sequential ray tracing tool generates an output file, which includes the detected power and path lengths from source to detector for each ray. We import this file to Matlab® and, using this information, we can express the CIR as

$$h(t) = \sum_{i=1}^{N_r} P_i \, \delta(t - \tau_i) \tag{2}$$

where P_i is the optical power of the ith ray, τ_i is the propagation time of the ith ray, $\delta(t)$ is the Dirac delta function and N_r is the number of rays received at the detector.

Once we obtain CIRs, we can calculate several channel parameters such as channel DC gain, path loss, RMS delay spread, mean excess delay and coherence bandwidth. Channel DC gain (H_0) is one of the most important features of a VLC channel, as it determines the achievable signal-to-noise ratio for a fixed transmitter power and is calculated as

$$H_0 = \int_{-\infty}^{\infty} h(t) \, dt \tag{3}$$

The path loss can be then expressed as

$$PL = -10\log_{10}\left(\int_0^{\infty} h(t)\,dt\right). \tag{4}$$

The time dispersion parameters of channel, RMS delay spread and mean excess delay, are respectively given by [13]

$$\tau_{RMS} = \sqrt{\frac{\int_0^{\infty}(t-\tau_0)^2 h(t)\,dt}{\int_0^{\infty} h(t)\,dt}} \tag{5}$$

$$\tau_0 = \frac{\int_0^{\infty} t \times h(t)\,dt}{\int_0^{\infty} h(t)\,dt} \tag{6}$$

The frequency correlation function can be obtained from the CIR as

$$H(\Delta f) = \int_{-\infty}^{\infty} h(t) e^{-j2\pi\Delta f t}\,dt \tag{7}$$

For a particular correlation level c (typically chosen as 0.9, 0.7 or 0.5 [54]), coherence bandwidth (B_c) is defined as the minimum frequency separation for which the norm of the frequency correlation function across this level. It is calculated as

$$B_c = \min(\Delta f) \text{ such that } \left|H(\Delta f)\right| = c\ . \tag{8}$$

2.5 Comparison with Existing Models

To make a one-to-one comparison, we consider the same environment and parameters of [37], see Fig. 6 and related parameters in Table 3. Specifically, we consider a room size of 5 m × 5 m × 3 m where four LED luminaries are located on the ceiling and the detector is located at the corner of the floor as in Fig. 6. An LED

luminary consists of 100 LED chips and each chip radiates 0.45 W with a view angle of 120°. The FOV and area of the detector are 85° and 1cm^2, respectively. The reflection of materials in [37] is considered as purely diffuse and an ideal Lambertian source is used. In our case, we use Cree Xlamp® MC-E White LED (see Fig. 6.b) which has nearly-ideal Lambertian pattern.

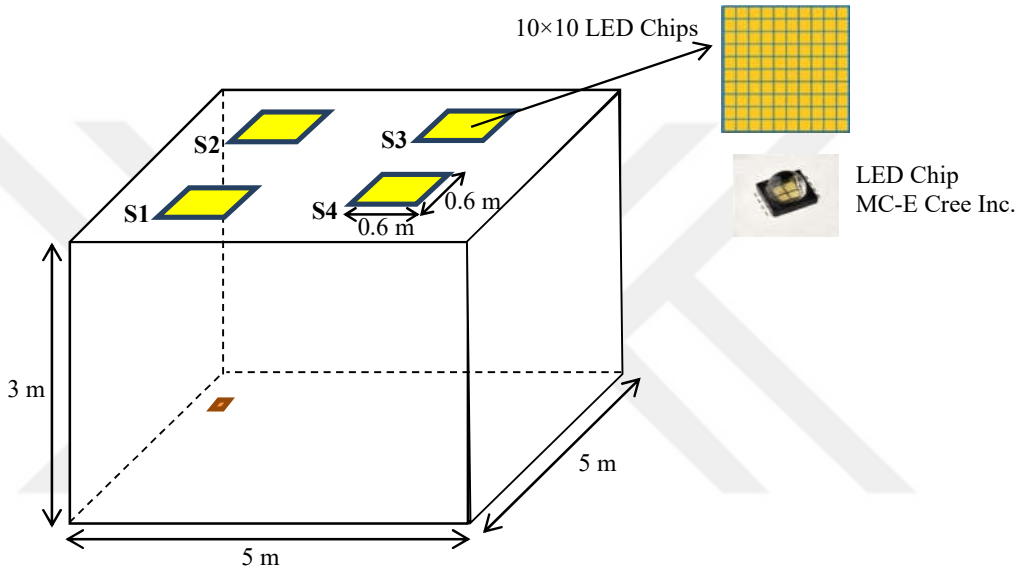

(a)

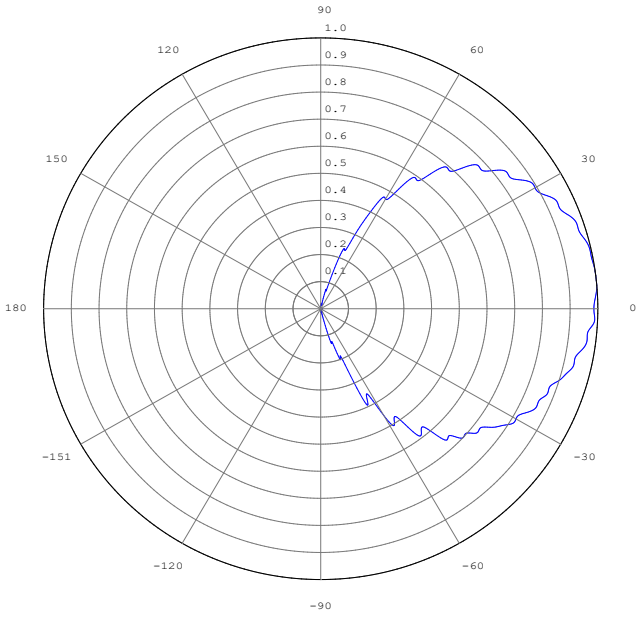

(b)

Figure 6: (a) 3D environment and (b) emission pattern of source

Table 3: Parameters of scenario in [37]

Size of room (m)	5 × 5 × 3
Time resolution (Δt)	0.2 (ns)
Number of lighting	4
Number of chip per each lighting	100
Power of each chip	0.45 (W)
Lighting positions (m)	(1.5,1.5,3) (1.5,3.5,3) (3.5,1.5,3) (3.5,3.5,3)
PD position (m)	(0.5,1,0)
View angle of lighting	120°
FOV of PD	85°
Area of PD	1 (cm^2)
Materials	Purely diffuse reflections

In the following, we present CIRs for $k=0$, 1, 2, 3. In Fig. 7, only LOS is considered. In Fig. 8.a, we present the CIR for first order reflections. It is observed from Fig. 8.b (which is basically obtained through superposition of CIRs presented in Fig. 7 and Fig. 8.a) that first order reflections contribute to increase the amplitude of zero order reflections. The delay spread also increases by first order reflections. Similarly, Fig. 9.b is a summation of CIRs presented in Fig. 8.b and Fig. 9.a. It is observed from Fig. 9.b that second order reflections slightly increases the amplitude of zero order reflections but effectively increases the delay spread of CIR.

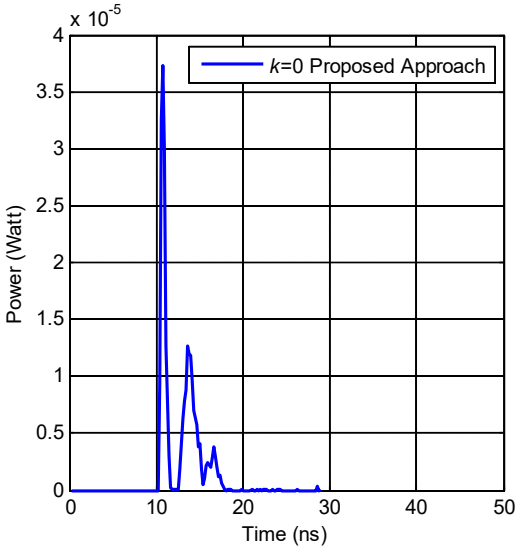

Figure 7: CIR for $k=0$ (Only LOS is considered)

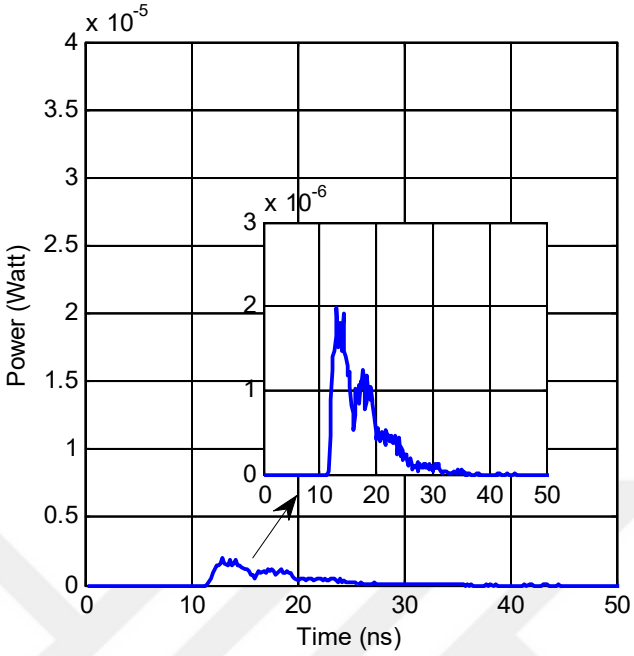

(a)

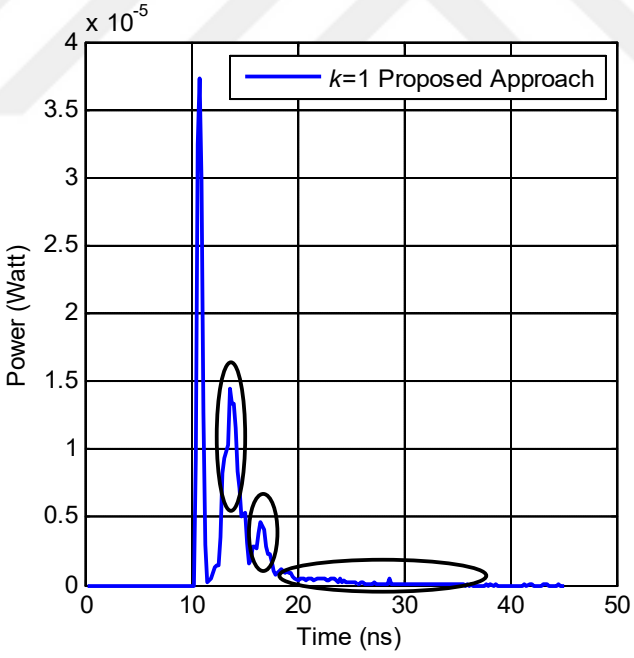

(b)

Figure 8: (a) CIR for first order reflections and (b) CIR for $k=1$ (i.e., LOS and first order reflections)

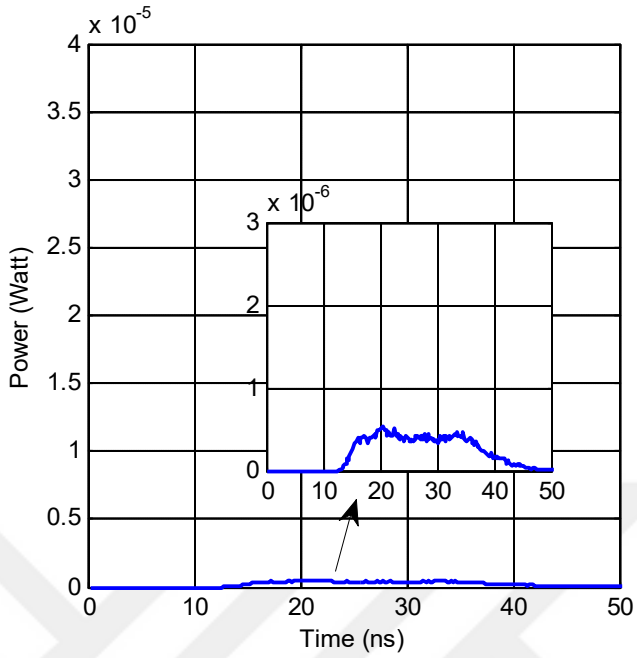

(a)

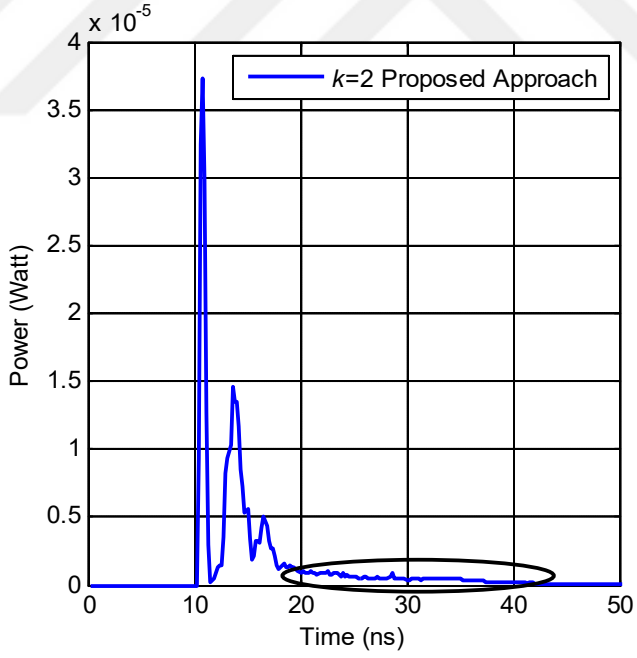

(b)

Figure 9: (a) CIR for second order reflections and (b) CIR for $k=2$ (i.e., LOS, first and second order reflections)

In Fig. 10, we present the CIR for $k=3$ reflections similar to [37]. It is observed that two CIRs are almost identical confirming the accuracy of our approach. Some small differences between the tails of two CIRs are observed. This is due to the fact that our light source is a commercial light source and not ideal Lambertian (see Fig. 6.b) unlike the theoretical one in [37]. It can be further noted that three peaks exist in CIR which are related to 4 LED lightings. The largest one corresponds to the nearest LED (S2) and the second one is related to two LEDs (S1 and S3) which are at the same distance from the photodetector (PD) and the last one is related to the farther LED (S4).

In Fig. 10, we assumed $k=3$ reflections to make a one-to-one comparison with [37], however note that our approach is able to handle more number of reflections. Fig. 11 and Table 4 present the values of channel parameters for k values up to 8. It is observed from Fig. 11 that there is no noticeable change for values larger than $k=4$ in an empty room under consideration.

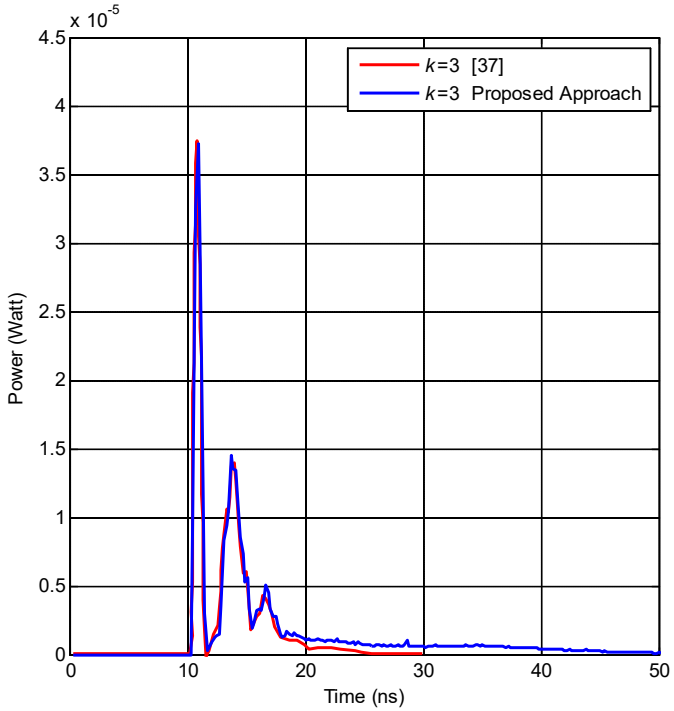

Figure 10: Comparison of the proposed approach with [37]

Table 4: Mean excess delay, RMS delay spread and channel DC gain for different k values in purely diffuse reflections

k	τ_0 (ns)	τ_{RMS} (ns)	H_0
0	12.58	2.10	4.82×10^{-5}
1	13.53	3.33	6.03×10^{-5}
2	15.59	6.60	7.06×10^{-5}
3	17.26	8.95	7.67×10^{-5}
4	17.42	9.25	7.71×10^{-5}
5	17.42	9.25	7.71×10^{-5}
6	17.42	9.26	7.71×10^{-5}
7	17.42	9.26	7.71×10^{-5}
8	17.42	9.26	7.71×10^{-5}

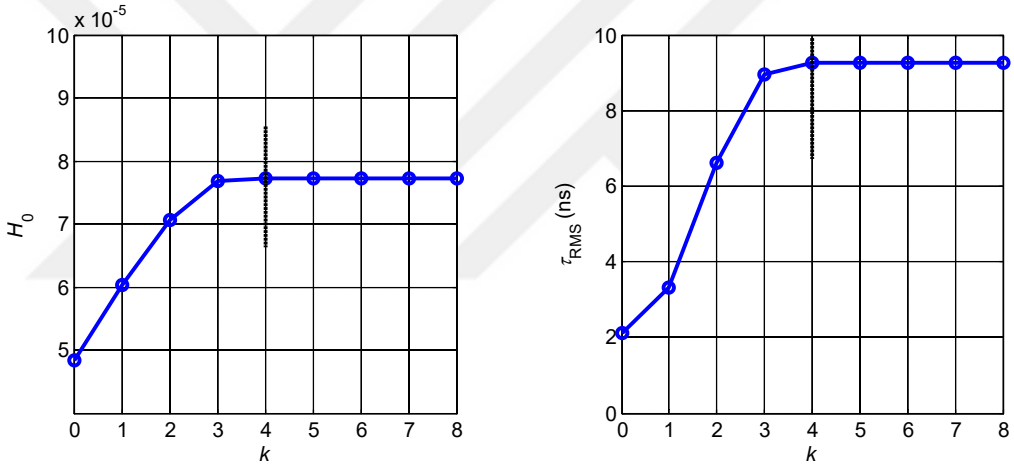

(a) (b)

Figure 11: (a) Channel DC gain and (b) RMS delay spread vs. number of reflection assuming diffuse reflections

Note that the recursive approach in [37] builds upon the assumption of purely diffuse reflections. In contrary, our approach can handle other type of reflections. In the following, we assume mixed reflections (see Fig. 12) and mostly specular reflections (see Fig. 13) where SF is set to 0.5 and 0.2 respectively. It is observed from Figs. 12 and 13 that the presence of specular components create fluctuations in CIR and results in deviations from the purely diffuse case considered in [37]. This is particularly evident in Fig. 13 where mostly specular case is considered. In diffuse case, when one ray reflects

from the surface, the power of ray decays by reflection coefficient and that power is divided among scattering rays. On the other hand, in specular case, the power of ray just decays by reflection coefficient and there is no division of power among scattering rays. By considering specular components for materials, the power of rays decays slowly which results in fluctuations of CIR.

To evaluate the impact of the number of the reflections on CIR, Fig. 14 and Tables 5 and 6 present the values of channel parameters for mixed and mostly specular reflection cases. It is observed from Fig. 14 that the RMS delay and channel DC gain saturate after 4 reflections for mixed case similar to purely diffuse case. However, in mostly specular case, this takes place after 7 reflections.

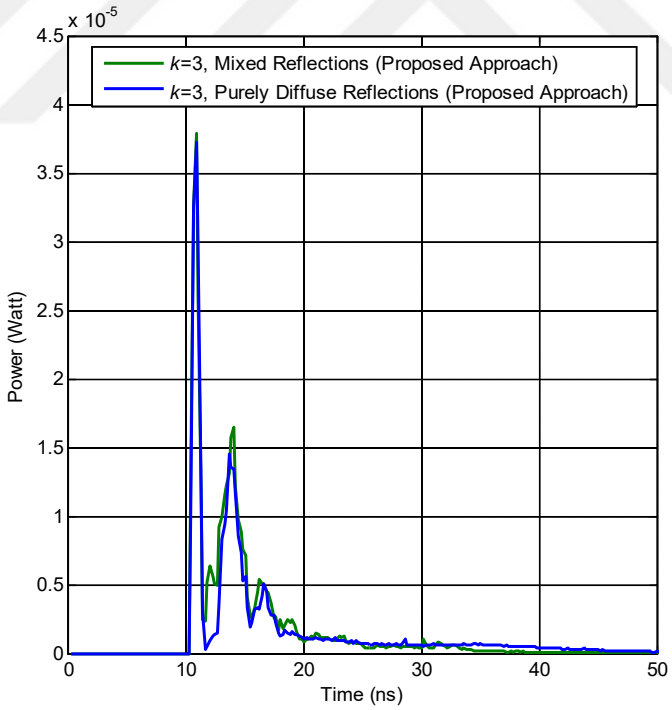

Figure 12: Comparison of CIRs under the assumptions of mixed reflections and purely diffuse reflections

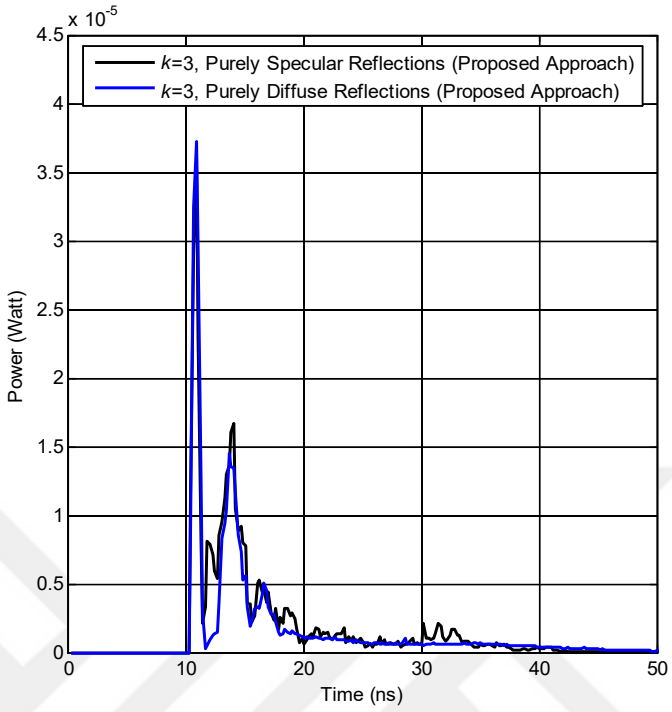

Figure 13: Comparison of CIRs under the assumptions of mostly specular reflections and purely diffuse reflections

Table 5: Mean excess delay, RMS delay spread and channel DC gain for different k values in the case of mixed reflections

k	τ_0 (ns)	τ_{RMS} (ns)	H_0
0	12.44	1.98	4.53×10^{-5}
1	13.88	3.52	7.38×10^{-5}
2	14.76	4.93	8.06×10^{-5}
3	15.05	5.49	8.19×10^{-5}
4	15.11	5.61	8.20×10^{-5}
5	15.11	5.61	8.21×10^{-5}
6	15.11	5.61	8.21×10^{-5}

Table 6: Mean excess delay, RMS delay spread and channel DC gain for different k values in the case of mostly specular reflections

k	τ_0 (ns)	τ_{RMS} (ns)	H_0
0	12.36	1.94	4.19×10^{-5}
1	13.85	3.45	7.40×10^{-5}
2	15.24	5.37	8.60×10^{-5}
3	16.46	7.12	9.19×10^{-5}
4	17.07	8.07	9.43×10^{-5}
5	17.44	8.78	9.53×10^{-5}
6	17.64	9.22	9.58×10^{-5}
7	17.74	9.49	9.60×10^{-5}
8	17.79	9.63	9.61×10^{-5}
9	17.81	9.72	9.61×10^{-5}
10	17.81	9.73	9.61×10^{-5}
11	17.82	9.74	9.61×10^{-5}
12	17.82	9.74	9.61×10^{-5}
13	17.82	9.74	9.61×10^{-5}
14	17.82	9.74	9.61×10^{-5}

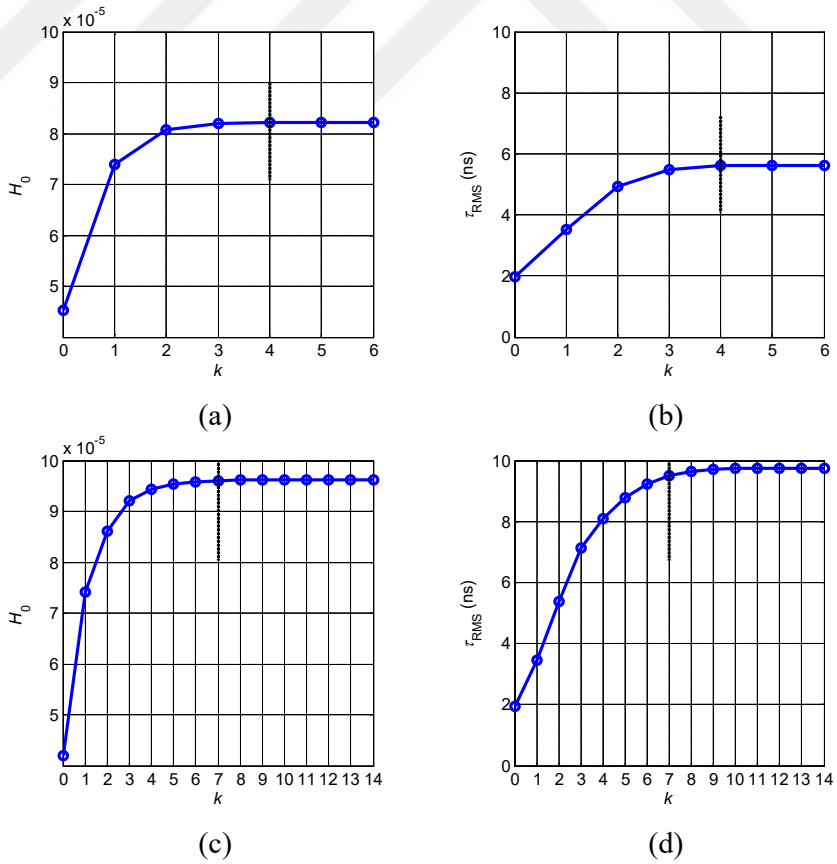

Figure 14: (a,c) Channel DC gain and (b,d) RMS delay spread vs. number of reflection assuming mixed reflections and mostly specular reflections

2.6 Indoor VLC Channel Characteristics

In the previous section, we have introduced our channel modeling approach and compared it with some existing works highlighting our advantages. In this section, based on our approach, we present CIRs for a number of indoor environments and discuss associated channel characteristics.

2.6.1 Effect of Distance between Transmitter and Receiver

In this section, we investigate the effect of varying distance between transmitter and receiver on channel parameters. We consider an empty room with a size of 10 m × 10 m × 3 m. The location of transmitter is fixed and located at the center of the ceiling. The location of receiver is varied on the diagonal which stretches from the corner to the middle of the floor. Effectively, the distance between the transmitter and receiver (d_{TX-RX}) varies between 3 m and 7.42 m. Similar to the previous section, we assume that the FOV and area of the detector are 85° and 1cm^2 respectively. The materials used for walls, ceiling and floor are respectively plaster, plaster and pine wood. To highlight the differences between VL and IR band, we repeat the same study for IR band under the same assumptions. For VL and IR band, we use the light sources given respectively in Figs. 5.a and 5.b.

Based on the aforementioned assumptions, Fig. 15 illustrates how channel DC gain, RMS delay spread, and coherence bandwidth change with the distance. The main observations are summarized in the following.

Channel DC gain (Fig. 15.a): It is observed that as d_{TX-RX} increases, the received power decreases in a negative exponential manner resulting in the decrease of channel DC gain. Through curve fitting, we express DC gain in terms of d_{TX-RX} as

$$H_0 = \begin{cases} 6.54\times10^{-5}\, e^{-0.99 d_{TX-RX}} + 7.52\times10^{-7}\, e^{-0.26 d_{TX-RX}} & \text{VL Band} \\ 5.71\times10^{-5}\, e^{-0.93 d_{TX-RX}} + 9.08\times10^{-7}\, e^{-0.12 d_{TX-RX}} & \text{IR Band} \end{cases} \quad (9)$$

Comparison of results obtained for IR and VL reveals that DC gains of VL channels are smaller than those in IR channels for same configurations. This is mainly due to the reason that reflectivity values in IR band are larger than those in VL band.

RMS delay spread (Fig. 15.b): It is observed that RMS delay spread first increases, then decreases with the increasing distance. It should be noted in our configuration the location of transmitter is fixed while the location of receiver is varied on the diagonal. This behavior change is a result of the detector location. Similar behavior is also reported in [55]. Through curve fitting, we express RMS delay spread in terms of d_{TX-RX} as

$$\tau_{RMS} = \begin{cases} 12.72\, e^{-\left(\frac{d_{TX-RX}-5.88}{4.29}\right)^2} & \text{VL Band} \\ 15.66\, e^{-\left(\frac{d_{TX-RX}-5.17}{5.34}\right)^2} & \text{IR Band} \end{cases} \quad (10)$$

Comparison of results obtained for IR and VL reveals that RMS delay spreads of VL channels are smaller than those in IR channels for same configurations. Similar to the observations in DC gains, this happens as a result of the fact that reflectivity values in IR band are larger than those in VL band.

Our results indicate that VL channel introduces an RMS delay spread of 8 ns-13 ns within the given environment. Targeting data speeds on the order of multiple gigabits per second will introduce inter-symbol-interference (ISI) spanning tens of symbols. This necessitates the use of proper ISI mitigation techniques for high speed VLC systems.

Coherence bandwidth (Fig. 15.c, 15.d): It is observed from Fig. 15.c that coherence bandwidth first decreases then slightly increases with the increasing distance. This is expected as coherence bandwidth is inversely proportional to RMS delay spread. Specifically, we obtain coherence bandwidth in terms of d_{TX-RX} as

$$B_c = \begin{cases} 1349\,e^{-1.60 d_{TX-RX}} + 3.93\,e^{0.03 d_{TX-RX}} & \text{VL Band} \\ 896.5\,e^{-1.91 d_{TX-RX}} + 1.92\,e^{0.09 d_{TX-RX}} & \text{IR Band} \end{cases} \tag{11}$$

It is also observed from Fig. 15.c that VL channels can potentially provide larger transmission bandwidth than IR channels.

In Fig. 15.d, we further illustrate the relation between coherence bandwidth and RMS delay spread. Through curve fitting, this relationship can be expressed as

$$B_c = \begin{cases} 1934\,\tau_{\text{RMS}}^{-2.37} & 7.5 < \tau_{\text{RMS}} < 14 \quad \text{VL Band} \\ 2303\,\tau_{\text{RMS}}^{-2.40} & 12 < \tau_{\text{RMS}} < 16.6 \quad \text{IR Band} \end{cases} \tag{12}$$

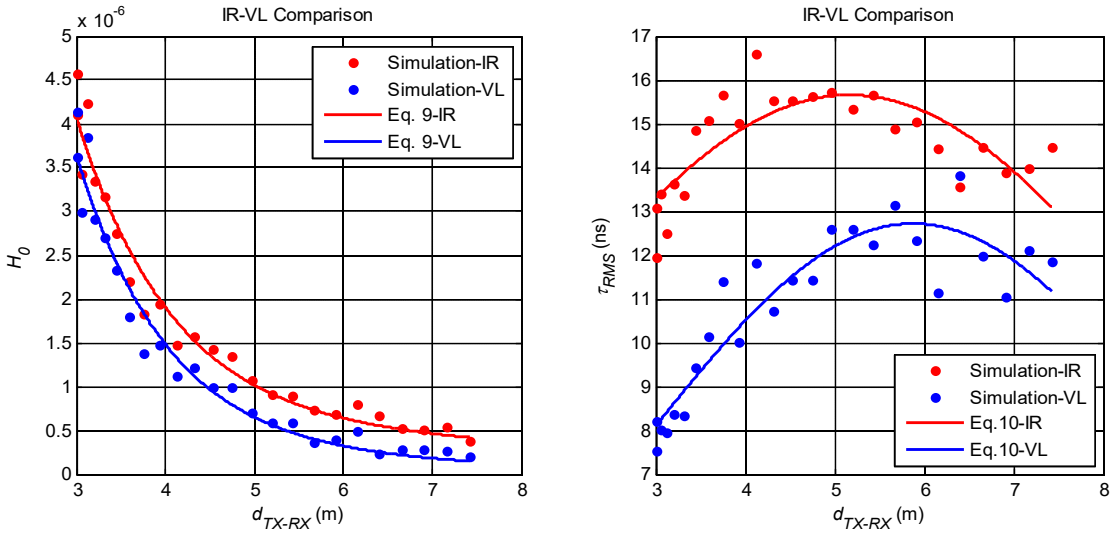

(a) (b)

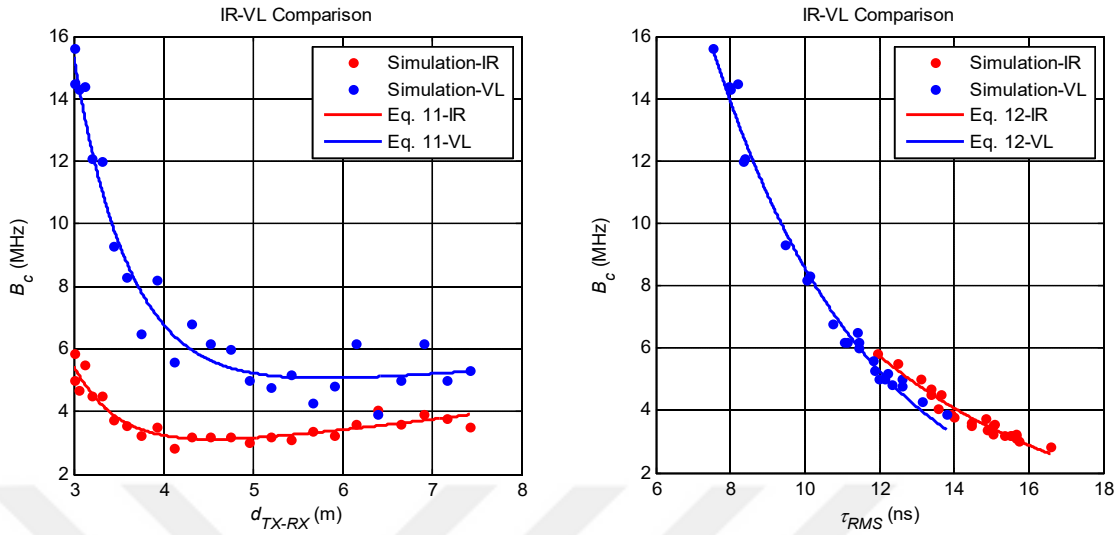

(c) (d)

Figure 15: (a) Channel DC gain vs. distance, (b) RMS delay vs. distance, (c) coherence bandwidth vs. distance and (d) coherence bandwidth vs. RMS delay spread

2.6.2 Effect of Multiple Transmitters, Position-Rotation of Transmitter-Receiver and the Presence of Objects

In the previous section, we have obtained CIRs and presented related channel parameters for an empty room with a single transmitter. In this section, we consider various environments with different transmitter specifications (i.e., multiple transmitters, array type), receiver specifications (i.e., location, rotation) and furniture.

In our study, we assume a room size of 5 m × 5 m × 3 m where the walls and ceiling are plaster while the floor is pinewood. The total power budget for LED chips is 1 W. Through this assumption, we associate channel DC gain with the averaged received power [24]. For easy identification, we label different configurations as VLx, x=1, 2, … , 8 illustrated in Figs. 16-18.

Effect of multi-transmitter deployment: In Fig. 16, we consider three configurations with different number of transmitters. The main features of these configurations are summarized below:

- **VL1:** Empty rectangular room with single transmitter located at the center of the ceiling and single receiver located at the center of the floor.
- **VL2:** Empty rectangular room with four transmitters located at the ceiling and single receiver located at the center of the floor.
- **VL3:** Empty rectangular room with sixteen transmitters located at the ceiling and single receiver located at the center of the floor.

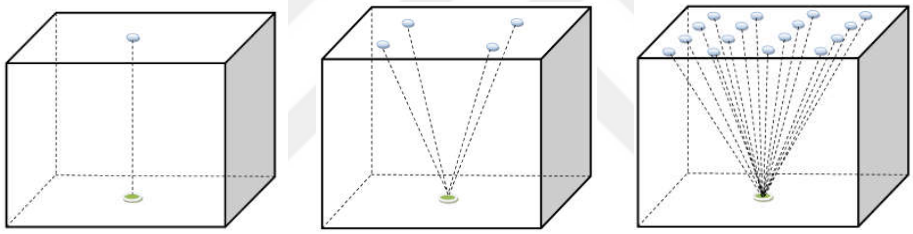

VL1 VL2 VL3

Figure 16: Configurations with multiple light sources

Table 7 summarizes the channel parameters for these three configurations under consideration. It is observed that by increasing the number of transmitters (see VL2 and VL3), channel DC gain decreases with respect to VL1 where the transmitter and receiver are perfectly aligned. Note that this observation is made under the assumption of a fixed overall transmit power budget. The received power therefore decreases with LEDs more dispersed on the ceiling. It is also observed from Table 7 that RMS delay spread increases in VL2 and VL3 in comparison to VL1 with single source since more scattering is received from multiple sources.

Table 7: Channel parameters for different number of transmitters

	τ_0 (ns)	τ_{RMS} (ns)	H_0
VL1	15.22	10.55	5.90×10^{-6}
VL2	19.92	10.60	3.02×10^{-6}
VL3	20.26	10.95	2.58×10^{-6}

Effect of position/rotation of receiver: In Fig. 17, we consider three configurations with different receiver rotations. The main features of these configurations are summarized below:

- **VL4:** Empty rectangular room with single transmitter located at the center of the ceiling and single receiver looking upwards located at the corner of the floor.
- **VL5:** Empty rectangular room with single transmitter located at the center of the ceiling and single receiver with 45 degrees rotation located at the corner of the floor.
- **VL6:** Empty rectangular room with single transmitter located at the center of the ceiling and single receiver with 90 degrees rotation located at the corner of the floor.

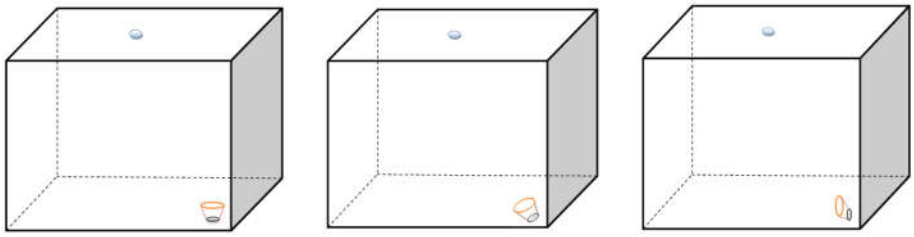

VL4 VL5 VL6

Figure 17: Configurations with various rotations of receiver

Based on the obtained CIRs and channel parameters (see Table 8), we observe that by rotation of detector towards to the source (see VL5), the channel DC gain

increases with respect to VL4 and VL6 where the receiver is pointed towards to the ceiling and walls respectively. It is also observed that by moving the detector to the corner side, the RMS delay spread increases with respect to VL1 where the detector is located at the center of the floor. It is a result of receiving more scattering power from corner sides.

Table 8: Channel parameters for different rotations of detector

	τ_0 (ns)	τ_{RMS} (ns)	H_0
VL4	26.18	11.59	1.09×10^{-6}
VL5	26.62	12.04	1.35×10^{-6}
VL6	26.34	12.97	1.17×10^{-6}

Effect of objects in the environment: In Fig. 18, we consider two different configurations to evaluate the effect of objects (e.g., furniture) in a room. The transmitter is located at the center of ceiling and the receiver is located at the center of the floor. In VL7 and VL8, we assume the same room size as VL1. The main features of these configurations are summarized below:

- VL7: Rectangular room with chair, desk and desk lamp.
- VL8: Rectangular room with chair, desk, desk lamp, laptop, couch, library, cage and coffee table.

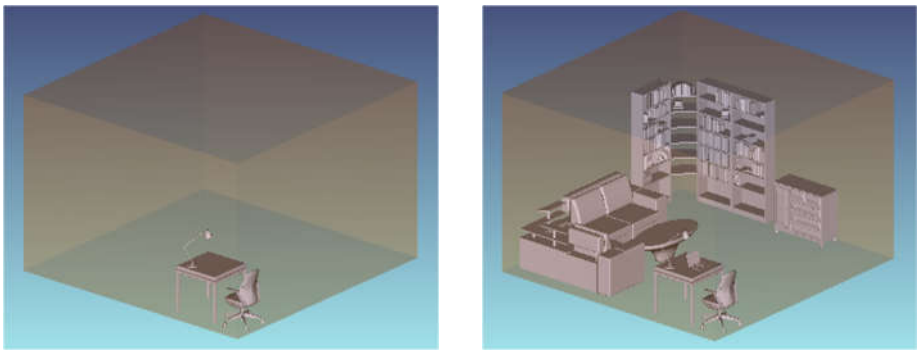

(a) (b)

Figure 18: Configurations with (a) few furniture and (b) lots of furniture

In VL7 and VL8, we assume that coating materials of desk, desk lamp, chair, cage, laptop, library, coffee table and couch are respectively pinewood, black gloss paint, black gloss paint, pinewood, black gloss paint, pinewood, pinewood and black gloss paint.

Based on the obtained CIRs and channel parameters (see Table 9), we observe that in the configuration with lots of furniture (VL8), the presence of furniture in the room has resulted in a decreased delay spread and channel DC gain. On the other hand, delay spread and channel DC gain in the room with few furniture (VL7) are similar to those ones in an empty room. It should be however noted that depending on relative positions of source, detector and furniture, different observations on CIR can made as noted in an earlier IR channel modeling study [26].

Table 9: Channel parameters for room with few furniture vs. lots of furniture

	τ_0 (ns)	τ_{RMS} (ns)	H_0
VL7	15.10	10.41	5.91×10^{-6}
VL8	13.08	7.80	5.58×10^{-6}

2.7 IEEE 802.15.7r1 Reference Channel Models

In December 2015, the IEEE established the Task Group 802.15.7r1 "Short Range Optical Wireless Communications" which is currently in the process of developing an international standard for VLC. As a part of our study, we developed channel models for four usage scenarios (i.e., workplace, office room with secondary light, living room, and manufacturing cell) considered in the IEEE 802.15.7r1 Technical Requirements Document [56]. These were endorsed by IEEE 802.15.7r1 as reference channel models [18].

In the following, we describe each of these scenarios, present associated CIRs and discuss the relevant channel parameters.

2.7.1 Scenario 1-Workplace

In the first reference scenario, two workplaces are considered where six office desks with working personnel are located. Both workplaces have identical sizes with dimensions of 14 m × 14 m × 3 m. The first one has an open office layout (Fig. 19.a) while the second one (Fig. 19.b) has cubicles. Human bodies are modeled as CAD objects with different coating materials for body parts. Specifically, absorptive coating is assumed for their heads and hands along with cotton clothes and black gloss shoes. 32 luminaries are uniformly located in a rectangular grid at the ceiling. The luminaries used in simulations are commercially available from Cree (LR24-38SKA35). They have a non-ideal Lambertian pattern, a half viewing angle of 40° and 73 lumens per watt efficacy. The average of illumination level is 533 lx satisfying typical illumination requirements for working places [57]. The specific materials for floor, ceiling, walls and objects within the environment can be found in Table 10.

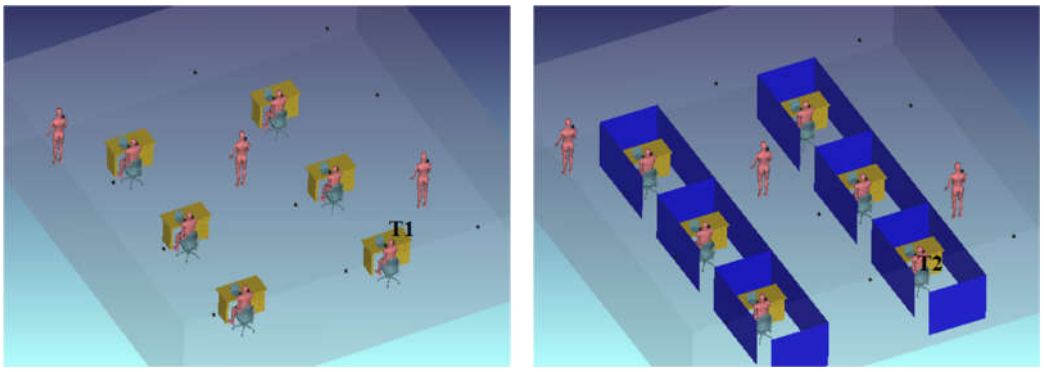

(a) (b)

Figure 19: (a) Workplace with open office concept and (b) workplace with cubicles

Table 10: Coating materials for objects within different scenarios

Scenario 1 Workplace	**Walls:** Plaster, **Ceiling:** Plaster, **Floor:** Pinewood, **Cubicles:** Plaster, **Desk:** Pinewood, **Chair:** Pinewood, **Laptop:** Black gloss paint
Scenario 2 Office room with secondary light	**Walls:** Plaster, **Ceiling:** Plaster, **Floor:** Pinewood, **Desk:** Pinewood, **Chair:** Black gloss paint, **Laptop:** Black gloss paint, **Desk light:** Black gloss paint, **Library:** Pinewood, **Window:** Glass, **Couch:** Cotton, **Coffee table:** Pinewood
Scenario 3 Living room	**Walls:** Plaster, **Ceiling:** Plaster, **Floor:** Pinewood, **Tables:** Wooden, **Chairs:** Wooden, **Couch:** Cotton, **Coffee table:** Glass
Scenario 4 Manufacturing cell	**Retaining Walls:** Concrete, **Manufacturing Gates:** Aluminum metal, **Cell boundaries:** Plexiglas (PMMA), **Ceiling:** Aluminum metal , **Floor:** Concrete, **Robot arm:** Galvanized steel metal

Different locations for the receivers are considered. For example, in one case, a standing person holds a cell phone in hand next to his/her ear and the detector is located on the phone (i.e., detector at a height of 1.7 m with 45° rotation). In another case, a personnel works at his/her desk and holds a cell phone in hand over his/her belly (i.e., detector at a height of 0.95 m with 45° rotation). In the third case, the personnel sits with a cell phone in hand to his/her ear (i.e., detector at a height of 1.1 m with 45° rotation). The FOV and the area of the detector are 85° and 1 cm^2 respectively.

CIRs for 24 different test points (see "black points" in Figs. 19.a and 19.b) can be found in [17]. As an example, two CIRs are presented in Figs. 20.a and 20.b. The associated test points are indicated by T1 in Fig. 19.a and T2 in Fig. 19.b. These correspond to the personnel who sits with a cell phone in hand to his/her ear. The average DC gain and RMS delay spread (averaged over 24 test points) are 8.13×10^{-4} and 15.27 ns respectively for workplace with open office. In workplace with cubicles, those values decrease to 7.51×10^{-4} and 12.68 ns, respectively. The decrease in channel DC gain is a result of the presence of cubicle walls. The rays hit the cubicle walls and decay more rapidly than those rays in open office. Similarly, since the rays cannot pass

through cubicle walls, delay spread decreases with respect to those in open office.

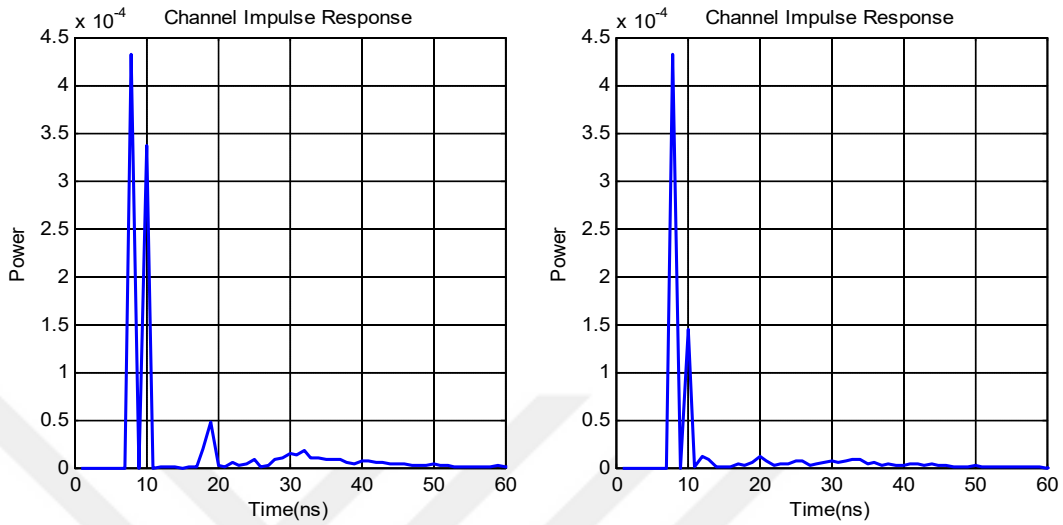

(a) (b)

Figure 20: Channel impulse responses for (a) T1 in workplace with open office concept and (b) T2 in workplace with cubicles

2.7.2 Scenario 2-Office Room with Secondary Light

In the second scenario, an office room with two light sources is considered. One of them is the main light source at the ceiling and the other one is a desk light. Such a scenario is particularly useful to evaluate the performance of relay-assisted (cooperative) VLC systems [58] where the ceiling light acts as the source and the desk light serves as the relay. The destination receiver is on the desk next to the laptop, see T3 in Fig. 21.b. This might for example take the form of a USB device connected to laptop. The relay receiver is on the top of desk light with 45° rotation towards the source on the ceiling. The room has a size of 5 m × 5 m × 3 m. The specifications of luminaries and detectors are selected the same as those in the first scenario. Other material specifications can be found in Table 10.

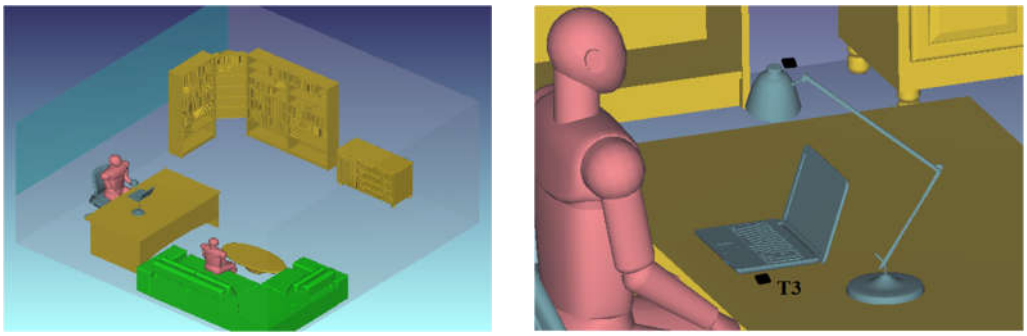

(a) (b)

Figure 21: (a) Office room with secondary light and (b) enlarged version of (c) showing secondary light, i.e., desk light

The CIRs associated with links from source to destination (S→D) and relay to destination (R→D) are presented in Figs. 22.a and 22.b. As expected, R→D channel is stronger than S→D channel since the relay transmitter is closer to the destination and therefore experiences smaller path loss. It is also observed that S→D channel has more scattering components inducing a larger delay spread. Since the distance between source and destination is larger than the distance between relay and destination, the rays coming out from the source hit more surfaces (i.e., wall, floor and objects inside the room) and result in more scattering.

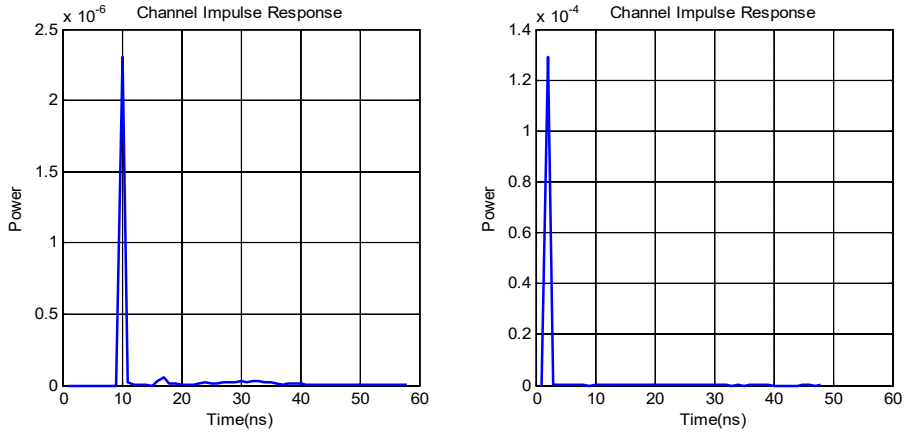

(a) (b)

Figure 22: (a) source to destination in office with secondary light and (b) relay to destination in office with secondary light

2.7.3 Scenario 3-Living Room

In the third scenario, a living room of size 6 m × 6 m × 3 m is considered (see Fig. 23). Four persons are present in the room; two sitting on the couch with other two standing. Nine luminaries (Cree CR6-800L) are uniformly located in a rectangular grid at the ceiling. They have a half viewing angle of 40° and 67 lumens per watt efficacy. The average of illumination level is calculated as 153 lx [57].

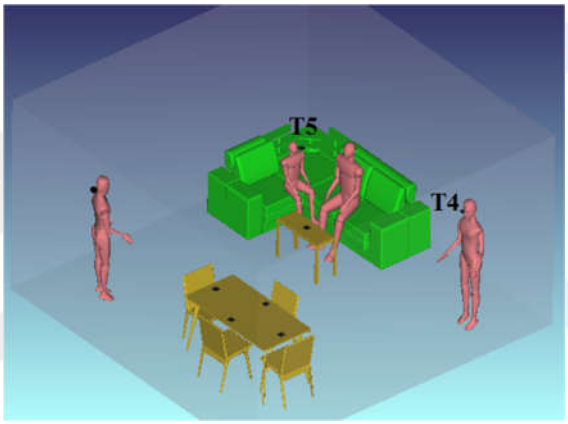

Figure 23: Living room

Similar to Scenario 1, various locations are considered for the receivers. In one case, the person is in a standing position and holds a cell phone in hand next to his/her ear. The detector is located on the phone (i.e., detector at a height of 1.7 m with 45° rotation). In another case, a person sits on the couch. He/she holds a cell phone in hand next to his/her ear and the detector is located on the phone at a height of 1.1 m with 45° rotation. The detectors on the dinner table are at a height of 0.9 m and that one on the coffee table is at a height of 0.6 m with 45° rotation toward the human being who sits on the couch.

CIRs obtained for eight test points (see Fig. 23) can be found in [17]. As an example, two CIRs are presented in Figs. 24.a and 24.b. The associated test points are

indicated by T4 and T5 in Fig. 23. The average DC gain and RMS delay spread (averaged over 8 test points) are calculated as 2.61×10^{-4} and 9.24 ns, respectively. It is observed that these are smaller than those observed in the workplace since the room dimensions are now smaller.

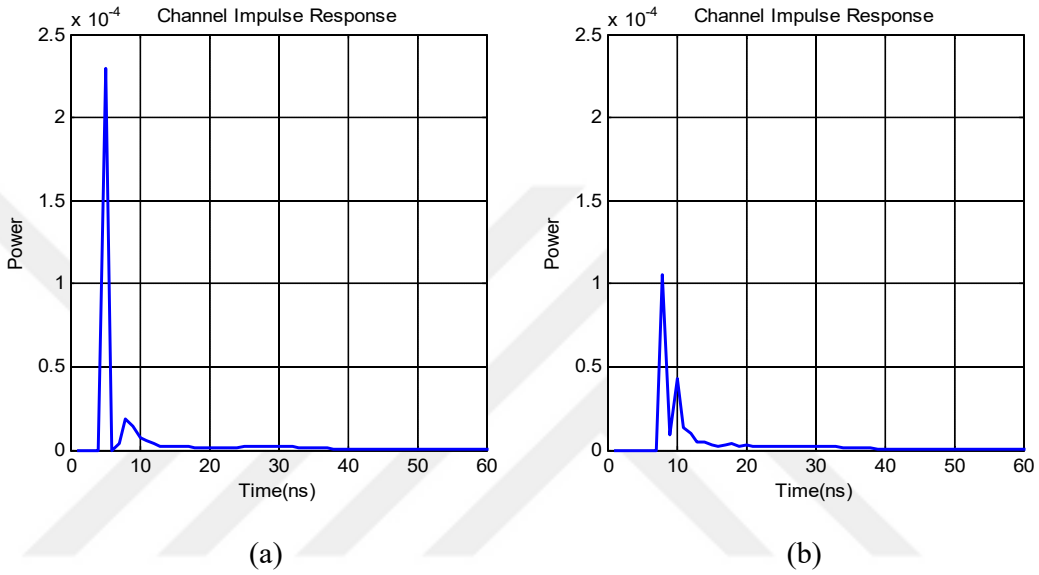

Figure 24: (a) T4 in living room and (b) T5 in living room

2.7.4 Scenario 4-Manufacturing Cell

In the fourth scenario, a manufacturing cell of size 8.03 m × 9.45 m × 6.8 m is considered. Six LED transmitters are located at the head of the robotic arm which has a form of cube. Each face of the cube is equipped with one transmitter ensuring 360° coverage. The LEDs are commercially available from Cree (MC-E) with non-ideal Lambertian pattern and a half viewing angle of 60°. The FOV and the area of the detector are 35° and 1 cm^2 respectively.

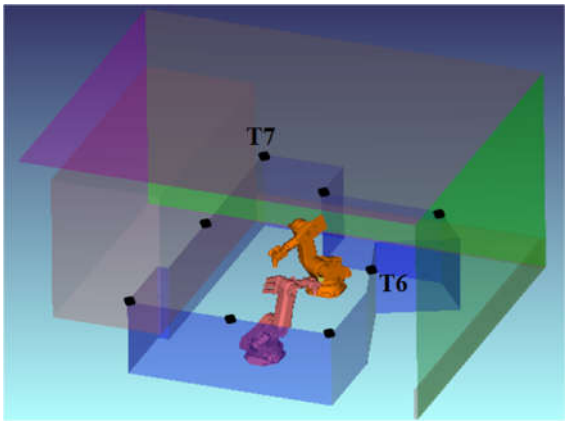

Figure 25: Manufacturing cell

Eight test points are considered on the top of the cell boundaries (see Fig. 25). As an example, two CIRs are presented in Figs. 26.a and 26.b. The associated test points are indicated by T6 and T7 in Fig. 25). These are rotated detectors toward the robot arms which are respectively placed in the middle and at the corner side of the cell boundary. It is observed that the amplitude of T6 is much larger than that of T7 because this detector is closer to the set of transmitters. Since T7 is located at the corner of the cell boundary, it receives more scattering from boundaries. On the other hand, the RMS delay spread of T7 is much larger than that of T6.

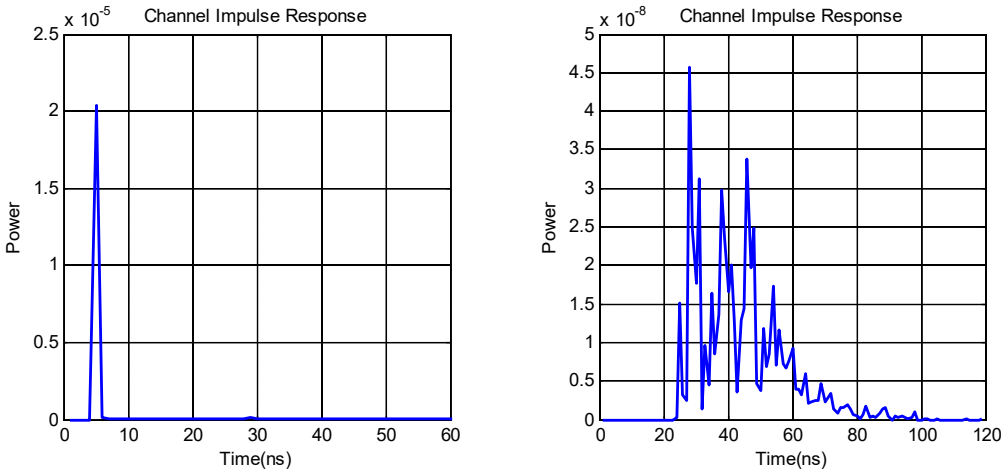

(a) (b)

Figure 26: (a) T6 in manufacturing cell and (b) T7 in manufacturing cell

2.8 Effect of User Mobility

Our discussion so far is limited to fixed user scenarios. There are only sporadic works which consider mobility in VLC channel modeling [59-62]. In [62], the shadowing effect caused by the human body was considered for VLC channel characteristics. This however builds on some simplifying assumptions such as ideal Lambertian source and purely diffuse reflections. An empty room was also considered ignoring the presence of furniture or any other objects. Another simplifying assumption in [59, 60, 62] was fixed reflectance values for surface materials (i.e., wall, floor, etc). While this can be justified for infrared wavelengths, wavelength dependency should be considered for realistic channel modeling in VLC. Most works also consider empty rooms ignoring the presence of human beings, furniture or any other objects. A comparison of existing mobile VLC channel models can be found in Table 11.

Table 11: Comparison of existing mobile VLC channel models

	Method	**Modeling of Reflectance**	**Number of Reflections**	**Type of Reflections**	**Source Type**	**Environmet and Other Assumptions**
[59]	Recursive	Fixed reflectance	First order	Purely Lambertian	Ideal Lambertian source	- Empty room - Multiple luminaries
[60]	Recursive	Fixed reflectance	First order	Purely Lambertian	Ideal Lambertian source	- Empty room - Multiple luminaries
[61]	Monte Carlo ray tracing	Wavelength dependent	High order (>4)	Purely Lambertian	Ideal Lambertian source	- Empty room - Mock-up human body - Single luminary
[62]	Recursive	Fixed reflectance	First order	Purely Lambertian	Ideal Lambertian source	- Room with furniture - Multiple luminaries

In this section, we adopt our realistic channel modeling approach which overcomes the limitations in earlier works and present a mobile VLC channel model

[19]. We consider a living room with a size of 6 m × 6 m × 3 m as illustrated in Fig. 27.a with plaster ceiling/walls and pinewood floor. We assume that coating materials of table, chairs, couch and coffee table are respectively pinewood, pinewood, cotton and glass. Human bodies are modeled as CAD objects with different coating materials for different parts of the body. Specifically, their heads and hands are modeled as absorbing objects while cotton clothes and black gloss shoes are assumed. We assume nine luminaries on the ceiling with equidistance spacing. These are commercially available LEDs (Cree® CR6-800L) with 40° half viewing angle. The optical power for each luminary is 11 Watts. This yields an average illumination level of 153 lux which satisfies typical illumination levels for home environment [57].

Here, we assume that the user walks on three different trajectories within the room (see Fig. 27.b for blue, green and red lines). We assume that he/she holds a cell phone in hand next to his/her ear and the detector is located on the phone. The orientation of human body (where he/she is facing) changes according to the direction of the way while the rotation and location of cell phone (i.e., 45° rotation and at a height of 1.8 m) in his/her hand are fixed with respect to his/her ear. The FOV and the area of the detector are 85° and 1 cm^2 respectively.

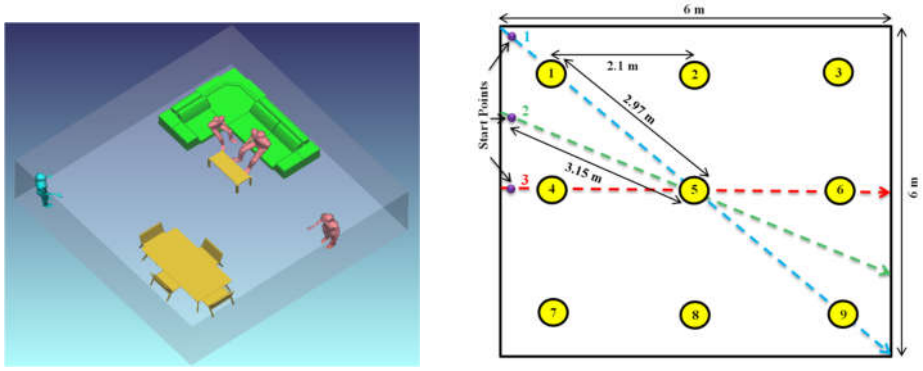

(a) (b)

Figure 27: (a) Living room under consideration and (b) movement trajectories with yellow circles denoting luminaries

Based on the approach summarized above and given scenario, we obtain CIRs for all points with 40 cm interdistance along each trajectory. Let $h_i(t)$ denote the individual optical CIR between the ith luminary and the receiver. $h(t)=\sum_{i=1}^{N_t} h_i(t)$ represents the combined optical CIR where N_t is the number of luminaries. The path loss is expressed as (4) and illustrated in Fig. 28 for three trajectories under consideration.

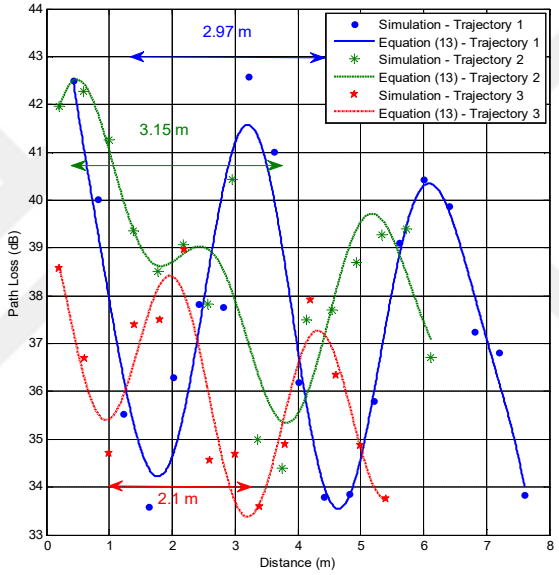

Figure 28: Path loss vs. distance along trajectories 1, 2 and 3

We apply curve fitting techniques on our observations based on the minimization of root mean square error (RMSE) to obtain some expressions for the path loss. We adopt cross validation, particularly "leave-one-out cross-validation (LOOCV)" method [63] to avoid over-fitting. Through curve fitting, we obtain

$$PL=\sum_{j=1}^{n} k_j \sin\left(l_j d+m_j\right) \tag{13}$$

The related coefficients k_j, l_j and m_j are presented in Table 12.

Table 12: Coefficients in (13) for room with size of 6 m × 6 m × 3 m

Trajectory 1 (Blue Line)					
k_1	108.40	l_1	0.13	m_1	2.25
k_2	38.32	l_2	0.56	m_2	3.94
k_3	10.46	l_3	1.09	m_3	5.03
k_4	2.49	l_4	2.43	m_4	-0.08
Trajectory 2 (Green Line)					
k_1	108.9	l_1	0.40	m_1	0.28
k_2	72.22	l_2	0.52	m_2	3.00
k_3	1.35	l_3	2.67	m_3	0.64
Trajectory 3 (Red Line)					
k_1	238.00	l_1	0.24	m_1	0.59
k_2	202.80	l_2	0.27	m_2	3.62
k_3	2.05	l_3	2.76	m_3	2.25

In (13), d is the distance of user from the start point and n is given by

$$n = \begin{cases} \sqrt{N_t} + 1 & \text{for trajectory 1} \\ \sqrt{N_t} & \text{for trajectory 2 and 3} \end{cases} \tag{14}$$

It is interesting to note that the value of n is directly related to the number of LEDs that contribute most to received power. For example, in trajectory 1 (indicated by blue line), n is equal to 4. It can be confirmed that 4 LEDs out of the total 9 contribute 95% of the total received power. Similarly, in other trajectories, a significant portion of the received power is contributed by n LEDs.

It is observed from Fig. 28 that as user moves along trajectory 1, the received power decreases (i.e., path loss increases) as he moves away from the luminary and increases when he approaches to the next one. It can be verified that the distance of two peaks in path loss is 2.97 m which is equal to the spacing between two adjacent luminaries on that trajectory. This distance reduces to 2.1 m for trajectory 3 (indicated by red line) where three luminaries are located. Over trajectory 2 (indicated by green line), it is observed that the path loss takes its minimum value around 3.64 m where the only luminary over this trajectory (i.e., labeled as 5th LED) is located. The distance

between the points where minimum and maximum path loss is 3.15 m; this corresponds to the distance of centered luminary (i.e., labeled as 5th LED) from the start point.

Through RMSE based curve fitting, the RMS delay spread of channel can be expressed as

$$\tau_{RMS} = \sum_{j=1}^{n} u_j \sin\left(v_j d + w_j\right) \tag{15}$$

where n is given by (14) and the related coefficients u_j, v_j and w_j are presented in Table 13. The RMS delay spread is illustrated in Fig. 29 for three trajectories under consideration. It is observed that RMS delay spread increases when the user moves away from the luminary while it decreases when the user moves toward the luminary. This is due to the fact that the differences on the signal arrival time from the LEDs to the receiver are small when the user is close to the luminary.

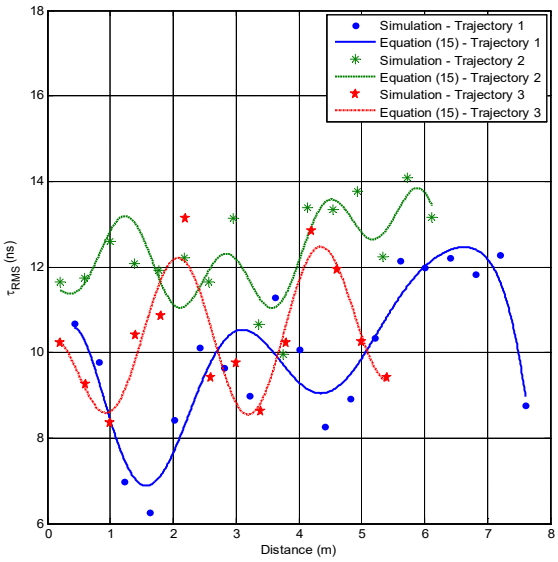

Figure 29: RMS delay spread vs. distance along trajectories 1, 2 and 3

Table 13: Coefficients in (15) for room with size of 6 m × 6 m × 3 m

Trajectory 1 (Blue Line)					
u_1	33.75	v_1	0.70	w_1	-1.21
u_2	38.35	v_2	1.04	w_2	0.62
u_3	37.22	v_3	1.55	w_3	1.66
u_4	23.46	v_4	1.70	w_4	4.12
Trajectory 2 (Green Line)					
u_1	31.71	v_1	0.46	w_1	0.13
u_2	20.16	v_2	0.63	w_2	2.77
u_3	0.79	v_3	3.98	w_3	-3.49
Trajectory 3 (Red Line)					
u_1	19.44	v_1	0.41	w_1	0.18
u_2	9.13	v_2	0.65	w_2	2.54
u_3	1.75	v_3	2.84	w_3	1.90

To confirm the validity of (13) and (15) for different cases, we further consider two empty rooms with sizes of 9 m × 9 m × 3 m and 12 m × 12 m × 3 m. To achieve the desired illumination levels (i.e., 153 lux), we assume the deployment of 25 and 49 luminaries in a square structure with equidistant spacing. Fig. 30 illustrates the path loss and RMS delay spread over the trajectory 3 for both rooms. It can be readily verified that they follow the same form as (13) and (15).

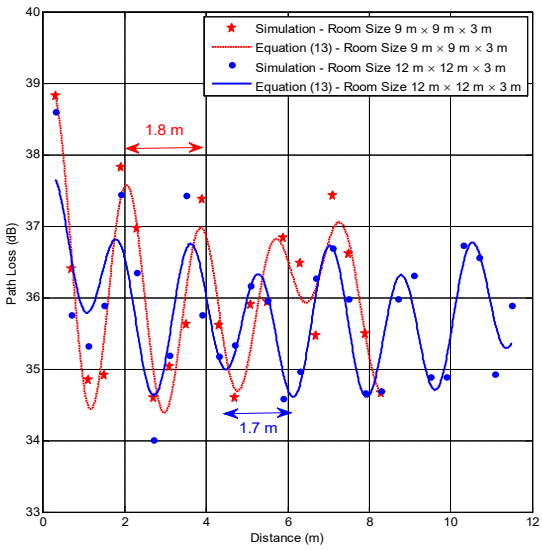

(a)

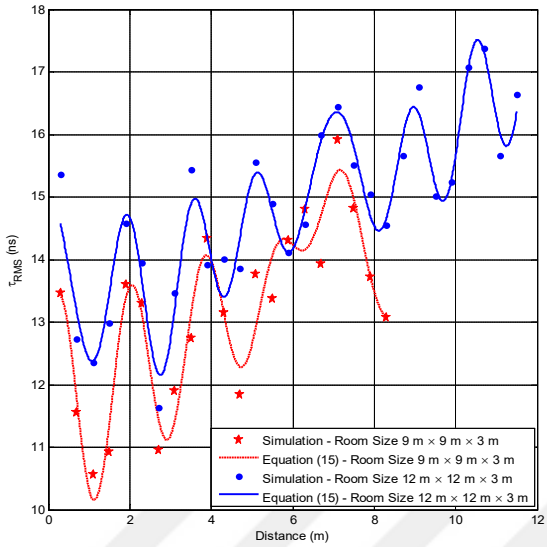

(b)

Figure 30: (a) Path loss vs. distance and (b) RMS delay spread vs. distance for rooms with sizes of 9 m × 9 m × 3 m and 12 m × 12 m × 3m

2.9 Effect of Receiver Orientation

In this section, we investigate the effect of photodetector location/orientation. We consider a mobile receiver terminal in the form of a cell phone. Seven possible locations are considered for the photodetector. Five of these are on the top edge and two of them are on the top round corners of the device. For each possible location of photodetector, we obtain CIRs and corresponding path loss. To further demonstrate the effects of user location, we present the spatial distribution of path loss within the room.

We consider a room with a size of 6 m × 6 m × 3 m as illustrated in Fig. 31 with plaster ceiling/walls and pinewood floor. We assume nine luminaries on the ceiling with equidistance spacing. These are commercially available LEDs (Cree® CR6-800L) with 40º half viewing angle. The optical power for each luminary is 11 Watts. This yields an average illumination level of 153 lux which satisfies typical illumination levels for home environment [57].

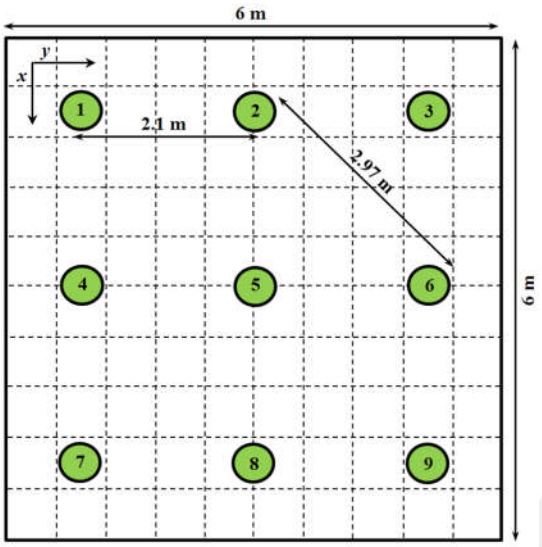

Figure 31: Room under consideration with green circles denoting luminaires

We consider a user with a height of 1.8 m and model the human body as a CAD object (see Fig. 32.a) with absorbing property. The cell phone has a size of 5.5 cm × 10.5 cm × 0.5 cm and is equipped with a single photodetector. The user holds the phone in his hand next to his ear with 45° rotation upward the ceiling and at a height of 1.8 m. We consider seven potential locations for the photodetectors denoted as D_n, $n = 1,...,7$ (see Fig. 32.b). $D_1,\ldots,D_5$ are placed on the top edge of the cell phone oriented toward the ceiling. D_6 and D_7 are placed on the top two round corners of the cell phone oriented toward the ceiling and floor, respectively. The FOV and the area of each detector are 85° and 1 cm^2, respectively.

Non-sequential ray tracing features of Zemax® are used to calculate the detected power and path lengths from source to detector for each ray. These are then imported Matlab to obtain the CIR. To further investigate the effects of user locations, we consider 100 cells with equidistant spacing of 0.6 m in *x* and *y* directions. The user is assumed to be standing in the middle of the cell. Let $h_i(t)$ denote the individual optical

CIR between the ith luminary and a given location of the photodetector. The combined optical CIR is given by $h(t) = \sum_{i=1}^{9} h_i(t)$. The path loss can be then calculated as (4).

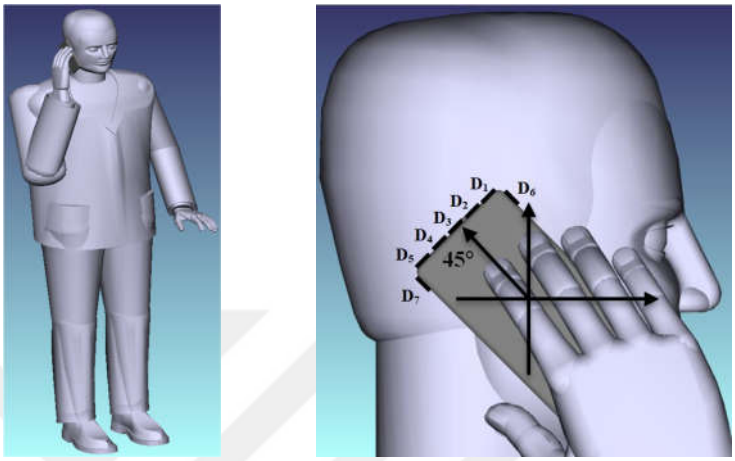

(a) (b)

Figure 32: (a) Human model and (b) location/orientation of PDs on the cell phone

In Fig. 33, we illustrate the spatial distribution of path loss as seen by the individual photodetectors D_n, $n = 1,...,7$. It is observed that as user moves within the room, the spatial distributions of path loss seen by the photodetectors $D_1,\ldots,D_6$ follow the sinusoidal pattern in *x* and *y* directions. In other words, the maximum signal strength (i.e., minimum value of path loss) occurs when human moves under the luminaire and vice versa. On the other hand, the spatial distribution of path loss seen by the photodetector D_7 is almost flat (i.e., the same path loss for all cells). This is due to this fact that this detector is oriented toward the floor and cannot see the received rays from luminaires. It is also observed from Fig. 33 that the average path losses over different cells for D_1, D_2, D_3, D_4, D_5, D_6 and D_7 are 58.96 dB, 58.78 dB, 58.50 dB, 58.16 dB, 57.97 dB, 58.69 dB and 61.19 dB, respectively.

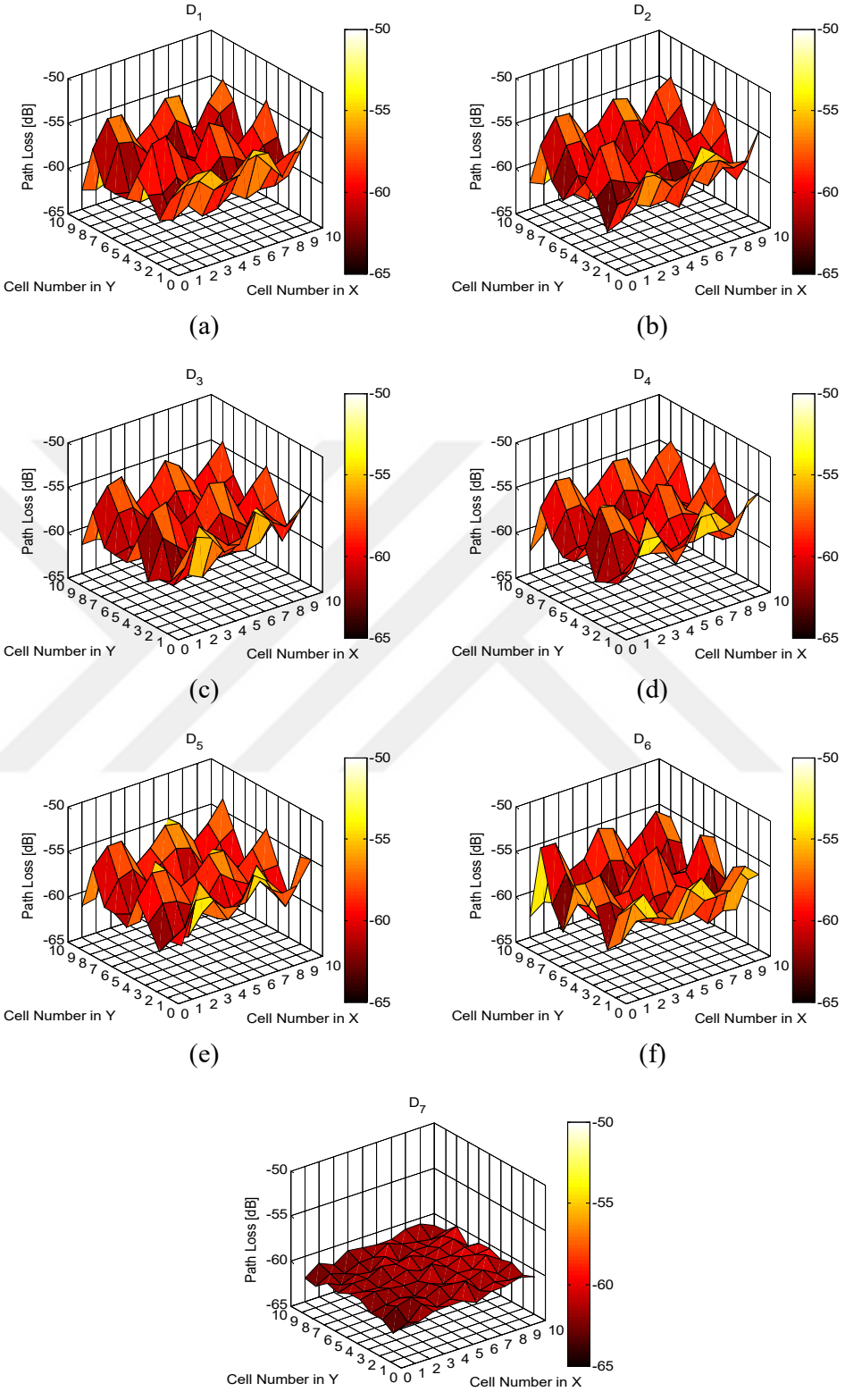

Figure 33: Spatial distributions of path loss as seen by the individual photodetectors D_n, $n = 1,...,7$

In Fig. 34, we present the cumulative distribution function (CDF) of path loss as seen by the individual photodetectors D_n, $n = 1,...,7$. This gives the probability that path loss will take less than or equal to a specific value. It is observed from Fig. 34 that the best locations of PD on the cell phone (i.e., minimum path loss) are D_4 and D_5.

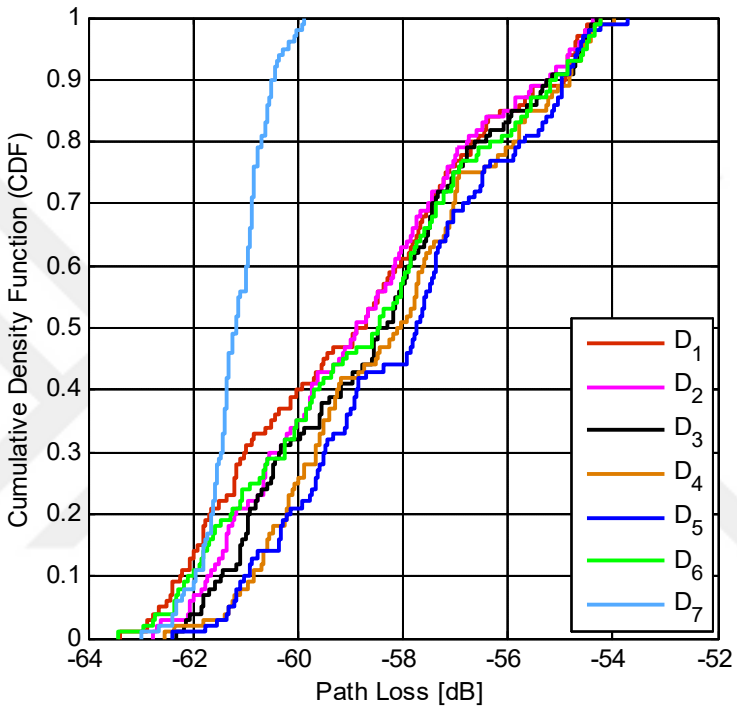

Figure 34: CDF of path loss as seen by the individual photodetectors $D_n, n = 1,...,7$

CHAPTER III

CHANNEL MODELING AND CHARACTERIZATION FOR VEHICULAR VISIBLE LIGHT COMMUNICATIONS

3.1 Introduction

While VLC has been studied intensively in the context of indoor communications [64, 65], its application to vehicular networking is relatively new [66, 67]. Vehicular networking is one of the main enablers of ITSs for V2V, V2I and I2V communications. In such an emerging topic, channel modeling is particularly important to understand the fundamental performance limits imposed by the outdoor medium. There has been a growing interest on vehicular VLC channel modeling [68-89]. Earlier works [68-71] build upon the LOS channel model originally proposed for the indoor LED light sources with Lambertian pattern. This can be adopted for some I2V links such as between traffic light and vehicle. However, such a model is not applicable to automotive low-beam and high-beam headlamps with asymmetrical intensity distributions as well as street lights. Furthermore, the reflectance of road surface and weather conditions should be further taken into account for outdoor VLC deployments.

In this chapter, we first present a literature overview of the existing vehicular VLC channel models. After we highlight the shortcomings of existing works, we present our vehicular VLC channel modeling approach.

3.2 Existing Vehicular VLC Channel Models

In [68], a traffic information system using LED traffic light was proposed. The LOS path was considered between traffic light and vehicles placed on two lanes of the road. It was demonstrated that the LOS path is greatly affected by the position of a receiver, the angle, the FOV and receiver's vertical inclination. In [69], the LOS channel model was adopted to carry out vehicular communications using a LED road illumination. The LED road illumination was designed to fulfill the standard specification of road illuminations in Japan. In [70], various parameters of a traffic light information system (i.e., the height of traffic light and orientation of the emitter) were optimized in a traffic light-to-vehicle set-up model by utilizing LOS configuration. In [71], a low data rate traffic broadcasting system was implemented in vehicular communication by considering a LOS channel model for LED array traffic light with Lambertian pattern.

In [74], a vehicular VLC channel model for V2V setting was proposed where an off-the-shelf scooter taillight is used at the transmitting end. Since the Lambertian pattern adopted in the LOS channel model is not able to capture the automotive lights pattern accurately, a piecewise Lambertian channel model was proposed to reflect the asymmetrical intensity distribution of scooter taillight. The analytical results obtained by this model were confirmed with empirical measurements.

In [72, 73], MCRT was used to obtain channel delay profiles for V2V, I2V and V2I configurations. The practical headlamp and street lamp were modeled where the effects of surroundings, i.e., buildings, road surface etc are considered via CAD file models. The results demonstrated that the common property of the delay profile was composed of dominant multiple LOS links and a less number of NLOS delay taps.

However, the delay profile from the V2I link and metropolitan scenario had more dispersive channel characteristics due to the reflection and the diffusion of the visible light.

The road surface might impact the vehicular VLC system performance. The reflectance of road surface depends on its nature and physical state, and it also changes with weather conditions. In [75, 76], a geometric V2V VLC channel model was proposed based on the measured headlamp beam patterns and a road surface reflection model. The link bit-error-rate (BER) performance was investigated for the clean and dirty headlamps in a wet and dry road surface.

In [77], the first study to investigate a problem of link asymmetry in V2V VLC was performed. The optical radiation pattern measurements were made with off-the-shelf LED headlamps and taillights and a number of vehicle mobility traces with 2-dimensional locations were collected. Combining these data, an analytical study was performed to obtain an experimental distribution for received power difference of the links in opposite directions.

In [78], an experimental study was performed to determine the spatial and angular limits of an off-the-shelf automotive LED fog light. It was shown that the received optical power of single channel VLC depends on the angle and distance, and demonstrated that Lambertian model does not represent the automotive LED fog light radiation pattern accurately. In [79], the configuration selection of the optical transmitters and MIMO modes with the corresponding modulation orders for vehicular VLC with the usage of measured vehicular visible light channel model was studied. The automotive brake lights compliant with the regulation was employed, and night time measurements were conducted at practical receiver locations to evaluate the sun light

interference free characteristics of optical signals from brake lights. In [80], IEEE 802.15.7 standard-compliant physical layer (PHY) implementation and experimental evaluation was proposed, using commercial off-the-shelf automotive LED fog light in a V2V VLC scenario.

In [81], an experimental set-up for vehicular VLC based on LED headlamp was demonstrated. The proposed system showed a potential for V2V VLC with 10 kbps data rate in about 20 m distance at day time scenario. In [82], the time variation of the V2V VLC channel was empirically characterized, by investigating how vehicle mobility and different vehicle behaviours correlate with the time variation. A measurement platform utilizing a commercial LED headlamp in a real-world road environment and in a car-following setting was developed. In [83], a prototype VLC based V2V system for communicating hard brake warning to the following vehicle was designed. The measurements were conducted in a real world road environment where daylight and twilight are considered to observe the reliability of VLC link. In [84], the bias/driving voltage of a vehicular LED was optimized and the transmission performance of 25 Mb/s on-off-keying (OOK) signal over a 60 m V2V VLC link was experimentally investigated with ambient light interference in the outdoor condition.

In [85], a number of real world experiments were performed where the low beam is used for the headlight, and positioning and the brake lights are used for the taillight. The measurements were performed at night to minimize the influence of environmental factors. An analytical path loss model was derived as a function of distance and angle between transmitter and receiver and further the impact of turns on a curved road on the channel was investigated. It was observed that the specific radiation pattern of car headlights may cause problems in maintaining a stable VLC link between two cars, particularly when turning left (that is to say right in countries with left lane traffic).

Another critical issue for vehicular VLC channels is the weather conditions which have received little attention so far in the literature. While there are some other works that quantify the effect of weather conditions on infrared LED transmission [90], these cannot be applied in a straightforward manner to vehicular VLC links at visible wavelengths. In [86, 87], a laboratory chamber was employed and the effect of artificially generated rain and fog on the received optical signal for a red LED (that can be potentially used as a taillight) was experimentally evaluated.

A comparison of existing vehicular VLC channel models is given in Table 14.

Table 14: Comparison of existing vehicular VLC channel models

	Method	**Source Modeling**	**Road Surface Modeling**	**Effect of Sun or Artificial Light**	**Weather Conditions**	**Geometry**
[68]	LOS channel	Ideal Lambertian	Not considered	Ambient light	Not considered	- I2V - Isolated geometry
[69]	LOS channel	Ideal Lambertian	Not considered	Not considered	Not considered	- I2V - Isolated geometry
[70]	LOS channel	Ideal Lambertian	Not considered	Ambient light	Not considered	- I2V - Isolated geometry
[71]	LOS channel	Ideal Lambertian	Not considered	Artificial light source	Not considered	- I2V - Isolated geometry
[72] [73]	Monte Carlo ray tracing	Measured headlamp and street lamp	Fixed reflectance	Not considered	Not considered	- V2V, V2I and I2V - Surrounding objects
[74]	Piecewise Lambertian channel	Measured scooter taillight	Not considered	Ambient light	Not considered	- V2V - Isolated geometry
[75] [76]	Geometric-based channel model	Measured headlamp	Wet and dry road surface	Ambient light	Not considered	- V2V - Isolated geometry
[77]	Measured channel	Measured headlamp and taillight	Real-world road environment	Ambient light	Not considered	- V2V - Car-following setting
[78]	Measured channel	Measured fog light	Real-world road environment	Ambient light	Not considered	- V2V - Isolated geometry

[79]	Measured channel	Measured brake light	Real-world road environment	Not considered	Not considered	- V2V - Isolated geometry
[80]	Measured channel	Measured fog light	Real-world road environment	Not considered	Not considered	- V2V - Isolated geometry
[81]	Measured channel	Measured headlamp	Real-world road environment	Ambient light	Not considered	- V2V - Isolated geometry
[82]	Measured channel	Measured headlamp	Real-world road environment	Ambient light	Not considered	- V2V - Car-following setting
[83]	Measured channel	Measured brake light	Real-world road environment	Ambient light	Not considered	- V2V - Car-following setting
[84]	Measured channel	Measured headlamp	Real-world road environment	Ambient light	Not considered	- V2V - Isolated geometry
[85]	Measured channel	Measured headlamp	Real-world road environment	Ambient light	Not considered	- V2V - Car-following setting
[86]	Measured channel	Measured taillight	Not considered	Not considered	Rainy weather	- V2V - Isolated geometry
[87]	Measured channel model	Measured taillight	Not considered	Not considered	Foggy weather	- V2V - Isolated geometry

3.3 Methodology for Vehicular VLC Channel Modeling

Fig. 35 provides an overall summary of major steps followed in the proposed channel modeling methodology [20]. For vehicular channel modeling, we use a similar channel modeling methodology based on Zemax® as adopted in indoor channel modeling. It should be however noted that there exist differences between indoor and outdoor environments. For example, the asymmetrical pattern of headlamp and street lights, reflections from road surfaces and weather conditions should be carefully considered in channel modeling.

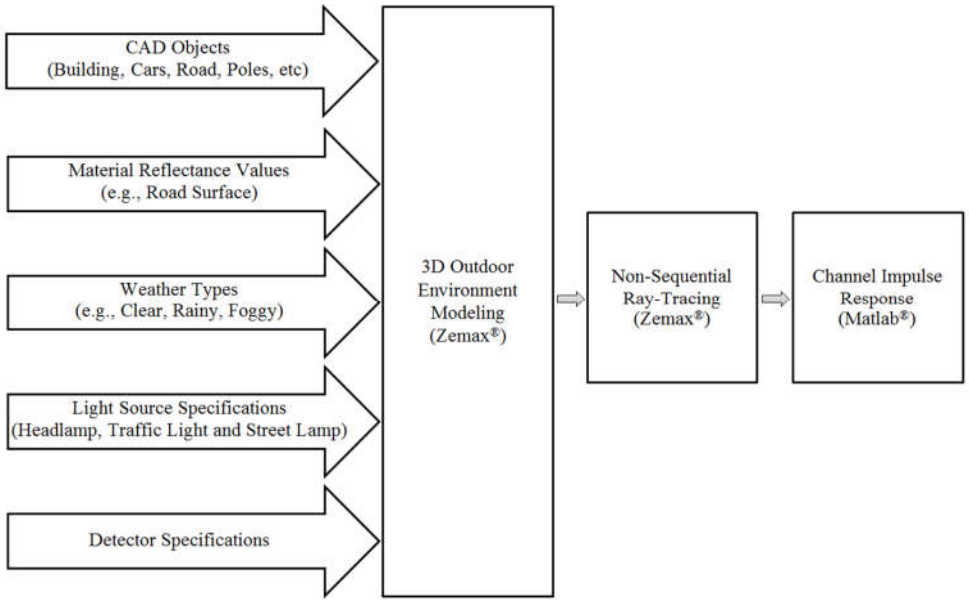

Figure 35: Steps in vehicular VLC channel modeling and characterization

We first construct the simulation platform of the outdoor environment integrating the CAD models of building, vehicles and any other objects within. We further specify the type of object surface materials (coating) and the types of reflections, i.e., purely diffuse, specular and mixed reflections. The specific type of reflection is defined by "scatter fraction" parameter. The reflectance of road surface depends on its nature and physical state, and it also changes with weather conditions [76]. For example, a large amount of specular reflection may occur for wet or moist road surfaces. International Commission on Illumination (CIE) classified the road surfaces into different classes for a range of road surface materials and wet conditions which can be found in Table 15 [91].

Table 15: Road surface classifications

Class	Road Surface Composition	Mode of Reflectance
R1	Asphalt with aggregate including a minimum of 15% artificial brightener aggregate	Mostly diffuse
R2	Asphalt with aggregate including a minimum of 60% gravel sized larger than 10 mm	Mixed diffuse and specular
R3	Asphalt with dark aggregate-the surface becomes rough after several months of use	Slightly specular
R4	Very smooth asphalt	Mostly specular

Mie scattering is used to model clear, rainy and foggy weather conditions with different visibilities [3, Chapter 3]. "Bulk scatter" method in the software allows providing the input parameters "particle index" (the refractive index of particles), "size" (the radius of the spherical particles) and "density" (the density of particles). The characteristics of various weather types are listed in Table 16.

Table 16: Characteristics of various weather types

	Particle Index	Size (μm)	Density (cm^{-3})
Clear	1.000277	10^{-4}	10^{19}
Rain	1.33	100	0.1
Fog, $V = 50$ m	1.33	10	124.6
Fog, $V = 10$ m	1.33	10	622.6

After we create the simulation environment, we use the built-in ray tracing function to determine the CIR. The non-sequential ray tracing tool generates an output file, which includes the detected power and path lengths from source to detector for each ray. We import this file to Matlab® and, using this information, we can express the CIR as (2).

As an initial study, we first consider a vehicular VLC scenario shown in Fig. 36. In this scenario, there is a crossroad where vehicles run in four directions. There are also

buildings, traffic lights and street lamps. We assume that coating materials of buildings, traffic light poles and street lamp poles are respectively concrete, aluminum metal and steel metal. The coating material of cars is considered as black and olive green gloss paint. The road is assumed to be asphalt satisfying R3 class.

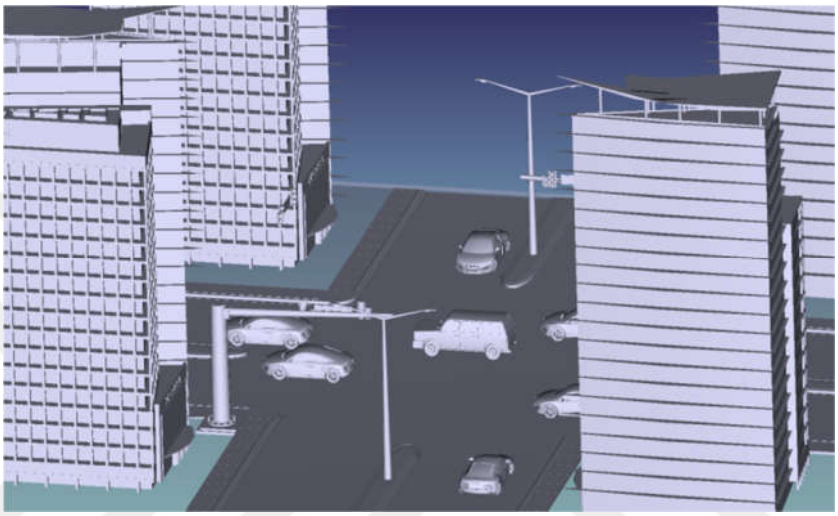

Figure 36: Crossroad scenario under consideration

We use the LED traffic signal produced by the Excellence Opto Inc. [92]. Relative spectral power distribution and relative intensity distributions of traffic light are provided in Fig. 37. In order to see the overall shape of luminaire's light distribution, different cross sections of light intensity is shown in Fig. 37.b, i.e., C0°-C180°, C90°-C270° and C135°-C315° planes are respectively indicated by red, blue and green color. These are however not distinguishable from each other for this particular traffic light. This is result of the fact that the commercial traffic lights have symmetrical intensity distributions.

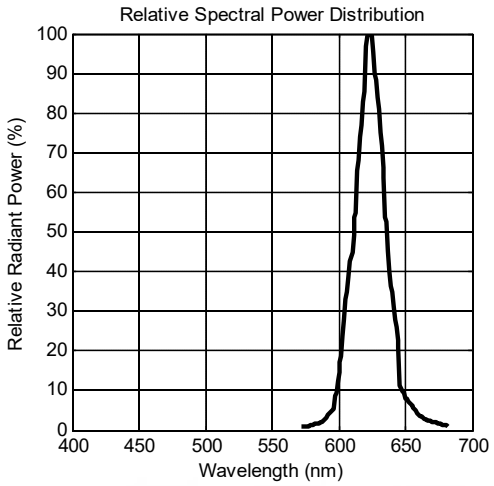

(a)

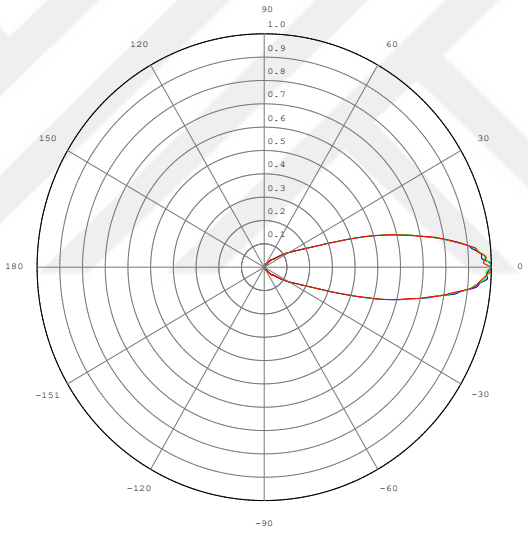

(b)

Figure 37: (a) Relative spectral power distribution and (b) relative intensity distributions of the traffic light

As for the street lamp, we use a locally produced street lamp whose relative spectral power distribution and relative intensity distributions are provided in Fig. 38. Different cross sections of street lamp intensity is shown in Fig. 38.b, i.e., C0°-C180°, C90°-C270° and C135°-C315° planes are respectively indicated by red, blue and green color.

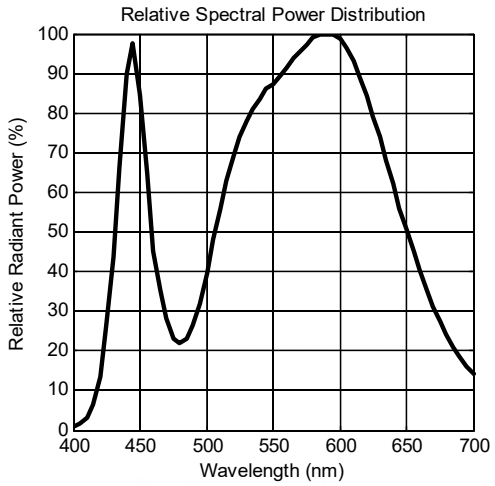

(a)

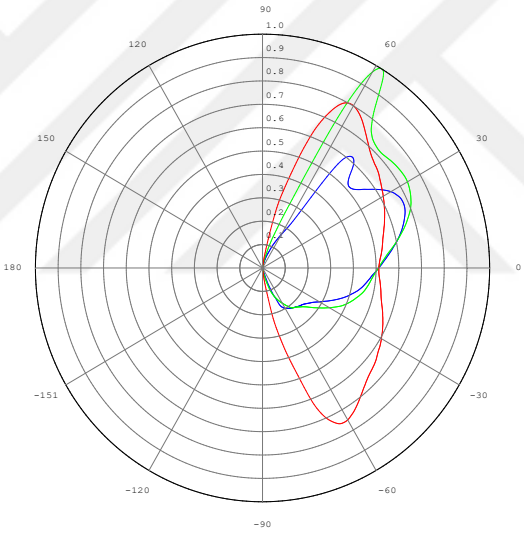

(b)

Figure 38: (a) Relative spectral power distribution and (b) relative intensity distributions of the street lamp

We use a low beam headlamp (located in the front side of the vehicle) Philips Luxeon Rebel [93] with the relative spectral power distribution shown in Fig. 39. Due to asymmetrical intensity distribution of luminaire [94], different cross sections of low beam headlamp intensity is shown in Fig. 39.b, i.e., C0°-C180°, C90°-C270° and C135°-C315° planes are respectively indicated by red, blue and green color.

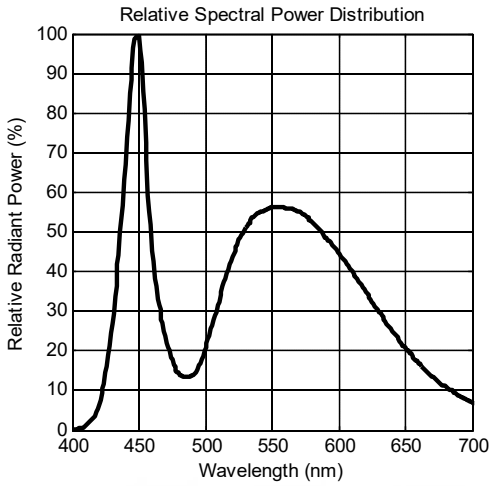

(a)

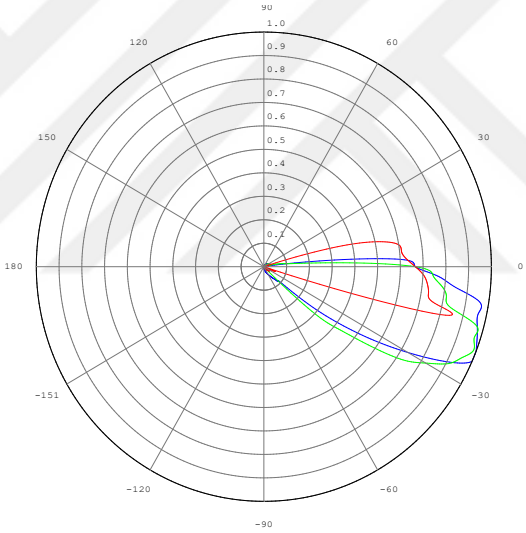

(b)

Figure 39: (a) Relative spectral power distribution (b) relative intensity distributions of low beam headlamp

In order to evaluate the CIR, we consider a total of three configurations, i.e., vehicle-to-vehicle, traffic light-to-vehicle and street lamp-to-vehicle.

3.3.1 Vehicle-to-Vehicle Configuration

In Fig. 40.a., we consider a V2V link in the crossroad scenario. Two low beam headlamps in the source vehicle denoted as S1 and S2 serve as transmitters (Fig. 40.b).

Two photodetectors denoted as D1 and D2 are placed in the back side of the destination vehicle and serve as the receivers (see Fig. 40.c). Each photodetector has an area of 1 cm^2 and FOV of 35°. Two cars are separated from each other by 10 meters. Let $h_{S_mD_n}$, $m = 1,2$ and $n = 1,2$ denote the CIRs obtained for V2V link. These are provided in Fig. 41. The corresponding channel DC gain, path loss and RMS delay spread are obtained and provided in Table 17. It is observed from Fig. 41 that $h_{S_2D_1}$ has the largest amplitude among others. It is due to this fact that the distance between S2→D1 is smaller than the distances between S1→D1, S1→D2 and S2→D2. It is also revealed from Fig. 41 that the CIRs are dominated by LOS component since the reflections from road surface (i.e., asphalt) is small.

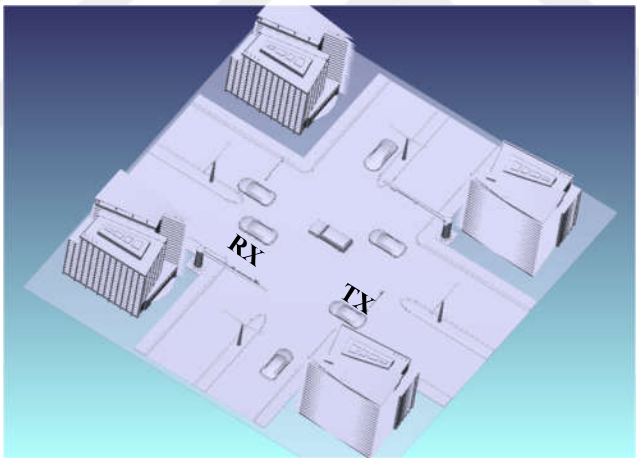

(a)

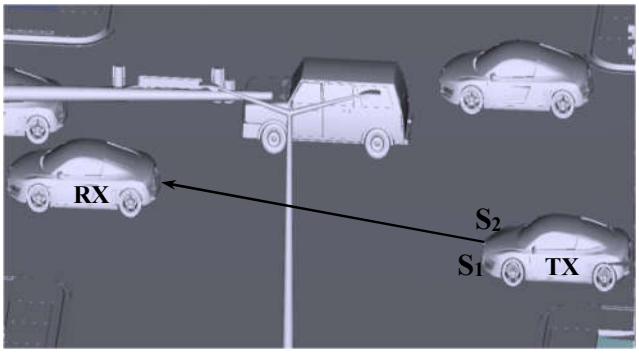

(b)

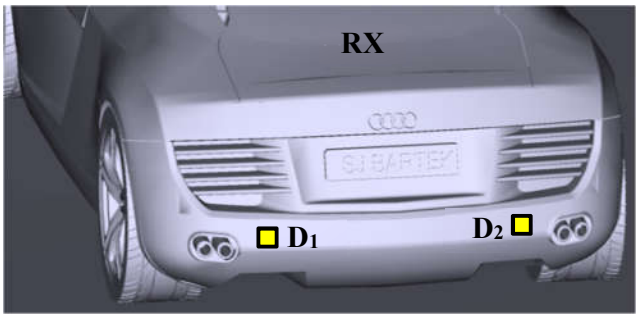

(c)

Figure 40: Vehicle-to-vehicle configuration

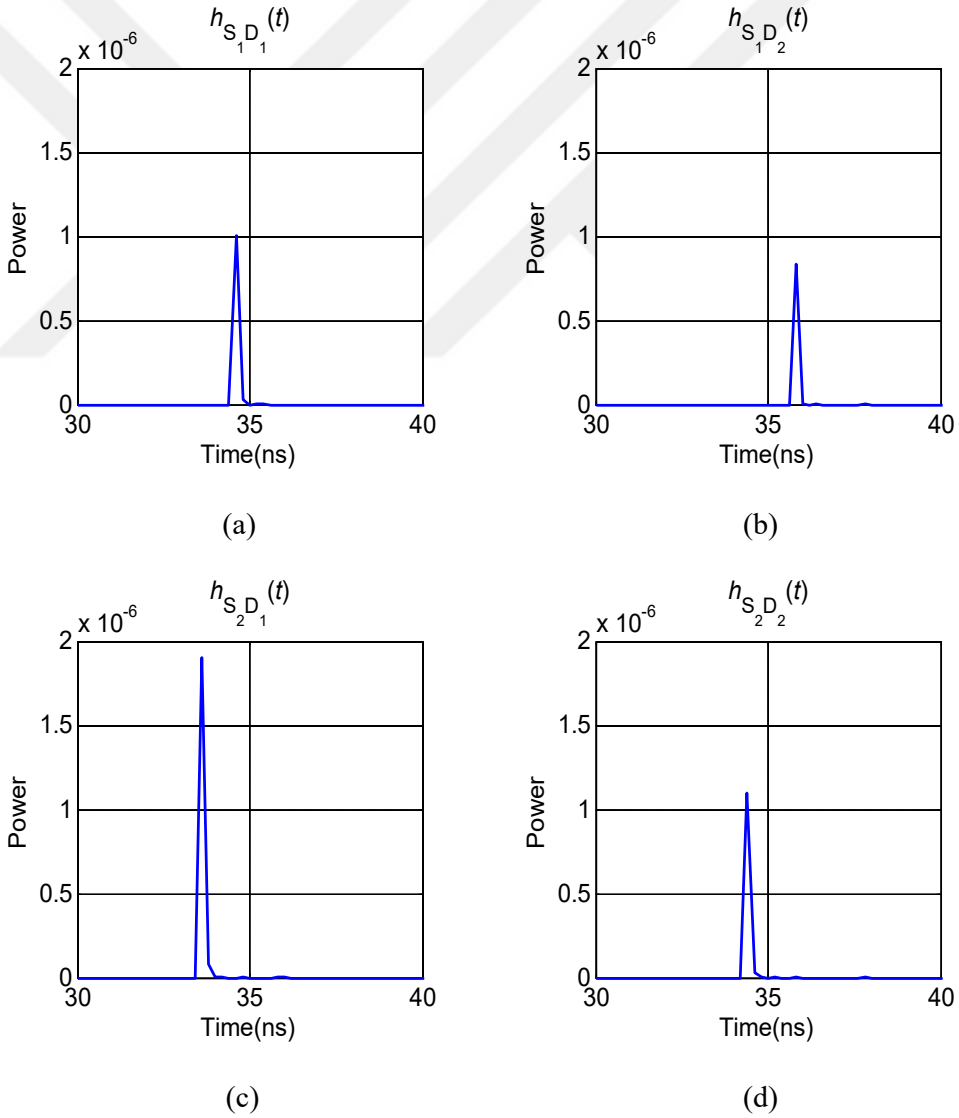

(a) (b)

(c) (d)

Figure 41: CIRs for (a) S1→D1, (b) S1→D2, (c) S2→D1 and (d) S2→D2

Table 17: Channel parameters for V2V link

	τ_{RMS} (ns)	H_0	PL(dB)
S1→D1	0.05	1.02×10^{-6}	59.91
S1→D2	0.10	8.34×10^{-7}	60.78
S2→D1	0.15	1.97×10^{-6}	57.05
S2→D2	0.07	1.13×10^{-6}	59.46

3.3.2 Traffic Light-to-Vehicle Configuration

In Fig. 42.a, we consider a VLC link between a traffic light and vehicle in the crossroad scenario. The traffic light denoted as S serves as the transmitter (Fig. 42.b). Two photodetectors denoted as D1 and D2 are placed in the front side of the destination vehicle and serve as the receivers (see Fig. 42.c). The link distance is about 22.6 meters. Let $h_{\mathrm{SD_n}}$, $\mathrm{n}=1,2$ denote the CIRs. These are provided in Fig. 43. The corresponding channel DC gain, path loss and RMS delay spread for CIRs are obtained and provided in Table 18. It is observed from Fig. 43 that the amplitude of $h_{\mathrm{SD_2}}$ is larger than that of $h_{\mathrm{SD_1}}$. This is a result of the fact that D2 is place at the left hand side of the car and therefore is closer to the traffic light. In terms of path loss, this results in 1 dB difference. Similar to Fig. 41, we observe that the CIRs include only LOS component since the reflections from cars and road surface are small.

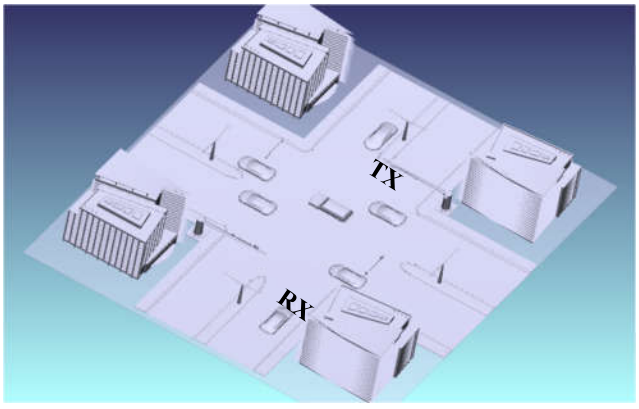

(a)

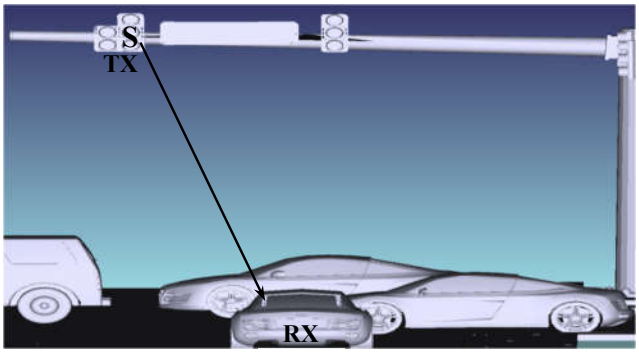

(b)

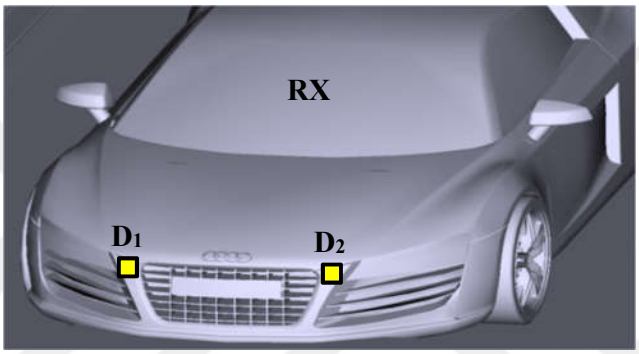

(c)

Figure 42: Traffic light-to-vehicle configuration

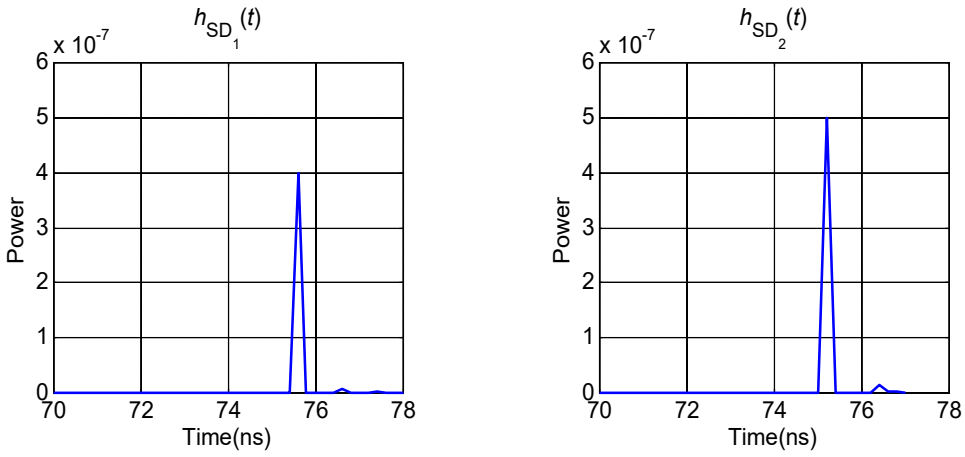

(a) (b)

Figure 43: CIRs for (a) S→D1 and (b) S→D2

Table 18: Channel parameters for traffic light-to-vehicle configuration

	τ_{RMS} (ns)	H_0	PL (dB)
S→D1	0.12	4.06×10^{-7}	63.91
S→D2	0.11	5.06×10^{-7}	62.95

3.3.3 Street Light-to-Vehicle Configuration

In Fig. 44.a, we consider a VLC link between street light and vehicle in the crossroad scenario. The street lights denoted as S1 and S2 serve as the transmitters (Fig. 44.b). Two photodetectors denoted as D1 and D2 are placed in the front side of the destination vehicle and serve as the receivers (see Fig. 44.c). The link distance is about 9 meters. Let $h_{S_mD_n}$, $m=1,2$ and $n=1,2$ denote the CIRs. These are provided in Fig. 45. The corresponding channel DC gain, path loss and RMS delay spread values for CIRs are provided in Table 19. It is observed from Fig. 45 that, similar to Figs. 41 and 43, the CIRs are dominated by the LOS component. It is further observed that the amplitude of $h_{S_1D_1}$ is smaller than that of $h_{S_1D_2}$. Similarly, the amplitude of $h_{S_2D_1}$ is larger than that of $h_{S_2D_2}$. This is a result of the fact that the pattern of street lights is asymmetric as seen in Fig. 38.b.

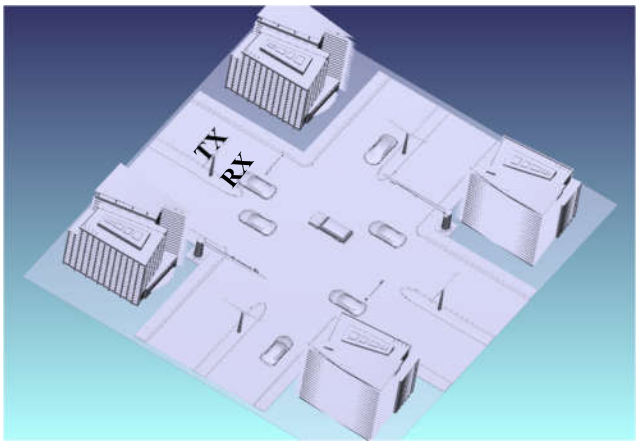

(a)

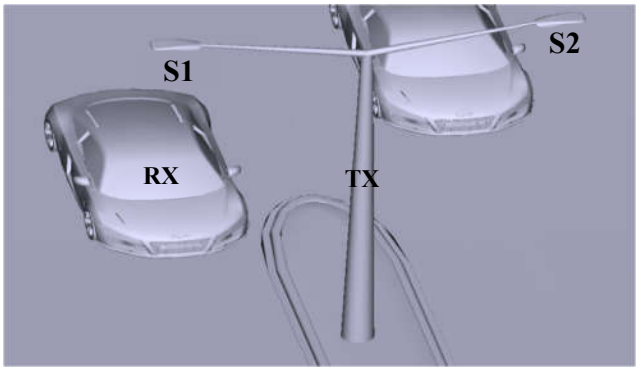

(b)

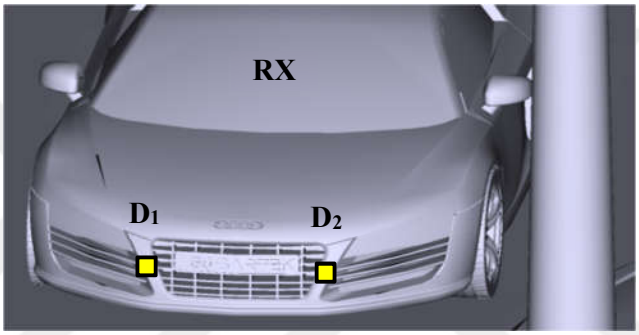

(c)

Figure 44: Street lamp-to-vehicle configuration

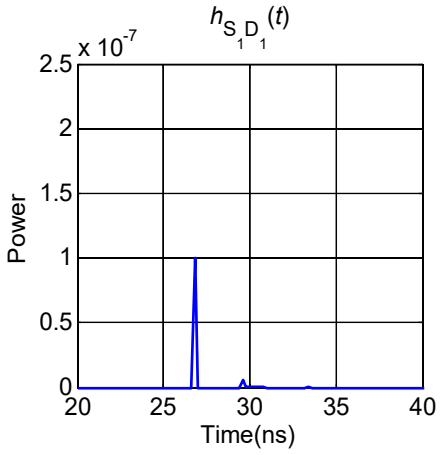

(a)

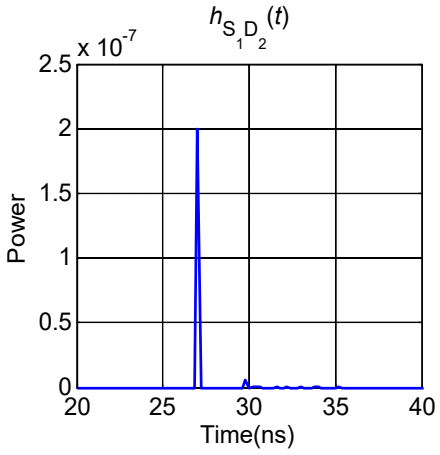

(b)

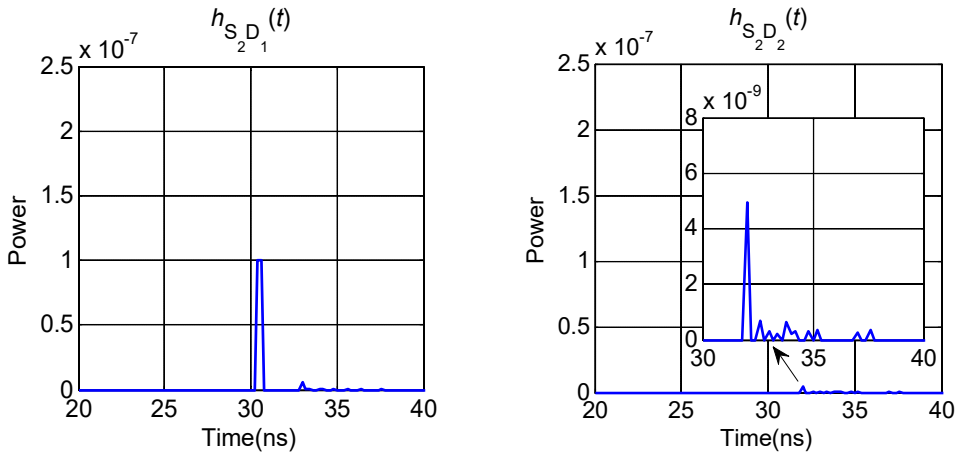

(c) (d)

Figure 45: Optical CIRs for (a) S1→D1, (b) S1→D2, (c) S2→D1, and (d) S2→D2

Table 19: Channel parameters for street lamp-to-vehicle configuration

	τ_{RMS} (ns)	H_0	PL(dB)
S1→D1	27.54	1.09×10^{-7}	3.94
S1→D2	28.24	2.15×10^{-7}	6.43
S2→D1	31.11	2.08×10^{-7}	0.85
S2→D2	33.93	8.97×10^{-9}	4.35

3.4 Effect of Weather Conditions

We consider a V2V scenario shown in Fig. 46. The coating material of vehicles is considered as black gloss paint where we assume the road type R2. This corresponds to asphalt with aggregate including a minimum of 60% gravel sized larger than 10 mm or asphalt with aggregate including a minimum of 10-15% artificial brightener aggregate. For the clear and foggy weathers, we assume mixed diffuse and specular reflections while mostly specular reflections are considered for the wet road in rainy weather [76].

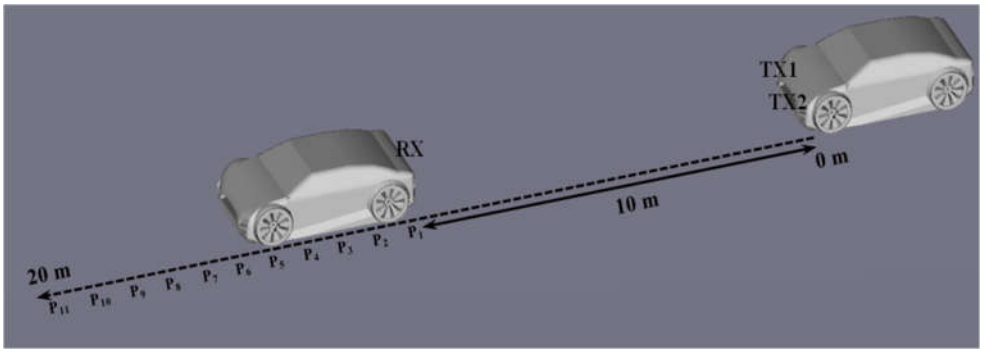

Figure 46: Vehicle-to-vehicle scenario

We use Philips Luxeon Rebel automotive white LED as the high-beam headlamp with the relative spectral power distribution shown in Fig. 47.a. Different cross sections indicated by C0°-C180°, C90°-C270° and C135°-C315° planes are shown in Fig. 47.b. Two headlamps with their total power normalized to unity are placed in the front side of the first vehicle as the transmitters. One photodetector is placed in the back side of the other vehicle as the receiver (see Fig. 46). The PD has a size of 1 cm^2 and FOV of 180°.

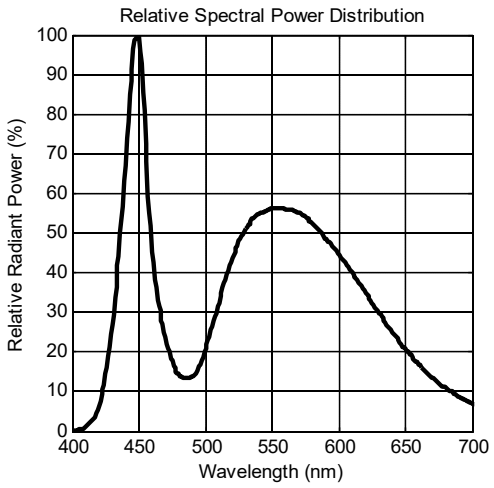

(a)

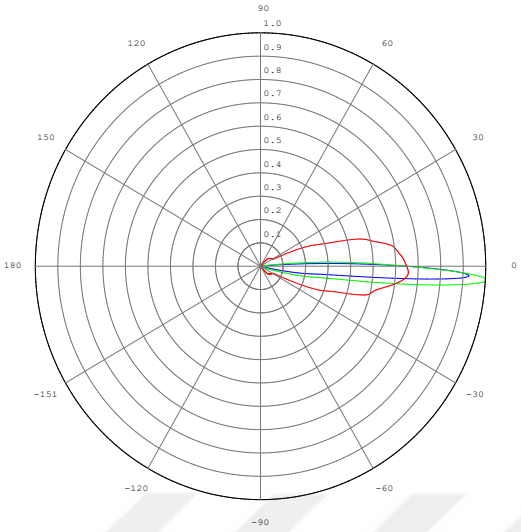

(b)

Figure 47: (a) Relative spectral power distribution and (b) relative intensity distributions of high-beam headlamp

Based on the approach summarized above and for the given scenario, we obtain the CIR for the V2V link under consideration. We assume that the two vehicles are separated from each other initially at a distance 10 meter. We obtain the CIRs through all points with 1 meter interdistance over the driving direction of the car for a range of 10 meter (i.e., CIR samples were taken at P_j, $j = 1, 2, \cdots, 10$). As an example, Fig. 48 presents the CIRs for clear, rainy and foggy weather conditions. It is observed that the amplitude of CIR in rain decreases to 90% of that in clear weather. On the other hand, fog has much more significant impact. For $V = 50$ m, the CIR amplitude decreases to 45% of that in clear weather. It further decreases to 2.7% for $V = 10$ m.

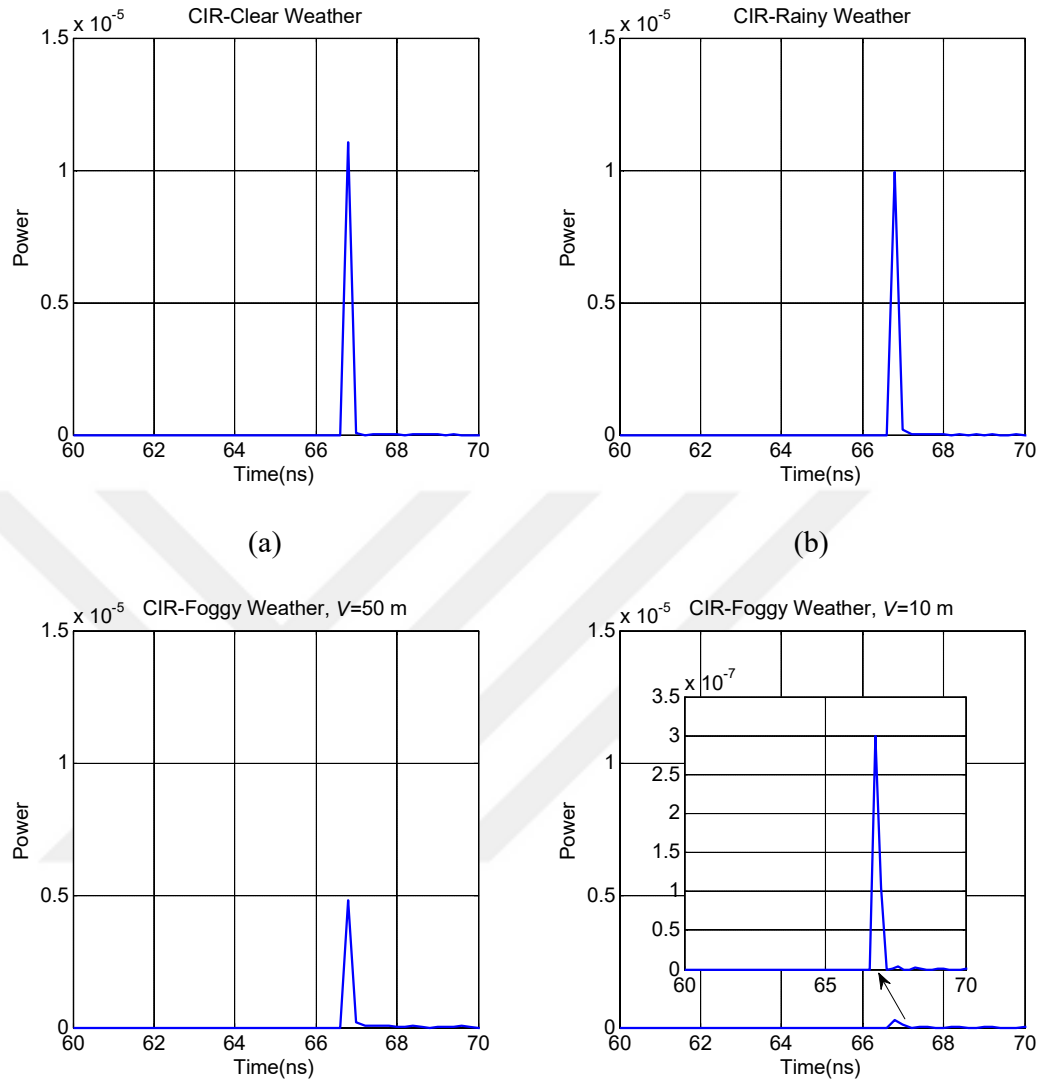

Figure 48: CIRs at distance of 20 m for (a) clear weather, (b) rainy weather, (c) foggy weather with $V = 50$ m and (d) foggy weather with $V = 10$ m

Based on the CIRs, the path loss can be then calculated as (4). In an effort to obtain a closed-form expression for the path loss, we apply curve fitting techniques on our calculated values in (4) based on the minimization of root mean square error. This yields

$$PL(d) = Ad + B, \quad d \geq 10 \text{ m} \tag{16}$$

where the coefficients A and B are found via data fitting and depend on weather type (see Table 20). In Fig. 49, we present the path loss versus distance for different weather conditions under consideration. It is observed that the proposed closed-form expression in (16) provides a good match to simulation results.

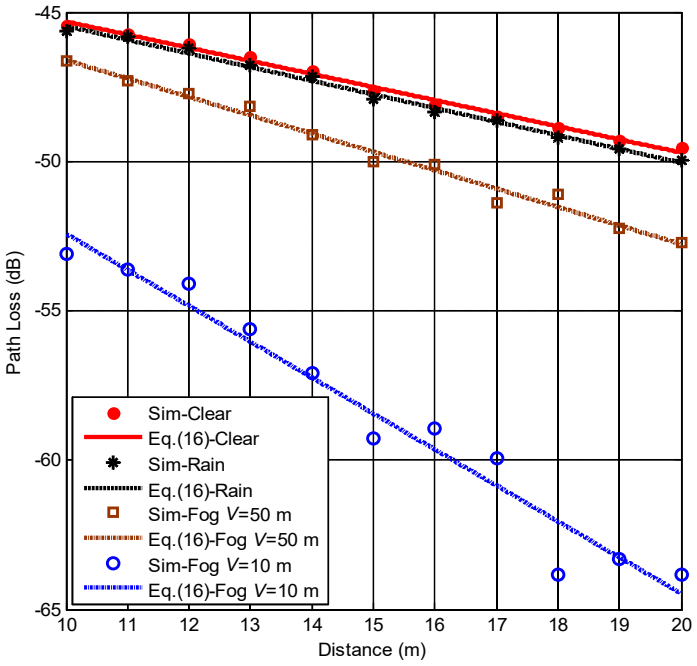

Figure 49: Path loss versus distance for different weather conditions

Table 20: Coefficients in (16) for different weather types

	A	B
Clear	-0.44	-40.93
Rain	-0.46	-40.90
Fog, $V = 50$ m	-0.61	-40.46
Fog, $V = 10$ m	-1.20	-40.38

CHAPTER IV

CHANNEL MODELING AND CHARACTERIZATION FOR UNDERWATER VISIBLE LIGHT COMMUNICATIONS

4.1 Introduction

There has been an increasing demand for high-speed real-time underwater wireless links to accommodate a wide range of applications such as environmental monitoring and pollution control, underwater exploration, scientific data collection, maritime archaeology, offshore oil field exploration, port security and tactical surveillance among others. Although fiber optic links are currently used in some underwater applications to establish real-time communication, their high installation cost, operational difficulties and lack of flexibility for redeployment become restrictive for most cases.

As diverse and data-heavy underwater applications emerge, there has been an increasing attention on underwater VLC [10, 11] as a cost-effective and high-data-rate technology. In the past, some works have been reported on underwater visible light channel modeling which depend on Beer Lambert law [95-97], analytical radiative transfer equations (RTE) model [98, 99], numerical RTE models [100], stochastic models [101-104] and MCRT [105-116].

While earlier works demonstrate the feasibility of UVLC and quantify the path loss for different water types, they are limited to simplified underwater scenarios, i.e., empty sea. In this Chapter, we carry out a channel modeling and characterization study

taking into account the presence of human and man-made objects to investigate the effects of shadowing and blockage. We also develop a closed-form path loss expression as a function of transceiver parameters and the water type.

4.2 Existing UVLC Channel Models

4.2.1 Beer-Lambert Law

Beer-Lambert law describes the light attenuation effects in underwater environment [95, 96] as

$$I = I_0 e^{-c(\lambda)d} \tag{17}$$

where I_0 is the transmitted optical power (intensity), I is the received optical power (intensity) at distance d and $c(\lambda)$ stands for the extinction coefficient. Beer-Lambert law builds upon two implicit assumptions. First, the transmitter and receiver are perfectly aligned. Second, all the scatter photons are lost even though in reality some of the scattered photons can still arrive at the receiver after multiple scattering events. To address the latter issue, a function of two exponentials was proposed [97] to approximate the long distance underwater channel power loss as

$$I = I_0 \left(u_1 e^{-v_1 d} + u_2 e^{-v_2 d} \right) \tag{18}$$

where the parameters u_1, u_2, v_1 and v_2 are calculated by the least mean square (LMS) fitting algorithm to the simulation data obtained from Monte Carlo method.

4.2.2 Radiative Transfer Equations (RTE)

The propagation of light underwater is modelled by the RTE [117, Ch. 9] which basically describes the energy conservation of a light wave traversing a scattering medium

$$\left[\frac{\partial}{v\partial t}+\vec{n}.\nabla\right]L(t,\vec{r},\vec{n})=-cL(t,\vec{r},\vec{n})+b\int_{4\pi}\beta(\vec{n},\vec{n}')L(t,\vec{r},\vec{n})d\vec{n}'+S(t,\vec{r},\vec{n}) \quad (19)$$

where $L(t,\vec{r},\vec{n})$ is the light radiance at time t and position $\vec{r}$ propagating toward direction $\vec{n}$ and $S(t,\vec{r},\vec{n})$ is the source radiance. RTE involves integro-differential equation of time and space which cannot analytically find a general solution [117]. Thus, some approximate analytical solutions [98] have been proposed in recent years. These approximate RTE solutions depend on various simplifying assumptions and the predicted irradiances are typically accurate to a few tens of percent at best, and can be off by an order of magnitude. Besides utilizing analytical solutions, numerical methods are preferred to solve the RTE. In view of this, most of the researchers focus on two basic approaches to develop numerical RTE solvers, i.e., numerical and MCRT methods.

Various numerical methods have been proposed for solving RTE. One of these methods is the invariant embedding solution [118]. Invariant imbedding creates a model by converting the RTE, into a regular differential equation with an initial condition. In the other words, the invariant imbedding is restricted to problems with only one spatial dimension and to simple boundary conditions (e.g., flat surface and bottom). The advantages of this model are computationally efficient and highly accurate that considers the variation of the water inherent optical properties (IOPs) and the boundary conditions at the bottom and the water-air surface. Another method is discrete ordinate model (DOM) [119] which calculates a solution to the RTE by considering the medium as a stack of homogeneous layers. Layers are divided into a finite number of discrete solid angles and the RTE is solved for each of these solid angles individually. In this way, the integro-differential equation is transformed into a system of coupled ordinary differential equations that is solved by the discrete ordinate method. It should be noted

that discrete ordinates can handle aerosol phase functions well and is often used in atmospheric optics, but is not much used for underwater calculations because of the need to resolve highly peaked phase functions and to have many layers if the IOPs vary greatly with depth.

4.2.3 Stochastic Channel Models

As an alternative to RTE stochastic models have also been proposed where the probability of received photon and its arrival time are evaluated. In [101], a stochastic channel model was proposed to represent the spatial-temporal probability distribution of propagated photons for non-scattering and single scattering components of UVLC links. The OTHG function was adopted as the probability density function of light scattering angle to simplify the analysis. In [102], a more general stochastic UVLC channel model was proposed by considering all three components of propagated photons, which include non-scattering, single scattering and multiple scattering components.

4.2.4 MCRT Channel Models

In [105], Monte Carlo approach was used by considering Haltrin & Kattawar model and one-term Henyey-Greenstein (OTHG) SPF. The time dispersion for link ranges up to 100 m in various water types (i.e., pure sea, clear ocean, coastal and harbor) and receiver aperture sizes (i.e., 0.5 cm, 5 cm, 20 cm and 50 cm) was quantified. In [107], the same study in [105] was repeated using this time so-called two-term Henyey-Greenstein (TTHG) SPF to model volume scattering function (VSF) as an enhancement over OTHG SPF.

In [109] and [110], Monte Carlo approach was used based on Haltrin & Kattawar model and Mie scattering phase function. The seawater surface was modeled

using a random variable to investigate the effect of surface collision. A Lambertian model was used for modeling of dispersive effect from sea bottom. The received intensity for various ranges (i.e., 1 m, 5 m and 25 m), particle sizes (i.e., 1 μm, 4 μm and 8 μm), concentration of particles and Lambertian order of transmitter was quantified.

In [111], a multiple-input multiple-output (MIMO) UVLC scenario was considered and intensity under the assumption of Haltrin & Kattawar model and OTHG SPF for coastal and harbor water was computed. Additionally, a closed form expression for channel impulse response using weighted double Gamma function was proposed. In [112] as a continuance of [111], a relatively more realistic SPF (Mobley's particle phase function) was considered and the received intensity and time dispersion for various ranges (i.e., up to 16 m for the harbor and up to 60 m for the coastal water) and receiver field of views (i.e., 20°, 40° and 180°) were obtained. In [113], the path loss of UVLC system for link ranges up to 80 m was quantified assuming various transmitter divergence angles (up to 60°) and receiver field of views (up to 180°) in clear ocean, coastal and harbor water.

A comparison of existing UVLC channel models can be found in Table 21.

Table 21: Comparison of existing underwater VLC channel models

	Method	**Water Modeling**	**Source Modeling**	**Environment Modeling**
[95]	Beer-Lambert law	- Measured data for absorption and scattering coefficients in clear ocean	- Ideal laser source	- No human or objects - Geometric loss modeling - Modeling of sea surface
[96]	Beer-Lambert law	- Haltrin & Kattawar model for absorption and scattering coefficients in clear ocean	- Ideal Lambertian source	- No human or objects - Solar noise modeling
[97]	Modified Beer-Lambert law	- Haltrin & Kattawar model for absorption and scattering coefficients in pure sea and clear ocean	- Ideal Lambertian source	- No human or objects

[98]	Analytical RTE	- Haltrin & Kattawar model for absorption and scattering coefficients in coastal - Mie SPF - Refractive index of water - Refractive index of particles - Size and density of different particles - Salinity and temperature	- Left-handed circular polarized (LHCP) light	- No human or objects
[99]	Analytical RTE	- Measured data for absorption and scattering coefficients in coastal and harbor - Measured SPF based on Petzold's data	- Ideal laser source	- No human or objects - Modeling of sea surface
[100]	Numerical RTE	- Measured data for absorption and scattering coefficients in coastal and harbor - OTHG SPF	- Ideal laser source	- No human or objects
[101]	Stochastic model	- Measured data for absorption and scattering coefficients in coastal water - OTHG SPF	- Ideal laser source	- No human or objects
[102]	Stochastic model	- Measured data for absorption and scattering coefficients in coastal and harbor - OTHG SPF	- Ideal laser source	- No human or objects
[103]	Stochastic model	- Measured data for absorption and scattering coefficients in coastal and harbor - OTHG SPF	- Ideal laser source	- No human or objects -Considering misalignment
[104]	Stochastic model	- Haltrin & Kattawar model for absorption and scattering coefficients in coastal and harbor - OTHG SPF	- Ideal laser source	- No human or objects
[105]	Monte Carlo photon tracing	- Haltrin & Kattawar model for absorption and scattering coefficients in pure sea, clear ocean, coastal and harbor - OTHG SPF	- Ideal laser source	- No human or objects
[106]	Monte Carlo photon tracing	- Measured data for absorption and scattering coefficients in clear ocean, coastal and harbor - OTHG SPF	- Gaussian laser source	- No human or objects
[107]	Monte Carlo photon tracing	- Haltrin & Kattawar model for absorption and scattering coefficients in pure sea, clear ocean, coastal and harbor - TTHG SPF	- Ideal laser source	- No human or objects
[108]	Monte Carlo photon tracing	- Measured data for absorption and scattering coefficients in clear ocean and coastal	- Ideal laser source	- No human or objects - Modeling of sea surface

		- OTHG SPF		
[109]	Monte Carlo ray tracing	- Measured data for absorption and scattering coefficients in pure seawater - Mie SPF (considering uniform particle size distribution) - Refractive index of water - Size and density of different particles	- Ideal Lambertian source	- No human or objects - Wavelength independent reflectance values for sea bottom
[110]	Monte Carlo ray tracing	- Measured data for absorption and scattering coefficients in pure seawater - Mie SPF (considering uniform particle size distribution) - Refractive index of water - Size and density of different particles	- Ideal Lambertian source	- No human or objects - Wavelength independent reflectance values for sea bottom
[111]	Monte Carlo photon tracing	- Measured data for absorption and scattering coefficients in coastal and harbor - OTHG SPF	- Ideal laser source	- No human or objects
[112]	Monte Carlo photon tracing	- Measured data for absorption and scattering coefficients in coastal and harbor - Mobley's SPF	- Ideal laser source	- No human or objects
[113]	Monte Carlo ray tracing	- Haltrin & Kattawar model for absorption and scattering coefficients in clear ocean, coastal and harbor - Empirical SPF model based on Kopelevich's data	- Ideal laser source	- No human or objects
[114]	Monte Carlo ray tracing	- Measured data for absorption and scattering coefficients in clear ocean, coastal and harbor - Empirical SPF model based on Mobley's data	- Ideal laser source	- No human or objects
[115]	Monte Carlo ray tracing	- Measured data for absorption and scattering coefficients in clear ocean - Empirical SPF model based on Wilson's data	- Laser source with various beam patterns	- No human or objects
[116]	Monte Carlo photon tracing	- Measured data for absorption and scattering coefficients in clear ocean, coastal and harbor - Measured SPF based on Petzold's data	- Ideal laser source	- No human or objects

4.3 Optical Characterization of Water and Particles

Before we present our underwater VLC channel modeling approach, we provide preliminaries on the optical characterization of water and particles. The inherent optical properties (IOP) of water are the optical parameters that only depend on the transmission medium itself, more specifically the composition of that medium and particulate substances present within it.

We can categorize underwater environments based on the distance from seashore, chlorophyll concentration, and depth, the latter which relates to sunlight penetration. According to depth, we can categorize the underwater environments into three groups, namely surface zone (0 m - 200 m), transition zone (200 m - 1000 m) and deep zone (1000 m - 4000 m) [120, 121]. According to the distance from seashore, we can group the underwater environments as shallow ocean and open ocean [120, 121]. Finally, according to chlorophyll concentration, we have four categorizations, i.e., pure sea, clear ocean, coastal and harbor [11]. The chlorophyll concentration is the main parameter that determines the absorption and scattering coefficients whose sum yields the extinction coefficient. Turbid water results in large extinction coefficient value while the extinction coefficient in non-turbid water takes small values. Based on typical chlorophyll concentrations, pure sea and clear ocean are therefore considered as non-turbid water and the coastal and harbor can be considered as turbid water. Fig. 50 provides an overall summary of these categorizations.

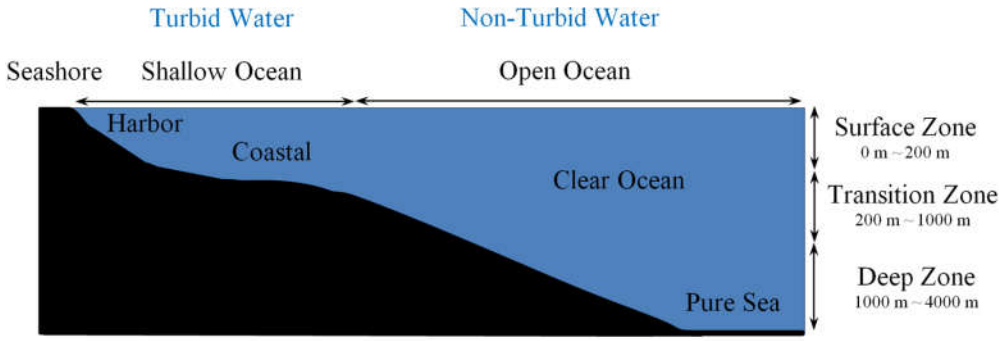

Figure 50: Classification of marine environments

Absorption and scattering coefficients are the two major IOPs that determine the underwater light attenuation. Absorption is an energy transfer process in which photons lose their energy and convert it into other forms, such as heat and chemical (photosynthesis). Scattering, on the other hand, refers to the deflection of light from its original path. In water, deflections can be caused by the particles of size comparable to the wavelength (diffraction), or by the particulate matters with refraction index different from that of the water (refraction).

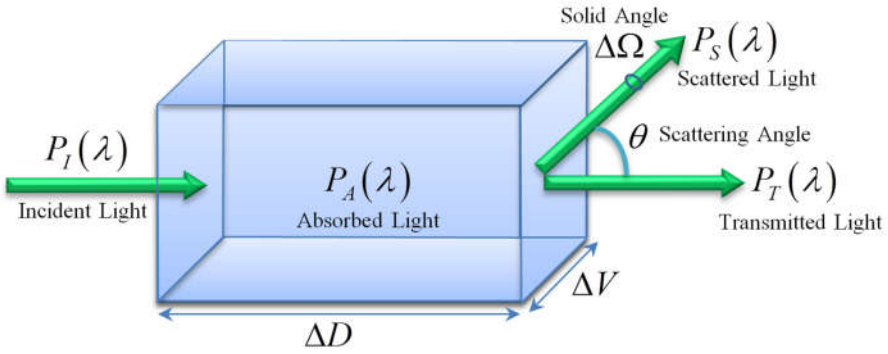

Figure 51: Geometry of inherent optical properties for a volume

As illustrated in Fig. 51, assume that a volume of water ΔV with thickness ΔD is illuminated by a collimated light beam with wavelength λ. We denote the power of incident light as P_I. A portion of the incident light power P_A is absorbed by water, and another portion of light power P_S is scattered. P_T is the remaining light power that will

propagate through medium. According to the law of conservation, we have [122]

$$P_I = P_A + P_S + P_T \tag{20}$$

Based on (20), we define the ratio between absorbed power and incident power P_A/P_I as absorbance. Similarly, the fraction between scattered power and incident power P_B/P_I is defined as scatterance. The absorption coefficient and the scattering coefficient are then calculated by taking the limit of absorbance and scatterance as water thickness (ΔD) becomes infinitesimally small [122], i.e.,

$$a(\lambda) = \lim_{\Delta D \to 0} \frac{P_A}{P_I \Delta D} \tag{21}$$

$$b(\lambda) = \lim_{\Delta D \to 0} \frac{P_S}{P_I \Delta D} \tag{22}$$

The overall attenuation can be then described by the extinction coefficient $c(\lambda)$ which can be expressed as

$$c(\lambda) = a(\lambda) + b(\lambda) \tag{23}$$

In addition to the water molecules, different dissolved particles or suspending particles in water affect absorption and scattering. These include various dissolved salts, detrital and mineral components, colored dissolved organic matters, and phytoplanktons. The spectral absorption and scattering coefficient for a specific marine environment can be calculated by adding the contribution of each class of particles. Among these, phytoplanktons (a group of photosynthesizing microorganisms) determine the optical properties of most oceanic waters because their chlorophyll and related pigments strongly absorb light in the blue and red spectral ranges [122].

The commonly deployed bio-optical models to calculate absorption and scattering coefficients are proposed by Gordon & Morel [122] and Haltrin & Kattawar

[123]. In the Gordon & Morel model, the absorption and scattering coefficients are functions of wavelength and chlorophyll concentration. Mathematically speaking, they are respectively given by [122]

$$a(\lambda)=\left[a_w(\lambda)+0.06a_c^{*'}(\lambda)C_c^{\,0.65}\right]\left[1+0.2\exp\left(-0.014(\lambda-440)\right)\right] \tag{24}$$

$$b(\lambda)=\left(\frac{550}{\lambda}\right)0.30C_c^{\,0.62} \tag{25}$$

where C_c is the chlorophyll concentration with unit in mg/m^3 (see Appendix for calculation of C_c based on depth profiles), a_w is the absorption coefficient of pure water with unit in m^{-1} and $a_c^{*'}$ is a non-dimensional chlorophyll-specific absorption coefficient. Fig. 52 illustrates the absorption, scattering and extinction coefficients versus wavelength in the visible spectrum of 400 nm-700 nm based on (24) and (25) assuming that chlorophyll concentration take values of $C_c=0.005$, 0.31, 0.83 and 5.9 mg/m^3 respectively for the pure sea, clear ocean, coastal and harbor [122].

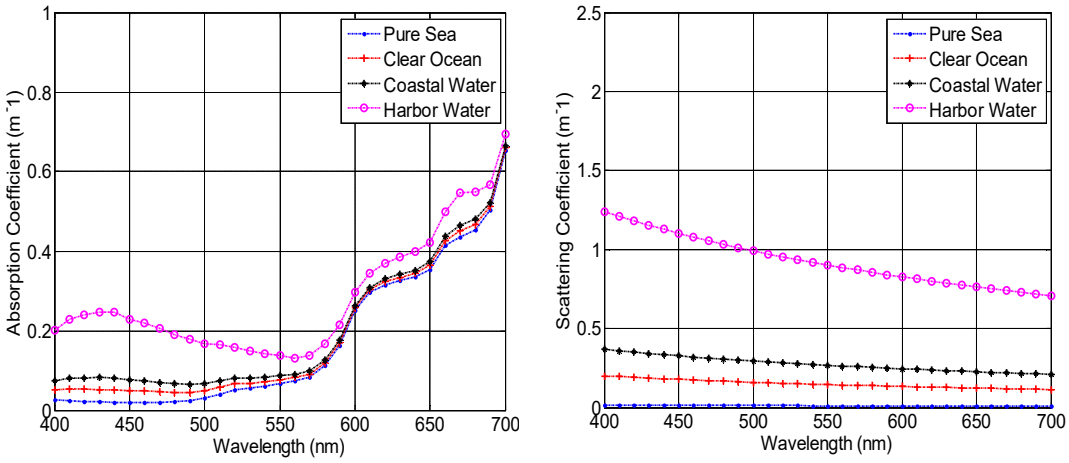

(a) (b)

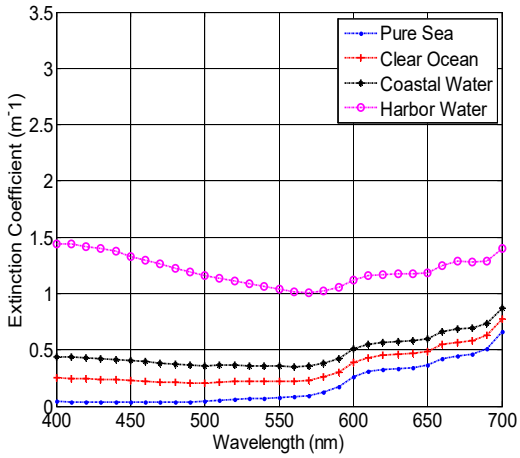

(c)

Figure 52: (a) Absorption, (b) scattering and (c) extinction coefficients versus wavelength for different water types based on Gordon & Morel model

In the Haltrin & Kattawar model [123], the absorption and scattering coefficients are functions of different biological factors. The overall absorption is determined by the absorptions of pure water, chlorophyll-*a*, (i.e., the main substance that comprises phytoplankton) and humic and fulvic acids (both of which act as nutrients for phytoplankton). The overall scattering is determined by the scattering of pure water and particulate substances. The latter is separated into small and large particles, each with a different statistical distribution and scattering strength. In the Haltrin & Kattawar model, the absorption coefficient is expressed as a sum of absorption spectra multiplied by their respective concentrations as

$$a(\lambda) = a_w(\lambda) + a_f^0 \exp(-k_f \lambda) C_f + a_h^0 \exp(-k_h \lambda) C_h + a_c^0(\lambda)\left(C_c / C_c^0\right)^{0.602} \qquad (26)$$

where a_f^0 is fulvic acid specific absorption coefficient ($a_f^0 = 35.959\,\mathrm{m^2/mg}$), k_f is the fulvic acid exponential coefficient ($k_f = 0.0189\ \mathrm{nm^{-1}}$) and C_f is the concentration of fulvic acid in $\mathrm{mg/m^3}$. In the third term of (26), a_h^0 is the humic acid specific absorption coefficient ($a_h^0 = 18.828\,\mathrm{m^2/mg}$), k_h is the humic acid exponential coefficient (

$k_h = 0.0110$ nm^{-1}) and C_h is the concentration of humic acid in mg/m^3. In the fourth and last term of (26), C_c is the concentration of chlorophyll-*a* in mg/m^3 (see [124] for calculation of C_c based on depth profiles), $C_c^0 = 1$ mg/m^3 is the reference concentration and a_c^0 is the specific chlorophyll absorption coefficient (m^2/mg) calculated as $a_c^0(\lambda) = A(\lambda) C_c^{-B(\lambda)}$ where coefficients A and B are empirical constants, see [125]. It should be further noted that C_f and C_h are given in terms of concentration of chlorophyll-*a* as $C_f = 1.74098 C_c \exp\left(0.12327\left(C_c / C_c^0\right)\right)$ and $C_h = 0.19334 C_c \exp\left(0.12343\left(C_c / C_c^0\right)\right)$ [126].

In the Haltrin & Kattawar model, the scattering coefficient as a function of wavelength and chlorophyll concentration is given by [123]

$$b(\lambda) = b_w(\lambda) + b_s^0(\lambda) C_s + b_l^0(\lambda) C_l \tag{27}$$

where b_w is the pure water scattering coefficient (m^{-1}), b_s^0 is the scattering coefficient for small particulate matter (m^2/g), b_l^0 is the scattering coefficient for large particulate matter (m^2/g), C_s is the concentration of small particles (g/m^3) and C_l is the concentration of large particles (g/m^3). The latter two are given in terms of concentration of chlorophyll-*a* as $C_s = 0.01739 C_c \exp\left(0.11631\left(C_c / C_c^0\right)\right)$ and $C_l = 0.76284 C_c \exp\left(0.03092\left(C_c / C_c^0\right)\right)$. The spectral dependencies for the scattering coefficients of small and large particulate matter are given by

$$b_w(\lambda) = 0.005826\left(400/\lambda\right)^{4.322} \tag{28}$$

$$b_s^0(\lambda) = 1.1513\left(400/\lambda\right)^{1.7} \tag{29}$$

$$b_l^0(\lambda) = 0.3411005826\left(400/\lambda\right)^{0.3} \tag{30}$$

The overall attenuation can be then described by the extinction coefficient which can be expressed as the sum of absorption and scattering coefficients.

Fig. 53 illustrates the absorption, scattering and extinction coefficients versus wavelength for different water types based on Haltrin & Kattawar model assuming that chlorophyll concentration take values of $C_c = 0.005,\ 0.31,\ 0.83$ and $5.9\ \text{mg/m}^3$ respectively for the pure sea, clear ocean, coastal and harbor [122].

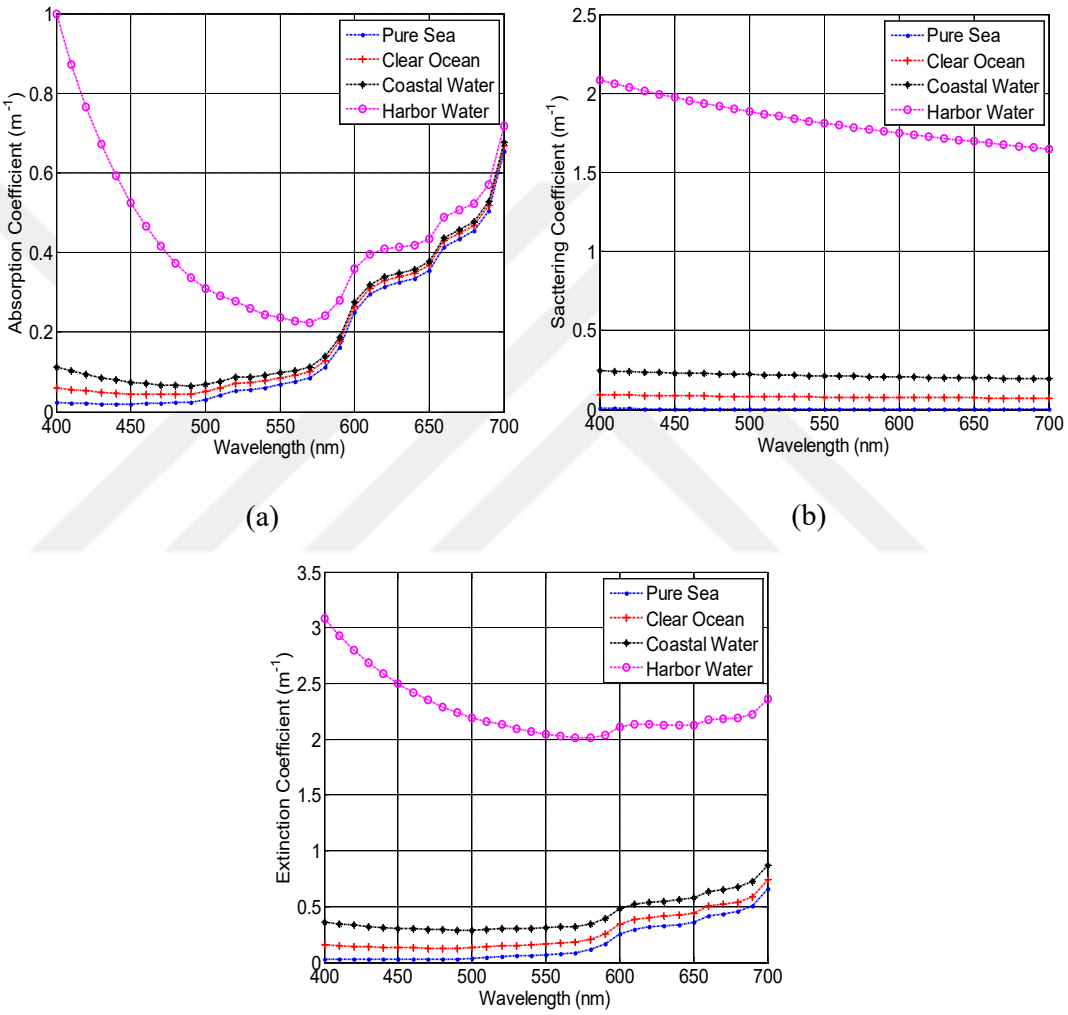

Figure 53: (a) Absorption, (b) scattering and (c) extinction coefficients versus wavelength for different water types based on Haltrin & Kattawar model

To have a clear comparison between Gordon & Morel model and Haltrin & Kattawar model, we present Fig. 54 where the extinction coefficients are plotted for both models in different water types.

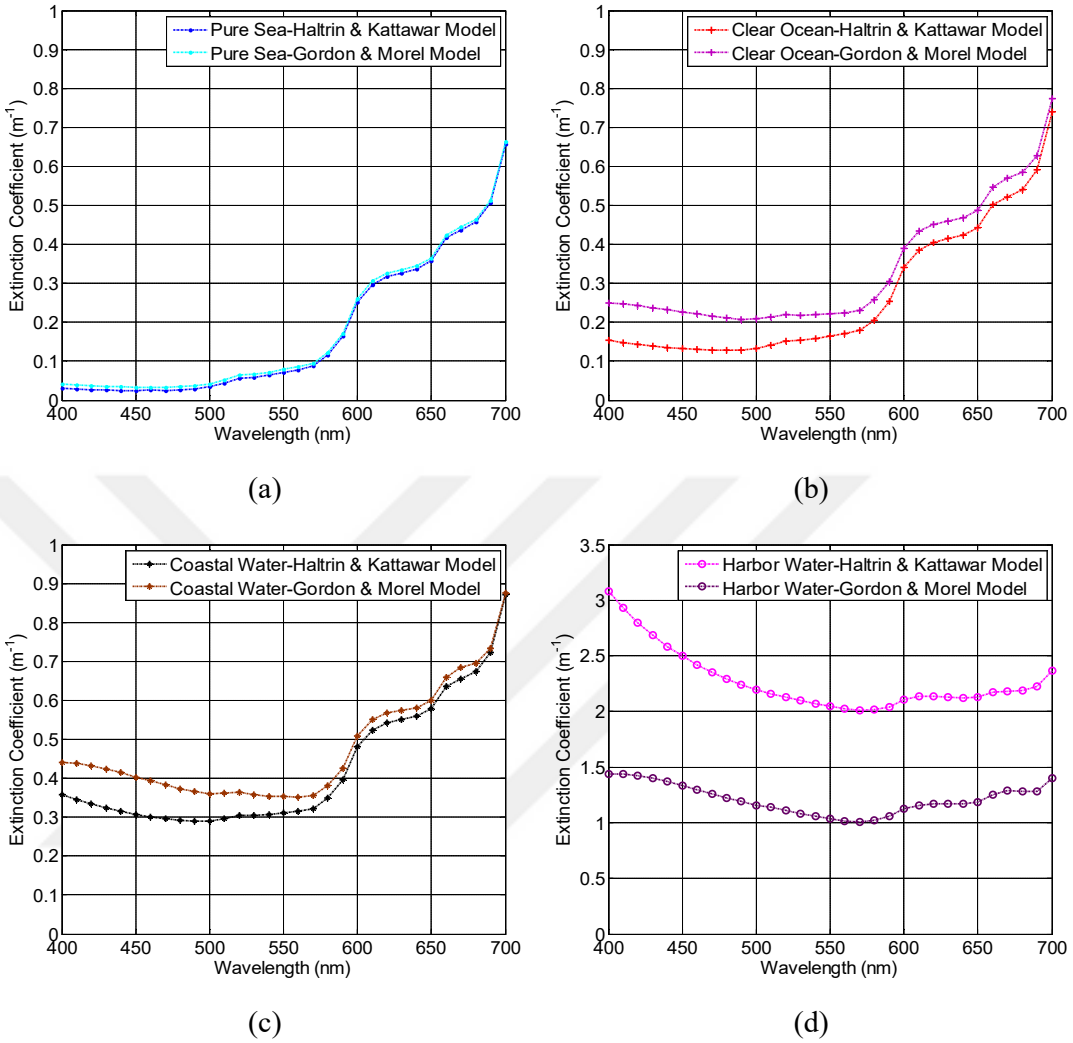

Figure 54: Extinction coefficients for (a) pure sea, (b) clear ocean, (c) coastal water and (d) harbor water

It is observed from Fig. 54 that the extinction coefficients obtained with Gordon & Morel and Haltrin & Kattawar models coincide for pure sea with a small difference while some discrepancy is observed in all other water types. In particular, in non-turbid and low turbid waters (pure sea, clear ocean and coastal), Gordon & Morel model provides overestimate of those ones obtained with Haltrin & Kattawar model. On the other hand, in high turbid waters (harbor), Gordon & Morel model provides an underestimate with respect to Haltrin & Kattawar model.

Fig. 54 demonstrates that the extinction coefficients in non-turbid and low turbid waters typically increase with the increase in wavelength. On the other hand, the extinction coefficient of high turbid water has a decreasing trend when the wavelength increases. From comparison of Figs. 54.a-d, it can be seen that the extinction coefficient increases from pure sea to harbor. It is due to this fact that the chlorophyll and related pigments can increase the turbidity of the water, and thus reduce the achievable propagation distance.

It can be concluded from Fig. 54 that the minimum extinction window (which consists of the smallest values of extinction coefficient in 50 nm window [10]) will be different for various water types. Ideal transmission wavelengths for different water types are listed in Table 22.

Table 22: Operating wavelength for different water types

Water Type	Chlorophyll Concentration	Humic and Fulvic Concentration	Operating Wavelength
Pure Sea	Less	Less	430 nm - 480 nm
Clear Ocean	Less	Less	450 nm - 500 nm
Coastal	High	High	460 nm - 510 nm
Harbor	Very High	Very High	540 nm - 590 nm

In order to describe the scattering effects more accurately, VSF is also used. It is defined as [127]

$$\beta(\theta,\lambda) = \lim_{\Delta D \to 0} \lim_{\Delta \Omega \to 0} \frac{P_S(\theta,\lambda)}{\Delta D \Delta \Omega} \tag{31}$$

where $P_S(\theta,\lambda)$ is the fraction of incident power scattered out of the beam through an angle θ into a solid angle $\Delta\Omega$ centered on θ (Fig. 51). VSF is the scattered intensity per unit incident irradiance per unit volume of water. In the view of physics, the VSF can also be interpreted as the differential scattering cross section per unit volume.

Integrating $\beta(\theta,\lambda)$ over all directions (solid angles) gives the scattering coefficient [127] as

$$b(\lambda)=\int \beta(\theta,\lambda)d\Omega=2\pi\int_0^{\pi}\beta(\theta,\lambda)\sin(\theta)d\theta \tag{32}$$

Normalizing (31) with the scattering coefficient, we obtain SPF which is defined as [127]

$$\tilde{\beta}(\theta,\lambda)=\frac{\beta(\theta,\lambda)}{b(\lambda)} \tag{33}$$

4.4 Methodology for UVLC Channel Modeling

A summary of major steps followed in the proposed channel modeling methodology [21] is provided in Fig. 55. For underwater channel modeling, we use a similar channel modeling methodology as adopted in indoor channel modeling. It should be however noted that there exist differences between indoor and underwater environments. The reflection characteristics of the sea surface and sea bottom as well as the water characteristics, i.e., extinction coefficient and scattering phase function of particles, should be precisely considered in channel modeling. We first create a three dimensional simulation environment in Zemax® where the geometry of the underwater environment and the objects therein are defined. The CAD objects can be imported in the simulation platform to model the human beings and any other man-made/natural objects, e.g., underwater vehicles, divers, rocks, etc. Wavelength-dependent reflectance of surface coating for each object in the environment is specified. We further take into account the effects of sea surface and bottom. We assume mud for the sea bottom and consider purely diffuse reflections.

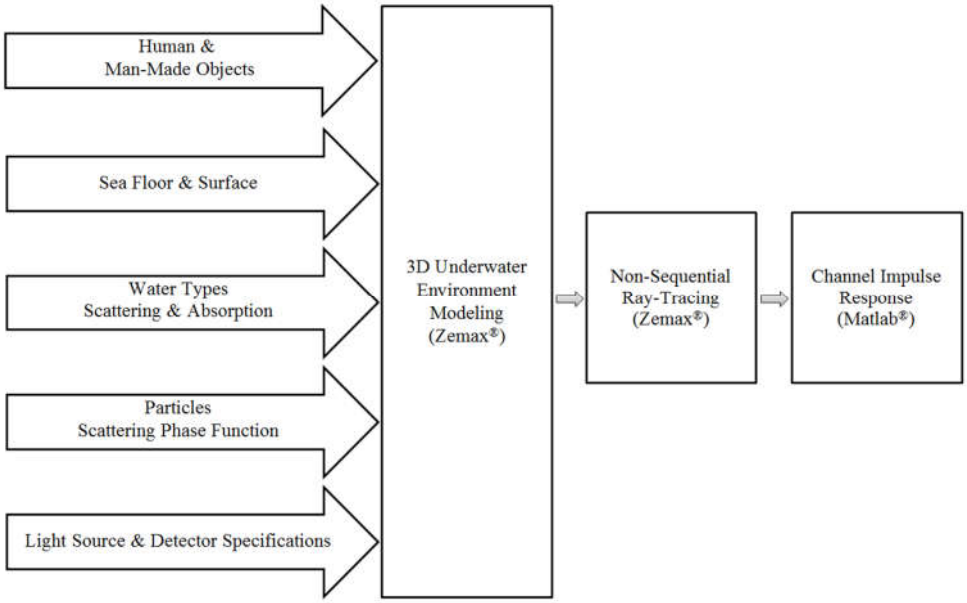

Figure 55: Steps in UVLC channel modeling and characterization

To characterize the reflection and refraction of transmitted rays from the sea surface, we use Fresnel equations respectively given by [95]

$$R_s = \left| \frac{n_1 \cos\theta_i - n_2 \cos\theta_t}{n_1 \cos\theta_i + n_2 \cos\theta_t} \right|^2 \tag{34}$$

$$R_p = \left| \frac{n_1 \cos\theta_t - n_2 \cos\theta_i}{n_1 \cos\theta_t + n_2 \cos\theta_i} \right|^2 \tag{35}$$

where R_s and R_p are the reflectances for s- and p-polarized light, n_1 and n_2 are the refractive indices of incident and refracting medium, and θ_i and θ_t are the incident and refracting angles.

In the second step, we integrate the laser or LED-based light source in the simulation platform. Different types of light sources can be used as UVLC transmitters. A collimated laser beam has very low divergence on the order of milliradians. On the other hand, LED is a diffuse source and transmits its energy over a large spherical section. A semi-collimated source would either be a laser that has been purposefully

diffused or a LED that is focused. The emission pattern and relative spectral power distribution are defined as inputs to the simulation platform for the selected light source. It is also possible to draw the related information for commercially available LEDs from RSM database [46]. As a receiving element, we use a rectangular aperture with specified dimensions and FOV.

In the third step, we define the underwater environment characteristics. The inherent optical properties of water, i.e., absorption, scattering and extinction coefficients are defined based on the Haltrin & Kattawar model [123] and depth profiles of chlorophyll concentration [124] and [128, 129]. To model scattering phase function, we use OTHG [130] formula with three parameters, namely mean free path, photon weight updating and average cosine of scattering angle in all scattering directions. The mean free path parameter defines the average geometric distance traveled by photons before being scattered [122] and it can be calculated as the inverse of extinction coefficient ($1/c(\lambda)$). The interaction between the photon and medium may cause the photon losing weight due to the absorption and scattering. The photon therefore needs to update its weight. The photon weight updating is defined as the ratio of scattering coefficient to extinction coefficient, i.e., ($b(\lambda)/c(\lambda)$).

Once the simulation platform is constructed based on the three steps summarized above, non-sequential ray tracing tool is run to calculate the detected power and path lengths from source to detector for a given number of rays. These are then imported to Matlab® and processed to yield the CIR.

4.5 Comparison with Existing Results for Empty Sea

4.5.1 Channel Impulse Response

First, as a sanity check, we consider the same underwater environment and parameters of [111] (see Table 23) and obtain the CIR under the assumption of OTHG. In [111], two lasers with 532 nm wavelengths and 10° divergence angle are located symmetrically on the *x*-axis of the transmit plane at -1 m and 1 m. Two photodetectors with 50 cm aperture diameter are placed 30 m away from transmitters on the *x*-axis of the receiver plane at -0.5 m and 0.5 m. Coastal water is assumed in this scenario and there are no objects within the environment. In Fig. 56, we present the computed CIR obtained through our methodology. The CIR of [111] is also included as a benchmark. Under the assumption that OTHG is used to model the SPF, it is observed that two CIRs are identical confirming the accuracy of our approach.

Table 23: Parameters of scenario in [111]

Number of transmitter	2
Number of receiver	2
Transmitter positions (m)	(1,0,15) (-1,0,15)
Receiver positions (m)	(0.5,0,-15) (-0.5,0,-15)
Link range (m)	30
Transmitter specifications	Power: 0.5 W Divergence angle: 10° Wavelength: 532 nm
Receiver specifications	Aperture diameter: 50 cm Field of view: 180°
Water type	Coastal ($C = 0.83$ mg/m^3)
Absorption, scattering and extinction coefficients (m^{-1})	0.088, 0.216, 0.305
Scattering phase function	OTHG
Average cosine of scattering angles	0.9470
Time resolution	0.1 ns

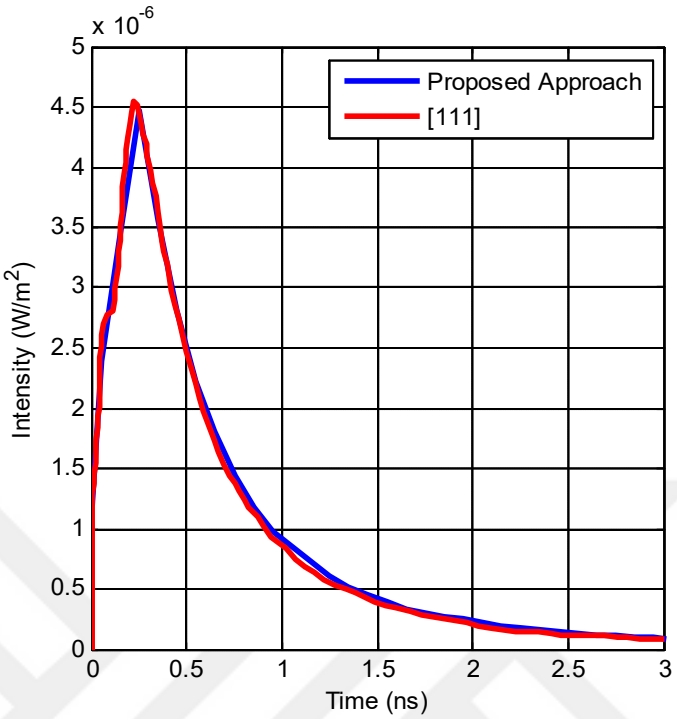

Figure 56: Comparison of the proposed approach with [111]

4.5.2 Path Loss

The path loss is a function of both attenuation loss and geometrical loss. For a collimated source such as a laser diode, geometrical loss is negligible; therefore, the path loss only depends on the attenuation loss. On the other hand, the effect of geometrical loss should be taken into account for the diffused and semi-collimated sources, i.e., LEDs and diffused laser diodes.

Attenuation losses can be calculated through well-known Beer Lambert law [131] or its modified version in [97]. According to Beer Lambert law, the attenuation loss is given by [131]

$$PL_{\mathrm{BL}} = 10\log_{10}\left(e^{-c(\lambda)d}\right) \tag{36}$$

where d is the link range between transmitter and receiver and $c(\lambda)$ is extinction

coefficient already defined in Section 4.3. As earlier noted, Beer-Lambert law builds upon two implicit assumptions. First, the transmitter and receiver are perfectly aligned. Second, all the scattered photons are lost even though in reality some of the scattered photons can still arrive at the receiver after multiple scattering events. To address the latter issue, a weighted function of two exponentials is proposed [97] as

$$PL_{\mathrm{MBL}} = 10\log_{10}\left(u_1 e^{-v_1 d} + u_2 e^{-v_2 d}\right) \tag{37}$$

where the weighting parameters u_1, u_2, v_1 and v_2 are calculated by the LMS fitting algorithm to the simulation data obtained from Monte Carlo method.

Geometrical loss occurs due to the spreading of the transmitted beam between the transmitter and the receiver. Considering LOS configuration and diffused/semi-collimated sources, geometrical loss can be given as

$$PL_{\mathrm{GL}} = 10\log_{10}\left(\frac{A_R(m+1)}{2\pi d^2}\cos^m(\phi)\right) \tag{38}$$

where A_R denotes the photodetector area, ϕ is the angle of irradiance and $m = -1/\log_2\left(\cos\left(\Phi_{1/2}\right)\right)$ is the order of Lambertian emission where $\Phi_{1/2}$ denotes the semi-angle of the light source. Based on (36-38), the overall path loss can be then determined as the summation of attenuation loss and geometrical loss.

We consider the scenario illustrated in Fig. 57 where the transmitter-receiver pair is placed at a depth of $h = 45$ m with $d = 20$ m distance apart in empty coastal water. The transmitter is selected as a Cree XR-E blue LED with non-ideal Lambertian distribution, a viewing angle of $\Phi = 60°$ and the full width at half maximum spectral of 450 nm-480 nm [132]. The FOV and aperture diameter of the detector are $FOV = 180°$ and $D_R = 5$ cm, respectively. All simulation parameters are summarized in Table 24. CIRs between transmitter and receiver are calculated with 1 meter distance apart. Path

loss is calculated based on (4) and presented in Fig. 58. As benchmarks, we include the path loss expressions calculated through (36-38). The coefficients u_1, u_2, v_1 and v_2 in (37) are respectively obtained as 1.183, -0.190, 0.072, and 0.164 for the scenario under consideration. It is observed from Fig. 58 that the path loss calculated through our approach is lower than that obtained through Beer Lambert law. This is expected since Beer Lambert law is known to overestimate the path loss. On the other hand, our results provide an excellent match with the weighted exponential function of [97].

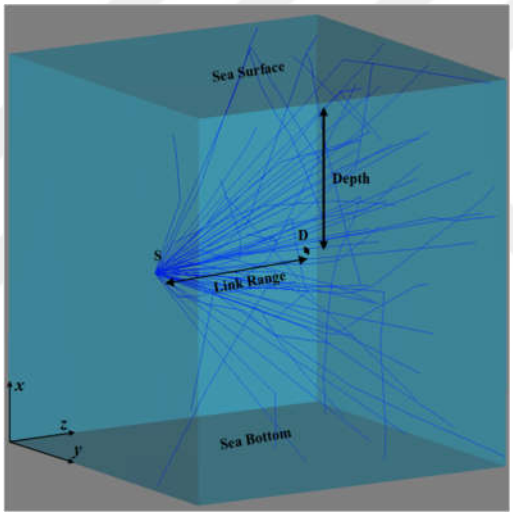

Figure 57: Link geometry in empty water environment

Table 24: Simulation parameters

Transmitter specifications	Power: 1 Watt LED brand: Super Blue Cree® XR-E [132] Viewing angle: 60° [132]
Receiver specifications	Aperture diameter: 5 cm [105] Field of view: 180° [105]
Link Range (m)	20
Depth (m)	45
Water type	Coastal- S_8 group (C_c: 0.8~2.2 mg/m^3) [124]
Absorption, scattering and extinction coefficients (m^{-1})	0.0508, 0.2116, 0.2624
Scattering phase function	OTHG
Mean cosine of scattering angles	0.9470

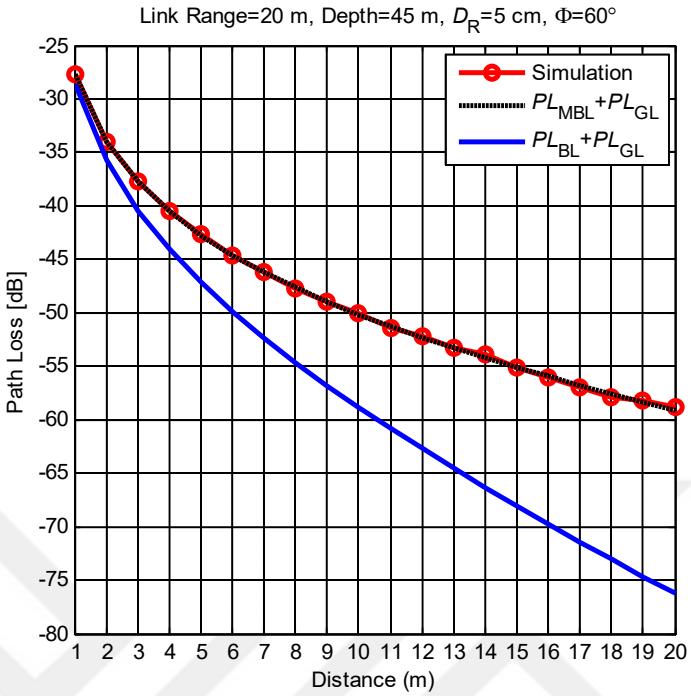

Figure 58: Path loss versus distance

4.6 Effect of Blocking and Shadowing

In this section, we present CIRs for more realistic underwater environments including divers, underwater vehicles etc and investigate the associated effects of shadowing and blocking. We assume that there are two divers who communicate with each other through UVLC link (see Fig. 59). The transmitter and receiver are placed in their hands. Unless otherwise stated, we use the simulation parameters provided in Table 24. In the following, we consider several cases to investigate the effect of human modeling, LOS blockage, transmitter/receiver specifications and water depth.

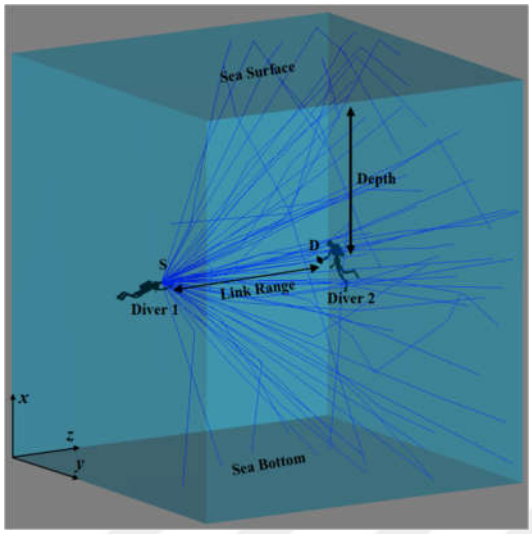

Figure 59: Link geometry for two divers who communicate with each other through UVLC link

To demonstrate the effect of human models, we consider a scenario with no blockage. Three cases are investigated as following. As the benchmark, empty water is considered (Case 1) where transmitter and receiver are placed as two floating nodes without the presence of humans in the environment. In Case 2, two divers are considered and modeled as absorbing objects. In Case 3, the coating materials of two divers are explicitly defined. Specifically, the coating materials of diver suit, diver glasses, and oxygen capsule are respectively modeled as black gloss paint, plexiglas and galvanized steel metal. The CIRs obtained for these three cases are illustrated in Fig. 60 while Table 25 lists all the relevant channel parameters. It is observed from Table 25 that the path losses in Cases 2 and 3 are respectively 59.11 dB and 58.79 dB which are more or less the same. Therefore, the simplifying assumption of absorbing material for human models and clothes can be made without losing accuracy. Since the transmitter and receiver are placed in diver's hands without any blockage between them, the path loss remains nearly the same as in empty water. On the other hand, the presence of human has some effect on RMS delay spread. In case of empty water, i.e., Case 1, the

RMS delay spread is 5.27 ns while this decreases to 3.22 ns and 3.89 ns for Cases 2 and 3, respectively. This is a result of the fact that the rays cannot pass through human bodies and terminated earlier than those rays in empty water.

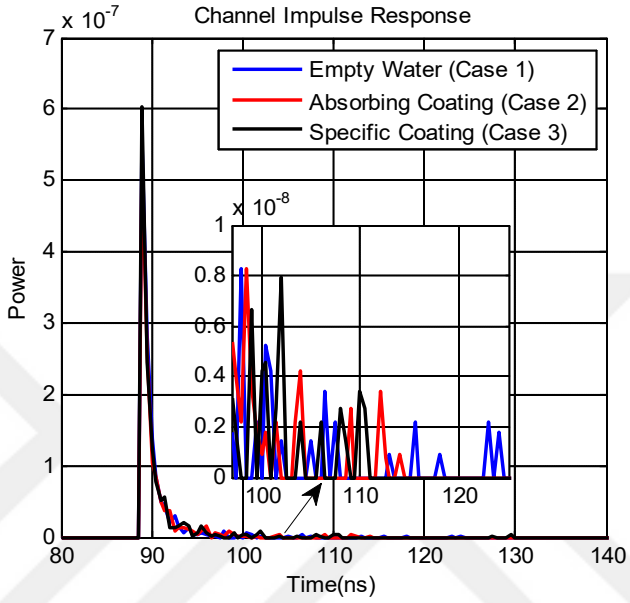

Figure 60: Effect of human models on CIR

Table 25: Channel parameters for the cases under consideration

	τ_{RMS} (ns)	H_0	PL(dB)
Case 1	5.27	1.30×10^{-6}	58.85
Case 2	3.22	1.22×10^{-6}	59.11
Case 3	3.89	1.31×10^{-6}	58.79
Case 4	6.28	1.35×10^{-6}	58.68
Case 5	6.77	5.91×10^{-7}	62.27
Case 6	8.22	2.73×10^{-7}	65.63
Case 7	5.71	4.90×10^{-7}	63.09
Case 8	3.44	7.64×10^{-7}	61.16
Case 9	2.26	8.08×10^{-7}	60.92
Case 10	2.17	7.81×10^{-7}	61.07
Case 11	2.14	4.84×10^{-7}	63.14
Case 12	7.88	1.34×10^{-6}	58.72
Case 13	7.08	5.00×10^{-6}	53.00
Case 14	5.42	4.06×10^{-7}	63.90
Case 15	11.25	1.73×10^{-7}	67.60

The objects present in the underwater environment are likely to result in LOS blockage. In this part, to demonstrate this effect, we consider a scenario where two divers communicate with each other while there is an AUV between them as illustrated in Fig. 61. As a benchmark, a LOS link with no obstructions is considered (Case 4). AUV is assumed to have a galvanized steel metal exterior and, based on its location, it either provides partial LOS blockage (Case 5) or complete LOS blockage (Case 6).

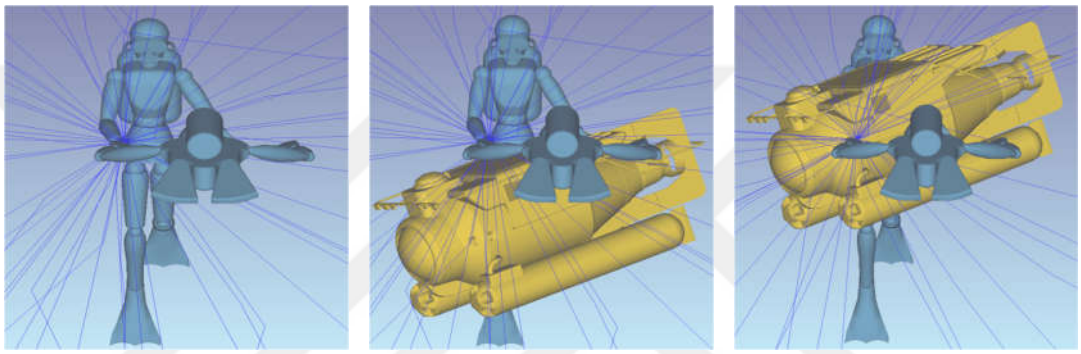

(a) (b) (c)

Figure 61: (a) Without LOS blockage, (b) partial LOS blockage and (c) complete LOS blockage

The associated CIRs are provided in Fig. 62. It is observed that the CIR is significantly affected by blockage. In case of complete LOS blockage, the channel DC gain decreases to 20% of the no blockage case (see Table 25). It should be however noted that the receiver still receives some signal due to scattering of light from particles. In terms of path loss, it is observed from Table 25 that the partial LOS blockage introduces an additional loss of 3.59 dB while this climbs to 6.95 dB for complete LOS blockage. Furthermore, as a result of scattered rays from obstructions, additional multipath components are introduced resulting in the increase of RMS delay spread.

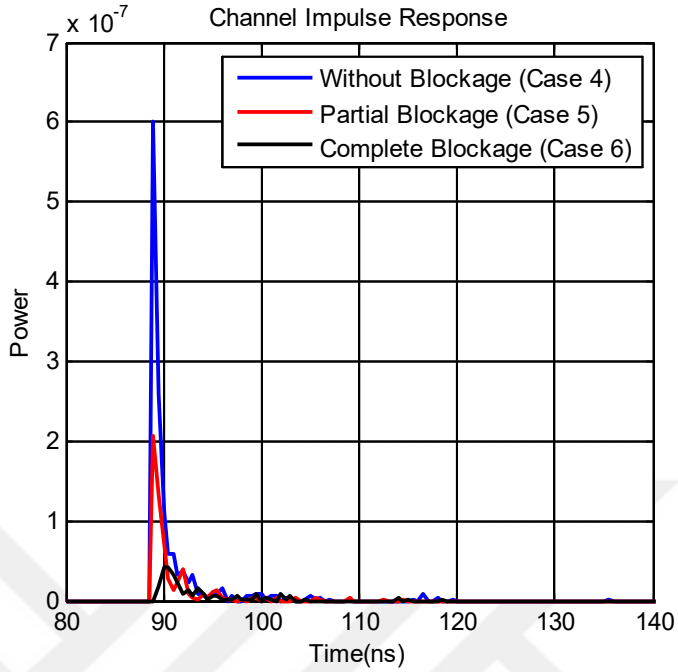

Figure 62: Effect of LOS blockage on CIR

In this part, we investigate the effect of transmitter viewing angles. Complete LOS blockage is assumed. In Fig. 63.a, we illustrate the CIRs assuming $\Phi = 40°$, 20°, and 10° (Case 7, Case 8 and Case 9). In comparison to $\Phi = 60°$ (which was earlier considered as Case 6 in Fig. 62), it is observed that decrease in LED viewing angles provide some gains. Specifically, path loss reductions of 2.54 dB, 4.47 dB and 4.71 dB are obtained for $\Phi = 40°$, $\Phi = 20°$ and $\Phi = 10°$, respectively. It is due to the fact that the focused beam has less attenuation through the water medium. It is also observed that RMS delay spread significantly decreases with decreased viewing angles. Specifically, delay spreads of 5.71 ns, 3.44 ns and 2.26 ns are observed for $\Phi = 40°$, $\Phi = 20°$ and $\Phi = 10°$, respectively.

As transmitter viewing angle gets smaller, the improvement in path loss cannot be sustained since the scattered rays are more likely to be blocked by obstruction. To demonstrate this, we illustrate CIRs in Fig. 63.b assuming $\Phi = 8°$ and 6° (Case 10 and

Case 11). With respect to Case 9 (i.e., $\Phi = 10°$), it is observed that $\Phi = 8°$ results in a loss of 0.15 dB while a loss of 2.22 dB is observed for $\Phi = 6°$. Therefore, $\Phi = 10°$ can be considered as the most appropriate value for the scenario under consideration.

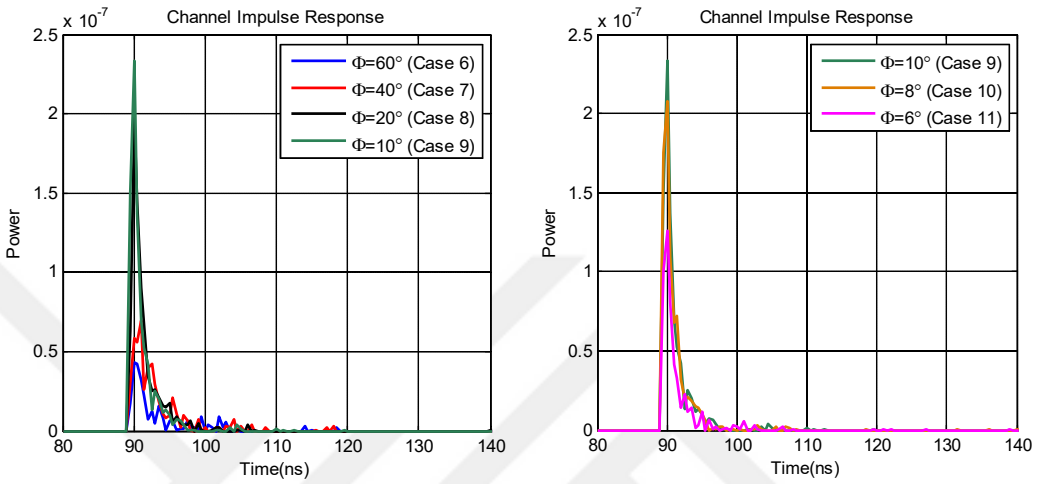

(a) (b)

Figure 63: Effect of transmitter viewing angles on CIR

In this part, we investigate the effect of receiver aperture size. Complete LOS blockage is assumed. In Fig. 64, we illustrate the CIRs for $D_R = 10$ cm and $D_R = 20$ cm (Case 12 and Case 13). In comparison to $D_R = 5$ cm (which was earlier considered as Case 6 in Fig. 62), it is observed that increased aperture diameters provide significant gains. Specifically 6.91 dB and 12.63 dB reductions in path loss are obtained for $D_R =$ 10 cm and $D_R = 20$ cm, respectively. It is also observed that RMS delay spread decreases with increased aperture diameters, specifically 0.34 ns and 1.14 ns for $D_R =$ 10 cm and $D_R = 20$ cm, respectively, since the rays are likely to reach earlier to a larger receiver due to less number of scattering.

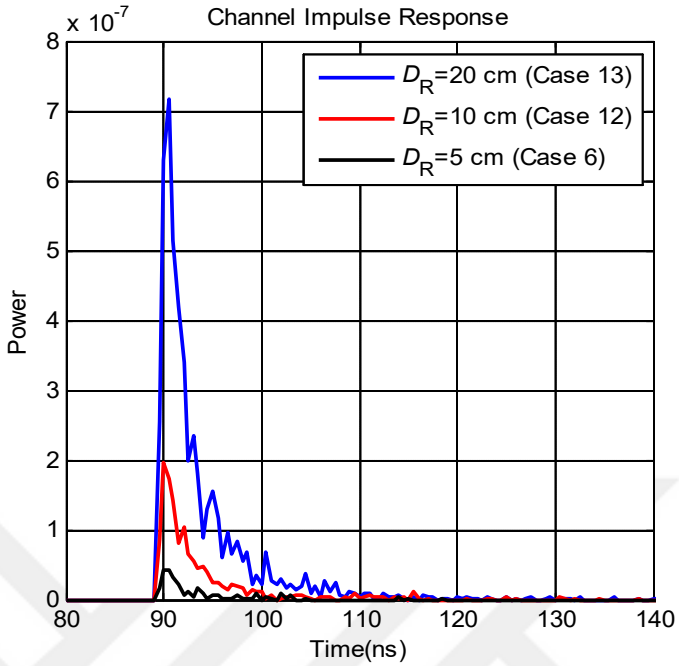

Figure 64: Effect of receiver aperture diameters on CIR

So far, we assumed a depth of 45 m which can be considered as mid-depth. In Fig. 65, we investigate the effect of depth. Based on the Haltrin & Kattawar model [123] and depth profiles of chlorophyll concentration [124], the absorption, scattering and extinction coefficients at depths of 2 m (Case 14) and 90 m (Case 15) are obtained as (0.1005, 0.3505, 0.4510) and (0.0292, 0.0556, 0.0848), respectively. It is observed that the path loss at sea surface is 63.90 dB indicating a reduction of 1.73 dB over that experienced at mid-depth. This is a result of the fact that the detector receives more specular reflected rays from the sea surface. On the other hand, the path loss at sea bottom is 67.60 dB indicating an additional loss of 1.97 dB over that experienced at mid-depth. This is a result of the fact that the rays are attenuated by diffusely reflecting from sea bottom.

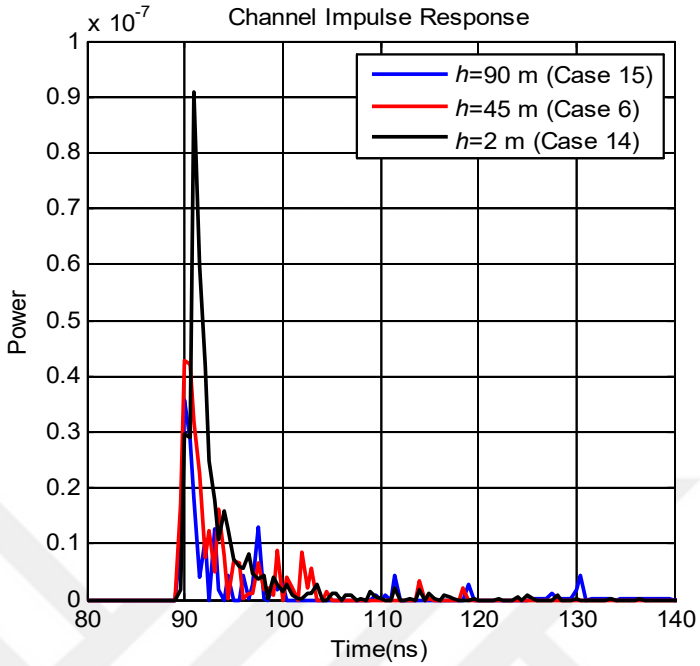

Figure 65: Effect of depths on CIR

4.7 UVLC Path Loss Model

So far, we focused on obtaining CIRs for a given underwater environment. The CIRs provide a full description of the channel, but require detailed information of the underwater environment. In this section, we aim to develop a closed-form path loss expression as a function of system parameters.

As discussed in detail in Section 4.5.2, the UVLC path loss is a function of both attenuation loss and geometrical loss. Considering LOS configuration and for a semi-collimated laser source with a Gaussian beamshape, geometrical loss can be approximated as [133]

$$PL_{\mathrm{GL}}(d) \approx 10\log_{10}\left(\left(\frac{D_R}{\theta_{1/e} d}\right)^2\right) \tag{39}$$

where $\theta_{1/e}$ is full width transmitter beam divergence angle[1]. Based on (36) and (39) and for a given wavelength λ, the overall path loss is then found as the summation of attenuation loss and geometrical loss, i.e.,

$$\begin{aligned} PL(d) &= PL_{\mathrm{BL}}(d) + PL_{\mathrm{GL}}(d) \\ &\approx 10\log_{10}\left(\left(\frac{D_R}{\theta_{1/e}d}\right)^2 e^{-cd}\right) \end{aligned} \tag{40}$$

In practice, the detector can receive the rays after multiple scattering while the above formulation assumes that the scattered rays are lost. To take into account the contribution of scattered rays, we propose a modified version of (40) as [22]

$$PL(d) = 10\log_{10}\left(\left(\frac{D_R}{\theta_{1/e}d}\right)^2 e^{-cd\left(\frac{D_R}{\theta_{1/e}d}\right)^T}\right) \tag{41}$$

where an additional term proportional to the geometrical propagation of the light source is introduced in the negative exponential. In (41), T is a coefficient found via data fitting to ray tracing simulation data. We carry out a comprehensive simulation study to validate the proposed expression in (41).

In Fig. 66, we consider pure sea, clear ocean, coastal water and harbor water as water types. Their extinction coefficients are respectively given by 0.056 m^{-1}, 0.150 m^{-1}, 0.305 m^{-1} and 2.170 m^{-1}. We assume $\theta_{1/e} = 6°$, $D_R = 5$ cm and $FOV = 180°$ in our simulations. Corresponding T values are found as 0, 0.05, 0.13 and 0.31 for pure sea, clear ocean, coastal water and harbor water, respectively.

[1] Full width transmitter beam divergence angle is measured at which the beam intensity drops to $1/e$ of its peak value.

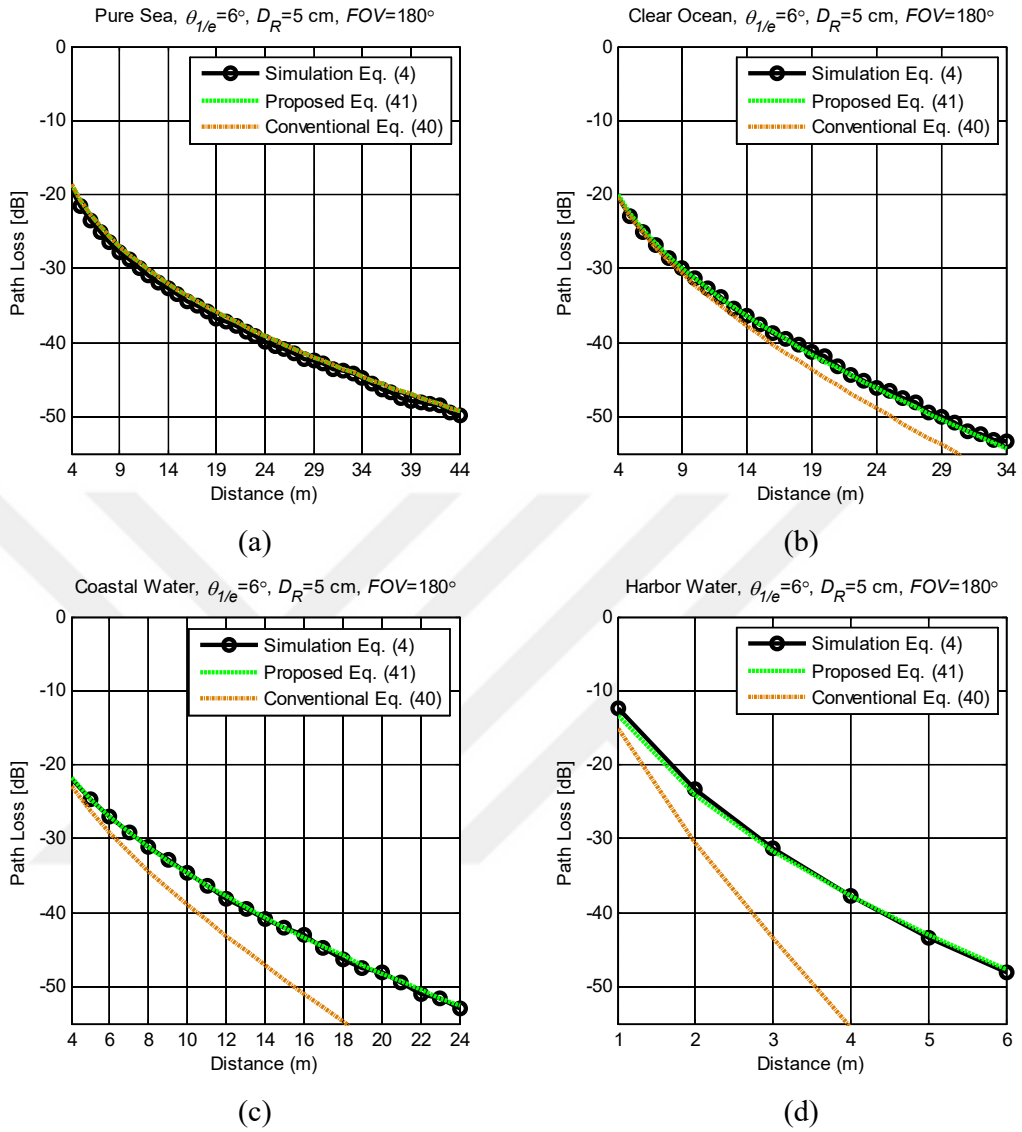

Figure 66: Comparison of path loss expression with simulation results for different water types

The proposed closed-form expression in (41) provides a "good fit"[2] with simulation data for all water types under consideration. On the other hand, (40) matches simulation results only for pure sea and deviates for other water types. In fact, it can be readily verified that for pure sea (i.e., $T = 0$), the proposed expression in (41) becomes identical to (40). Since the extinction coefficient of pure sea is very small (i.e., $c =$

[2] As a statistical measure of how close the simulation data are to the fitted line, we adopt R-squared [134]. A good fit is obtained R-squared is larger than 0.95 [112].

0.056 m^{-1}), the scattered photons are negligible at the receiver and Beer-Lambert formula is valid. For other water types, Beer-lambert formula overestimates the attenuation loss since it ignores the scattered photons. We also observe that T increases with increase in turbidity of the water and takes its maximum value for harbor water where the extinction coefficient is the largest among the four water types under consideration.

Table 26: Configurations under consideration

Configuration		System Parameters	*T*
1	**Effect of receiver aperture diameter**	$\theta_{1/e}=6°,\ D_R=5\,\text{cm},\ FOV=180°$	0.13
2		$\theta_{1/e}=6°,\ D_R=10\,\text{cm},\ FOV=180°$	0.16
3		$\theta_{1/e}=6°,\ D_R=20\,\text{cm},\ FOV=180°$	0.21
4		$\theta_{1/e}=6°,\ D_R=30\,\text{cm},\ FOV=180°$	0.26
5		$\theta_{1/e}=6°,\ D_R=40\,\text{cm},\ FOV=180°$	0.31
6		$\theta_{1/e}=6°,\ D_R=50\,\text{cm},\ FOV=180°$	0.37
7	**Effect of beam divergence angle**	$\theta_{1/e}=6°,\ D_R=20\,\text{cm},\ FOV=180°$	0.21
8		$\theta_{1/e}=12°,\ D_R=20\,\text{cm},\ FOV=180°$	0.24
9		$\theta_{1/e}=18°,\ D_R=20\,\text{cm},\ FOV=180°$	0.25
10	**Effect of field of view**	$\theta_{1/e}=6°,\ D_R=5\,\text{cm},\ FOV=60°$	0.13
11		$\theta_{1/e}=6°,\ D_R=5\,\text{cm},\ FOV=120°$	0.13
12		$\theta_{1/e}=6°,\ D_R=5\,\text{cm},\ FOV=180°$	0.13

In the following, we assume coastal water and investigate the effect of receiver aperture diameter, beam divergence angle and field of view. The system configurations under consideration are listed in Table 26. In Fig. 67, we consider the configurations 1-6 where we set $\theta_{1/e}=6°$ and $FOV=180°$ while varying the receiver aperture diameter. For receiver aperture diameters smaller than or equal to 30 cm, it is observed that the proposed closed-form expression in (41) provides a good fit with the ray tracing simulation data. For larger receiver aperture diameters, overestimation and underestimation are observed for small and large distances, respectively. It can be also

observed from Table 26 that the value of T increases when the aperture diameter increases.

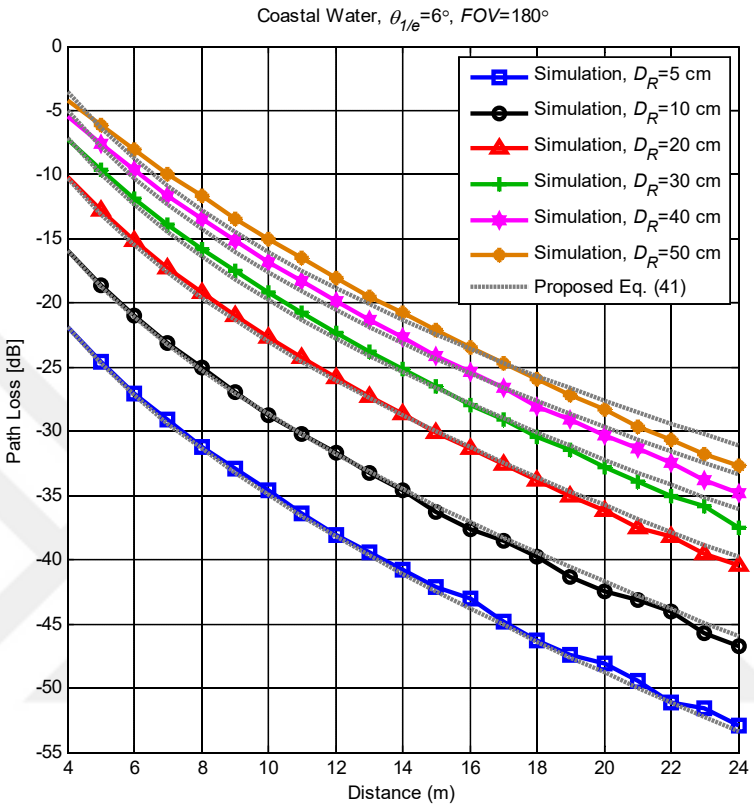

Figure 67: Comparison of path loss expression with simulation results (Configurations 1-6 assuming different receiver aperture diameters)

In Fig. 68, we consider the configurations 7-9 where we set $D_R = 20$ cm and $FOV = 180°$ while varying the beam divergence angle. In general, we observe a good fit between our expression in (41) and simulation data for configurations under consideration. It should be also noted that the proposed expression is obtained through the underlying assumption of semi-collimated source where the beam divergence angle is smaller than $\pi/10$ (i.e., 18°) [135]. It is also observed from Table 26 that the value of T increases when the beam divergence angle increases.

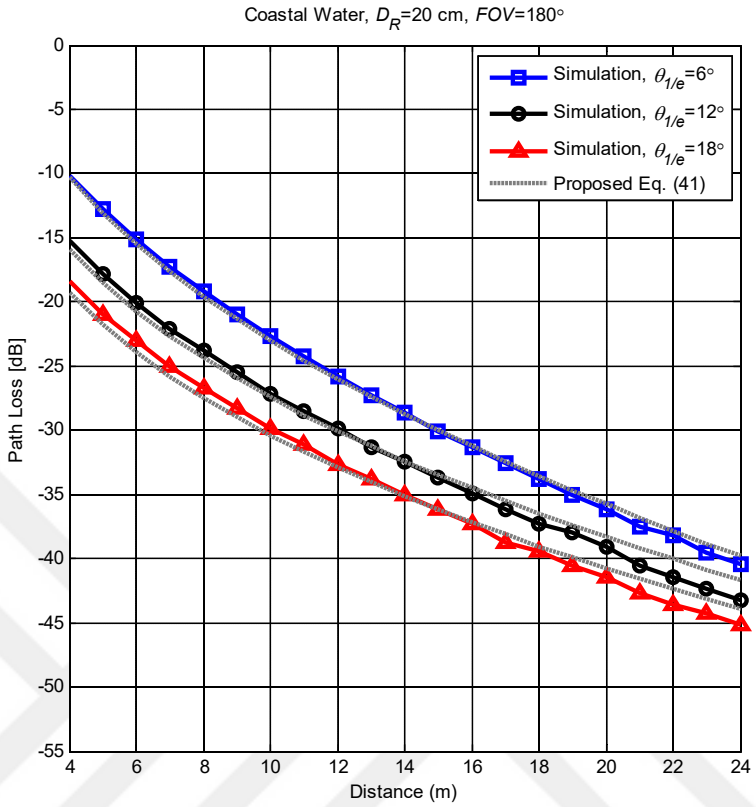

Figure 68: Comparison of path loss expression with simulation results (Configurations 7-9 assuming different beam divergence angles)

In Fig. 69, we consider the configurations 10-12 where we have $\theta_{1/e} = 6°$ and $D_R = 5$ cm and vary the receiver field of view. Coastal water is assumed. Based on the R-squared values, it can be concluded that the proposed closed-form expression in (41) provides a good fit with simulation data. It is also observed from Table 26 that the value of T is independent of receiver field of view.

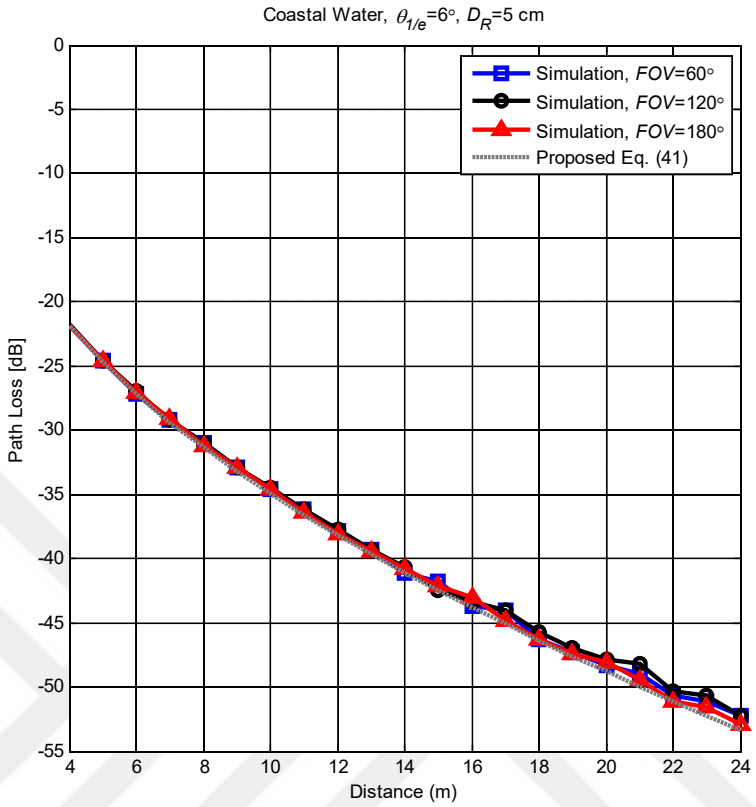

Figure 69: Comparison of path loss expression with simulation results (Configurations 10-12 assuming different field of views)

CHAPTER V

CONCLUSIONS

In this dissertation, we proposed a realistic VLC channel modeling approach based on a commercial optical and illumination design software called Zemax®. Taking advantage of the advanced ray tracing features of this software, we were able to obtain realistic CIRs which take into account practical issues such as wavelength dependency of reflection coefficients and different types of reflections (diffuse, specular and mixed cases of diffuse and specular). We were also able to integrate commercial light sources instead of ideal Lambertian sources typically used in existing works and obtain CIRs with higher order number of reflections.

In Chapter II, to confirm the accuracy of our approach, we first demonstrated that our approach yields the same CIR as in [24] under the assumption of purely diffuse reflections and ideal Lambertian source. We then discussed the effect of specular and mixed cases. Our results demonstrated that the presence of specular components create fluctuations in CIR and result in deviations from the purely diffuse case. Furthermore, we demonstrated the importance of taking into account higher order of reflections particularly for specular cases.

We further investigated the effect of varying distance between transmitter and receiver on channel parameters and obtained closed form expressions for channel DC gain and RMS delay spread as a function of distance. Our results showed that the received power decreases in a negative exponential manner resulting in the decrease of channel DC gain. It is also observed that RMS delay spread first increases then

decreases with the increasing distance. Comparison of results obtained for IR and VL further reveals that DC gains and RMS delay spread of VL channels are smaller than those in IR channels for same configurations. We finally demonstrated the effect of transmitter specifications (i.e., single vs. multiple transmitters), receiver specifications (i.e., location, rotation) and objects within the environment (i.e., furniture) on the CIR.

We also presented an overview of reference VLC channel models adopted by the IEEE 802.15.7r1. These channel models are based on four indoor scenarios, namely workplace (open office floor and cubicles), office room with secondary light, living room, and manufacturing cell. For each scenario, the CIRs were presented along with a discussion on fundamental channel characteristics such as delay spread and DC gain. These channels exhibit frequency selectivity and, furthermore, their characteristics are highly location dependent.

We have developed a mobile VLC channel based on non-sequential ray tracing. For realistic modeling, wavelength dependency was explicitly taken into account while different types of reflections (i.e., diffuse, specular and mixed reflections) were considered. Commercially available measured light source and an indoor environment with furniture and CAD human models were used in our simulations. Under these realistic assumptions, we have obtained CIRs over the user movement trajectories and presented expressions for path loss and delay spread. Our results demonstrated that the received power varies significantly based on the user location.

In Chapter III, we presented a realistic vehicular VLC channel modeling approach for the practical ITS usage scenarios by taking advantages of the advanced ray tracing. We obtained realistic CIRs which take into account practical issues such as wavelength dependency of reflection coefficients and different types of reflections

(diffuse, specular and mixed cases of diffuse and specular). We were also able to integrate commercial and practical light sources (i.e., headlamps, traffic lights and street lamps) instead of ideal Lambertian sources typically used in indoor environments. We further considered various configurations, i.e., vehicle-to-vehicle, traffic light-to-vehicle and street lamp-to-vehicle. For each configuration, we obtained CIRs and presented a channel characterization study where channel parameters, such as channel DC gain, RMS delay spread and path loss are obtained. From the derived channel impulse responses, it is observed that the common property of the CIRs was composed of dominant multiple LOS links and a less number of NLOS delay taps.

Building on non-sequential ray tracing, we have precisely taken into account the asymmetrical intensity distribution of automotive headlights and road reflection model and developed a closed-form path loss expression for V2V VLC channel for different weather conditions.

In Chapter IV, we have carried out a detailed underwater optical channel modeling and characterization study taking into account the presence of human and man-made objects such as AUV. The objects present in the underwater environment are likely to result in LOS blockage. Our results have demonstrated that, even in complete LOS blockage, transmission can take place due to scattering despite the increase in path loss. Such losses can be recovered by using smaller transmitter viewing angles or larger aperture sizes. However, there is also some trade-off between performance improvement and viewing angle. As the angle gets smaller, the improvement in path loss cannot be sustained since the scattered rays are also likely to be blocked by obstruction. Our results have also demonstrated that the path loss decreases at sea surface compared to that experienced at mid-depth. This is a result of the fact that the detector receives more specular reflected rays from the sea surface. On the other hand,

the path loss at sea bottom increases compared to that experienced at mid-depth since the rays are attenuated by diffusely reflecting from sea bottom.

We further developed a closed-form path loss expression as an explicit function of water type, beam divergence angle and receiver aperture diameter and validated the accuracy of the proposed expression through Monte Carlo simulation results.

APPENDIX

Chlorophyll Concentration Depth Profile

The chlorophyll profile over a depth $z(m)$ from the surface $C_c(z)$ can be modeled as a Gaussian curve [128]

$$C_c(z) = B_0 + Sz + \frac{h}{\sigma\sqrt{2\pi}} \exp\left[\frac{-(z - z_{\max})^2}{2\sigma^2}\right]$$
$$\sigma = \frac{h}{\sqrt{2\pi}\left[C_{chl}(z_{\max}) - B_0 - Sz_{\max}\right]} \tag{A.1}$$

A difficulty arises in determining the value of these parameters because for each surface concentration of chlorophyll, the profile shape alters. However, an experimental study in [129] quantified 2419 separate chlorophyll profiles [129]. Based on this data, ocean locations were categorized in nine groups, each representing a different range of surface chlorophyll concentrations. These were <0.04 mg⁄m^3, 0.04-0.08 mg⁄m^3, 0.08-0.12 mg⁄m^3, 0.12-0.2 mg⁄m^3, 0.2-0.3 mg⁄m^3, 0.3-0.4 mg⁄m^3, 0.4-0.8 mg⁄m^3, 0.8-2.2 mg⁄m^3, and 2.2-4 mg⁄m^3, represented by S1-S9, respectively. A full list of the parameters for each of these concentration ranges is given in [124]. The S1-S7 are related to pure sea and open ocean while S8-S9 are related to coastal and harbor. The chlorophyll concentration depth profiles of these nine groups are depicted in Fig. A.1.

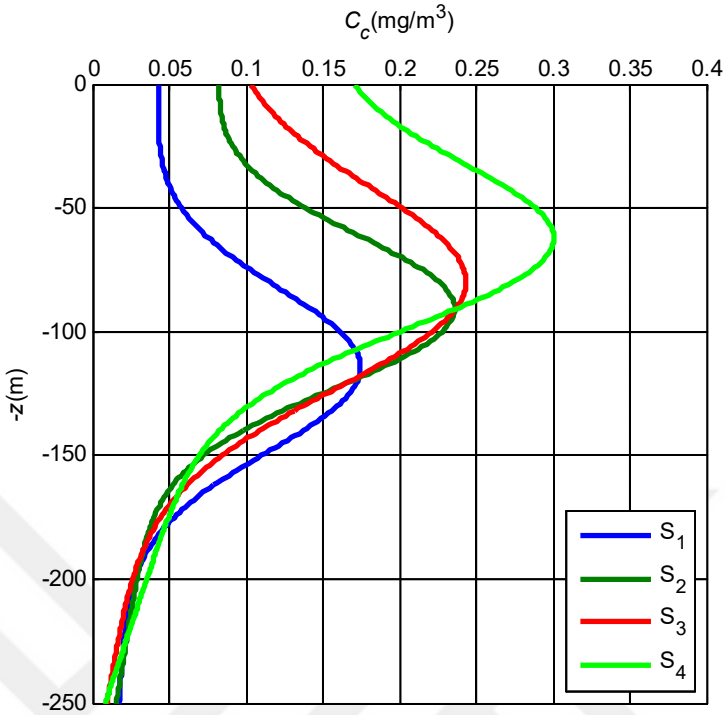

(a)

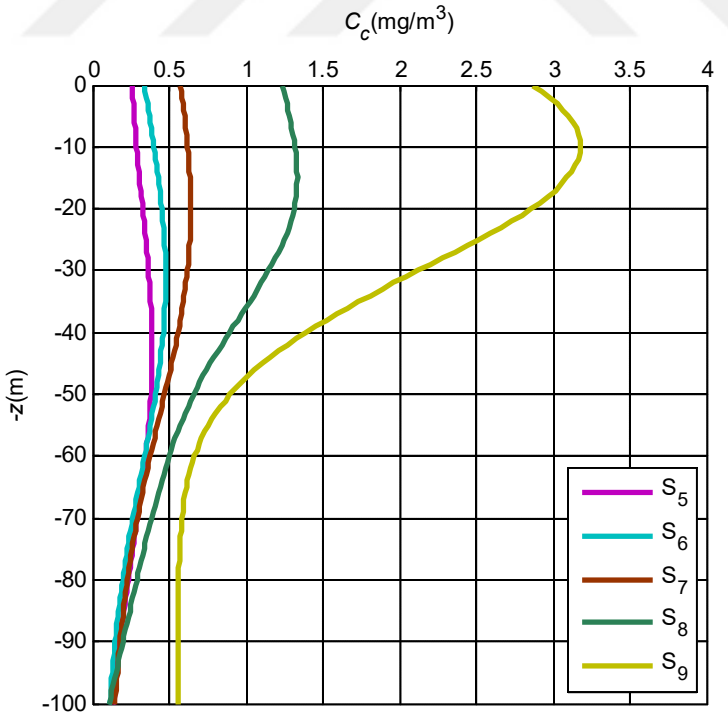

(b)

Figure A.1: Chlorophyll concentration depth profiles (a) S1-S4 and (b) S5-S9

REFERENCES

[1] Cisco White Paper, "Cisco visual networking index: Global mobile data traffic forecast update, 2016-2021", Feb. 2017.

[2] M. Agiwal, A. Roy, and N. Saxena, "Next generation 5G wireless networks: A comprehensive survey," *IEEE Commun. Surveys Tut.*, vol. 18, no. 3, pp. 1617-1655, Aug. 2016.

[3] M. Uysal, C. Capsoni, Z. Ghassemlooy, A. Boucouvalas, and E. Udvary, *Optical wireless communications: an emerging technology*, Springer, 2016.

[4] M. Uysal, Z. Ghassemlooy, A. Bekkali, A. Kadri and H. Menouar, "Visible light communication for vehicular networking: performance study of a V2V system using a measured headlamp beam pattern model," *IEEE Veh. Technol. Mag.*, vol. 10, no. 4, pp. 45-53, Dec. 2015.

[5] F. J. Martinez, C. K. Toh, J. C. Cano, C. T. Calafate, and P. Manzoni, "Emergency services in future intelligent transportation systems based on vehicular communication networks," *IEEE Intell. Transp. Syst. Mag.*, vol. 2, no. 2, pp. 6-20, 2010.

[6] A. M. Meroth, F. Trankle, B. F. Richter, M. Wagner, M. Neher, and J. Luling, "Functional safety and development process capability for intelligent transportation systems," *IEEE Intell. Transp. Syst. Mag.*, vol. 7, no. 4, pp. 12-23, 2015.

[7] O. Karagiannis, O. Altintas, E. Ekici, G. Heijenk, B. Jarupan, K. Lin, and T. Weil, "Vehicular networking: A survey and tutorial on requirements, architectures, challenges, standards and solutions," *IEEE Commun. Surveys Tut.*, vol. 13, no. 4, pp. 584-616, 2011.

[8] K. Zheng, Q. Zheng, P. Chatzimisios, W. Xiang, and Y. Zhou, "Heterogeneous vehicular networking: a survey on architecture, challenges, and solutions," *IEEE Commun. Surveys Tut.*, vol. 17, no. 4, pp. 2377-2396, 2015.

[9] "Intelligent transport systems (ITS) usage in ITU Member States, Working Document toward a Preliminary Draft New Report ITU-R M. [ITS USAGE], Annex 32 to Document 5A/469-E," Jun. 2017.

[10] H. Kaushal, and G. Kaddoum, "Underwater optical wireless communication," *IEEE Access*, vol. 4, pp. 1518-1547, 2016.

[11] Z. Zeng, S. Fu, H. Zhang, Y. Dong, and J. Cheng, "A survey of underwater optical wireless communications," *IEEE Commun. Surveys Tuts.*, vol. 19, no. 1, pp. 204-238, 2017.

[12] F. Miramirkhani, M. Uysal, and E. Panayirci, "Novel channel models for visible light communications", Invited Paper, *SPIE Photonics West*, San Francisco, California, United States, Feb. 2015.

[13] F. Miramirkhani, and M. Uysal, "Channel modeling and characterization for visible light communications", *IEEE Photonics Journal*, vol. 7, no. 6, pp. 1-16, Dec. 2015.

[14] M. Uysal, and F. Miramirkhani, "Channel modeling for visible light communications", doc: IEEE 802.15-15/0352r1, May 2015. [Online]. Available: https://mentor.ieee.org/802.15/dcn/15/15-15-0352-01-007a-channel-modeling-for-visible-light-communications.pptx

[15] M. Uysal, and F. Miramirkhani, "LiFi reference channel models: Office, home, and hospital", doc: IEEE 802.15-15/0514r1, Jul. 2015. [Online]. Available: https://mentor.ieee.org/802.15/dcn/15/15-15-0514-01-007a-lifi-reference-channel-models-office-home-hospital.pptx

[16] M. Uysal, F. Miramirkhani, T. Baykas, N. Serafimovski, and V. Jungnickel, "LiFi channel models: Office, home and manufacturing cell", doc: IEEE 802.15-15/0685r0, Sept. 2015. [Online]. Available: https://mentor.ieee.org/802.15/dcn/15/15-15-0685-00-007a-lifi-reference-channel-models-office-home-manufacturing-cell.pdf

[17] M. Uysal, T. Baykas, F. Miramirkhani, N. Serafimovski, and V. Jungnickel, "TG7r1 channel model document for high-rate PD communications", doc: IEEE 802.15-15/0746r1, Sept. 2015. [Online]. Available: https://mentor.ieee.org/802.15/dcn/15/15-15-0746-01-007a-tg7r1-channel-model-document-for-high-rate-pd-communications.pdf

[18] M. Uysal, F. Miramirkhani, O. Narmanlioglu, T, Baykas, and E. Panayirci, "IEEE 802.15.7r1 reference channel models for visible light communications", *IEEE Communications Magazine*, vol. 55, no. 1, pp. 212-217, Jan. 2017.

[19] F. Miramirkhani, O. Narmanlioglu, M. Uysal, and E. Panayirci, "A mobile channel model for VLC and application to adaptive system design", *IEEE Communications Letters*, vol. 21, no. 5, pp. 1035-1038, May 2017.

[20] M. Elamassie, M. Karbalayghareh, F. Miramirkhani, R. C. Kizilirmak, and M. Uysal, "Effect of fog and rain on the performance of vehicular visible light communications", *IEEE 87th Vehicular Technology Conference* (VTC2018-Spring), Porto, Portugal, Jun. 2018.

[21] F. Miramirkhani, and M. Uysal, "Visible light communication channel modeling for underwater environments with blocking and shadowing", *IEEE Access*, vol. 6, no. 1, pp. 1082-1090, 2018.

[22] M. Elamassie, F. Miramirkhani, and M. Uysal, "Channel modeling and performance characterization of underwater visible light communications", *IEEE 4th Workshop on Optical Wireless Communications* (co-located with IEEE ICC'18), Kansas City, MO, USA, May 2018.

[23] F. R. Gfeller, and U. Bapest, "Wireless in-house data communication via diffuse infrared radiation," *Proc. IEEE*, vol. 67, no. 11, pp. 1474-1485, 1979.

[24] J. R. Barry, J. M. Kahn, W. J. Krause, E. A. Lee, and D. G. Messerschmitt, "Simulation of multipath impulse response for wireless optical channels," *IEEE J. Sel. Areas Commun.*, vol. 11, no. 3, pp. 367-379, 1993.

[25] F. J. Lopez-Hermandez, and M. J. Betancor, "DUSTIN: Algorithm for calculation of impulse response on IR wireless indoor channels," *IEEE Electronics Lett.*, vol. 33, no. 21, pp. 1804-1806, 1997.

[26] M. Abtahi, and H. Hashemi, "Simulation of indoor propagation channel at infrared frequencies in furnished office environments," In *6th IEEE Int. Symp. Pers. Indoor and Mobile Radio Communications (PIMRC) Wireless: Merging onto the Information Superhighway*, pp. 306-310, 1995.

[27] J. B. Carruthers, and P. Kannan, "Iterative site-based modeling for wireless infrared channels," *IEEE Trans. Antennas Propag.*, vol. 50, no. 5, pp. 759-765, 2002.

[28] J. B. Carruthers, and J. M. Kahn, "Modeling of nondirected wireless infrared channels," *IEEE Trans. Commun.*, vol. 45, no. 10, pp. 1260-1268, 1997.

[29] V. Jungnickel, V. Pohl, S. Nonnig, and C. Von Helmolt, "A physical model of the wireless infrared communication channel," *IEEE J. Sel. Areas Commun.*, vol. 20, no. 3, pp. 631-640, 2002

[30] N. Hayasaka, and T. Ito, "Channel modeling of nondirected wireless infrared indoor diffuse link," *Electronics and Communications in Japan (Part I: Communications)*, vol. 90, no. 6, pp. 9-19, 2007.

[31] F. J. Lopez-Hernandez, R. Perez-Jimeniz, and A. Santamaria, "Monte Carlo calculation of impulse response on diffuse IR wireless indoor channels," *IEEE Electron. Lett.*, vol. 34, no. 12, pp. 1260-1262, Jun. 1998.

[32] F. J. Lopez-Hernandez, R. Perez-Jimenez, and A. Santamaria, "Modified Monte Carlo scheme for high-efficiency simulation of the impulse response on diffuse IR wireless indoor channels," *IEEE Electron. Lett.*, vol. 34, no. 19, pp. 1819-1820, Sept. 1998.

[33] S. Dimitrov, R. Mesleh, H. Haas, M. Cappitelli, M. Olbert, and E. Bassow, "On the SIR of a cellular infrared optical wireless system for an aircraft," *IEEE J. Sel. Areas Commun.*, vol. 27, no. 9, pp. 1623-1638, 2009.

[34] M. S. Chowdhury, W. Zhang, and M. Kavehrad, "Combined deterministic and modified monte carlo method for calculating impulse responses of indoor optical wireless channels." *J. Lightwave Technol.*, vol. 32, no. 18, pp. 3132-3148, 2014.

[35] H. Q. Nguyen, J. H. Choi, M. Kang, Z. Ghassemlooy, D. H. Kim, S. K. Lim, T. G. Kang, and C. G. Lee, "A MATLAB-based simulation program for indoor visible light communication system," In *7th IEEE Int.*

Symp. Communication Systems Networks and Digital Signal Processing (CSNDSP), pp. 537-540, July 2010.

[36] S. Long, M. A. Khalighi, M. Wolf, S. Bourennane, and Z. Ghassemlooy, "Channel characterization for indoor visible light communications," *IEEE 3rd Int. Workshop on Optical Wireless Communications (IWOW)*, pp.75-79, Sept. 2014.

[37] K. Lee, H. Park, and J. R. Barry, "Indoor channel characteristics for visible light communications," *IEEE Commun. Lett.*, vol. 15, no. 2, pp. 217-219, Feb. 2011.

[38] J. Ding, I. Chih-Lin, and Z. Xu, "Indoor optical wireless channel characteristics with distinct source radiation patterns," *IEEE Photon. J.*, vol. 8, no. 1, pp. 1-15, 2016.

[39] H. Schulze, "Frequency-domain simulation of the indoor wireless optical communication channel," *IEEE Trans. Commun.*, vol. 64, no. 6, pp. 2551-2562, 2016.

[40] C. Chen, D. Basnayaka, and H. Haas, "Non-line-of-sight channel impulse response characterization in visible light communications," In *IEEE Int. Conf. Communications (ICC)*, pp. 1-6, May 2016.

[41] A. Al-Kinani, C. X. Wang, H. Haas, and Y. Yang, "Characterization and modeling of visible light communication channels," In *IEEE 83rd Vehicular Technology Conf. (VTC Spring)*, pp. 1-5, May 2016.

[42] A. Al-Kinani, C. X. Wang, H. Haas, and Y. Yang, "A geometry-based multiple bounce model for visible light communication channels," In *IEEE Wireless Communications and Mobile Computing Conf. (IWCMC)*, pp. 31-37, Sept. 2016.

[43] S. P. Rodriguez, R. P. Jimenez, B. R. Mendoza, F. J. L. Hernandez, and A. J. A. Alfonso, "Simulation of impulse response for indoor visible light communications using 3D CAD models," *EURASIP Journal on Wireless Communications and Networking*, 2013:7, pp. 1-10, 2013.

[44] J. Rufo, J. Rabadan, V. Guerra, and R. Perez-Jimenez, "BRDF models for the impulse response estimation in indoor optical wireless channels, *IEEE Photon. Technol. Lett.*, vol. 29, no. 17, pp.1431-1434, 2017.

[45] H. S. Lee, "A photon modeling method for the characterization of indoor optical wireless communication," *Progress In Electromagnetics Research*, vol. 92, pp. 121-136, 2009.

[46] "Zemax OpticStudio optical design software illumination design software". http://www.zemax.com/opticstudio

[47] "ASTER Spectral Library - Version 2.0," [Online]. Available at: http://speclib.jpl.nasa.gov.

[48] "CREE LEDs," [Online]. Available at: http://www.cree.com.

[49] "OSRAM LEDs," [Online]. Available at: http://www.osram-os.com.

[50] A. Sivabalan, and J. John, "Modeling and simulation of indoor optical wireless channels: a review," In *IEEE Conference on Convergent Technologies for the Asia-Pacific Region (TENCON)*, vol. 3, pp.1082-1085, Oct. 2003.

[51] O. Gonzalez, C. Militello, S. Rodriguez, R. Prez-Jimenez, and A. Ayala, "Error estimation of the impulse response on diffuse wireless infrared indoor channels using a Monte Carlo ray-tracing algorithm," *IEE P. Optoelectron.*, vol. 149, no. 56, pp. 222-227, 2002.

[52] W. H. Press, S. A. Teukolsky, W. T. Vetterling, and B. P. Flannery, *Numerical Recipes*, Cambridge Press, 2007.

[53] "Zemax® 13 Release 2, Radiant Zemax® LLC," www.zemax.com/ support/ knowledgebase/ understanding Sobol sampling.

[54] M. S. Varela, M. G. Sanchez, "RMS delay and coherence bandwidth measurements in indoor radio channels in the UHF band," *IEEE Trans. Veh. Technol.*, vol. 50, no. 2, pp. 515-525, 2001.

[55] Z. Ghassemlooy, D. Wu, M. A. Khalighi, X. Tang, "Indoor non-directed optical wireless communications optimization of the Lambertian order," *Journal of Electrical and Computer Engineering Innovations*, vol. 1, no. 1, pp. 1-9, May 2013.

[56] TG7r1, "Technical considerations document", doc: IEEE 802.15-15/0492r3, July. 2015. [Online]. Available: https://mentor.ieee.org/802.15/dcn/15/15-15-0492-03-007a-technical-considerations-document.docx.

[57] "Lighting of indoor work places", *International Standard. ISO 8995:2002 CIE S 008/E-2001*.

[58] R. C. Kizilirmak, O. Narmanlioglu, and M. Uysal, "Relay-assisted OFDM-based visible light communications," *IEEE Trans. Commun.*, vol. 63, no. 10, pp. 3765-3778, 2015.

[59] T. Komine, and M. Nakagawa, "A study of shadowing on indoor visible-light wireless communication utilizing plural white LED lightings," In *1st Int. Symp. Wireless Commun. Systems*, pp.36-40, 2004.

[60] T. Komine, S. Haruyama, and M. Nakagawa, "A study of shadowing on indoor visible-light wireless communication utilizing plural white LED lightings," *Wireless Personal Communications*, vol. 34, no. 1-2, pp. 211-225, 2005.

[61] Y. Xiang, M. Zhang, M. Kavehrad, M. S. Chowdhury, M. Liu, J. Wu, and X. Tang, "Human shadowing effect on indoor visible light communications channel characteristics," *Opt. Eng.*, vol. 53, no. 8, pp. 086113-086113, 2014.

[62] P. Chvojka, S. Zvanovec, P. A. Haigh, Z. Ghassemlooy, "Channel characteristics of visible light communications within dynamic indoor environment," *J. Lightwave Technol.*, vol. 33, no. 9, pp. 1719-1725, May 2015.

[63] G. James, D. Witten, T. Hastie, and R. Tibshirani, *An introduction to statistical learning*, vol. 6. New York: Springer, 2013.

[64] D. Karunatilaka, F. Zafar, V. Kalavally, and R. Parthiban, "LED based indoor visible light communications: state of the art," *IEEE Commun. Surveys Tuts.*, vol. 17, no. 3, pp. 1649-78, 2015.

[65] P. H. Pathak, X. Feng, P. Hu, and P. Mohapatra, "Visible light communication, networking, and sensing: A survey, potential and challenges," *IEEE Commun. Surveys Tuts.*, vol. 17, no. 4, pp. 2047-2077, 2015.

[66] S. H. Yu, O. Shih, H. M. Tsai, N. Wisitpongphan, and R. Roberts, "Smart automotive lighting for vehicle safety," *IEEE Commun. Mag.*, vol. 51, no. 12, pp. 50-59, 2013.

[67] A. M. Cailean, and M. Dimian, "Impact of IEEE 802.15. 7 standard on visible light communications usage in automotive applications," *IEEE Commun. Mag.*, vol. 55, no. 4, pp. 169-175, 2017.

[68] M. Akanegawa, Y. Tanaka, and M. Nakagawa, "Basic study on traffic information system using LED traffic lights," *IEEE Trans. Intell. Transp. Syst.*, vol. 2, no. 4, pp. 197-203, 2001.

[69] S. Kitano, S. Haruyama, and M. Nakagawa, "LED road illumination communications system," In *IEEE 58th Vehicular Technology Conference (VTC Fall)*, pp. 3346-3350, 2003.

[70] N. Kumar, L. N. Alves, and R. L. Aguiar, "Design and analysis of the basic parameters for traffic information transmission using VLC," In *First Int. Conf. Wireless Communication, Vehicular Technology, Information Theory and Aerospace & Electronic Systems Technology, (Wireless VITAE)*, pp. 798-802, 2009.

[71] N. Kumar, D. Terra, N. Lourenco, L. N. Alves, and R. L. Aguiar, "Visible light communication for intelligent transportation in road safety applications," in *Proc. IEEE Int. conf. Wireless Communications and Mobile Computing*, pp. 1513-1518, 2011.

[72] S. J. Lee, J. K. Kwon, S. Y. Jung, and Y. H. Kwon, "Simulation modeling of visible light communication channel for automotive applications," In *15th International IEEE Conference on Intelligent Transportation Systems (ITSC)*, pp. 463-468, 2012.

[73] S. J. Lee, J. K. Kwon, S. Y. Jung, and Y. H. Kwon, "Evaluation of visible light communication channel delay profiles for automotive applications," *EURASIP Journal on Wireless Communications and Networking*, 2012:370, pp. 1-8, 2012.

[74] W. Viriyasitavat, S. H. Yu, and H. M. Tsai, "Short paper: Channel model for visible light communications using off-the-shelf scooter taillight," In *IEEE Vehicular Networking Conference (VNC)*, pp. 170-173, 2013.

[75] P. Luo, Z. Ghassemlooy, H. L. Minh, E. Bentley, A. Burton, and X. Tang, "Fundamental analysis of a car to car visible light communication

system," In *9th International Symposium on Communication Systems, Networks & Digital Signal Processing (CSNDSP)*, pp. 1011-1016, 2014.

[76] P. Luo, Z. Ghassemlooy, H. Le Minh, E. Bentley, A. Burton, and X. Tang, "Performance analysis of a car-to-car visible light communication system," *Appl. Opt.*, vol. 54, no. 7, pp. 1696-1706, 2015.

[77] H. Y. Tseng, Y. L. Wei, A. L. Chen, H. P. Wu, H. Hsu, and H. M. Tsai, "Characterizing link asymmetry in vehicle-to-vehicle visible light communications," In *IEEE Vehicular Networking Conference (VNC)*, pp. 88-95, 2015.

[78] B. Turan, S. Ucar, S. C. Ergen, and O. Ozkasap, "Dual channel visible light communications for enhanced vehicular connectivity," In *IEEE Vehicular Networking Conference (VNC)*, pp. 84-87, 2015.

[79] B. Turan, O. Narmanlioglu, S. C. Ergen, and M. Uysal, "Broadcasting brake lights with MIMO-OFDM based vehicular VLC," In *IEEE Vehicular Networking Conference (VNC)*, pp. 1-7, 2016.

[80] B. Turan, O. Narmanlioglu, S. C. Ergen, and M. Uysal, "Physical layer implementation of standard compliant vehicular VLC," In *IEEE 84th Vehicular Technology Conference (VTC-Fall)*, pp. 1-5, 2016.

[81] J. H. Yoo, J. S. Jang, J. K. Kwon, H. C. Kim, D. W. Song, and S. Y. Jung, "Demonstration of vehicular visible light communication based on LED headlamp," *Int. J. Auto. Tech-Kor.*, vol. 17, no. 2, pp. 347-352, 2016.

[82] A. L. Chen, H. P. Wu, Y. L. Wei, and H. M. Tsai, "Time variation in vehicle-to-vehicle visible light communication channels," In *IEEE Vehicular Networking Conference (VNC)*, pp. 1-8, 2016.

[83] K. Siddiqi, A. D. Raza, and S. S. Muhammad, "Visible light communication for V2V intelligent transport system," In *IEEE Int. Conf. Broadband Communications for Next Generation Networks and Multimedia Applications (CoBCom)*, pp. 1-4, 2016.

[84] H. Luan, X. Jin, W. Liu, M. Jin, and Z. Xu, "Demonstration of a real-time vehicular visible light communication system with timing recovery," In *IEEE 13th Int. Wireless Communications and Mobile Computing Conference (IWCMC)*, pp. 472-477, 2017.

[85] A. Memedi, H. M. Tsai, and F. Dressler, "Impact of realistic light radiation pattern on vehicular visible light communication," In *Proc. IEEE Global Telecommunications Conference (GLOBECOM 2017)*, Singapore, Dec. 2017.

[86] Y. H. Kim, W. A. Cahyadi, and Y. H. Chung, "Experimental demonstration of LED-based vehicle to vehicle communication under atmospheric turbulence," In *IEEE Int. Conf. Information and Communication Technology Convergence (ICTC)*, pp. 1143-1145, 2015.

[87] Y. H. Kim, W. A. Cahyadi, and Y. H. Chung, "Experimental demonstration of VLC-based vehicle-to-vehicle communications under fog conditions," *IEEE Photon. J.*, vol. 7, no. 6, pp. 1-9, 2015.

[88] I. E. Lee, M. L. Sim, and F. W. L. Kung, "Performance enhancement of outdoor visible light communication system using selective combining receiver," *IET Optoelectron.*, vol. 3, no. 1, pp. 30-39. 2009.

[89] K. Cui, G. Chen, Z. Xu, and R. D. Roberts, "Traffic light to vehicle visible light communication channel characterization," *Appl. Opt.*, vol. 51, no. 27, pp. 6594-6605, 2012.

[90] D. Schulz, V. Jungnickel, S. Das, J. Hohmann, J. Hilt, P. Hellwig, A. Paraskevopoulos, and R. Freund, "Long-term outdoor measurements using a rate-adaptive hybrid optical wireless/60 GHz link over 100 m," In *IEEE 19th Int. Conf. Transparent Optical Networks (ICTON)*, pp. 1-4, 2017.

[91] R. E. Stark, "Road surface's reflectance influences lighting design," *Light. Design Appl.*, 1986.

[92] "Excellence Opto. Inc.," http://www.eoi.com.tw/

[93] "LUMILEDS LEDs," https://www.lumileds.com/

[94] *Agreement Addendum 111: Regulation No. 112 Revision 3-unece*, 2013.

[95] S. Arnon, and D. Kedar, "Non-line-of-sight underwater optical wireless communication network," *JOSA A*, vol. 26, no. 3, pp. 530-539, 2009.

[96] T. Hamza, M. A. Khalighi, S. Bourennane, P. Léon, and J. Opderbecke, "Investigation of solar noise impact on the performance of underwater wireless optical communication links," *Opt. express*, vol. 24, no. 22, pp. 25832-25845, 2016.

[97] C. Wang, H. Y. Yu, and Y. J. Zhu, "A long distance underwater visible light communication system with single photon avalanche diode," *IEEE Photon. J.*, vol. 8, no. 5, pp. 1-11, 2016.

[98] S. Jaruwatanadilok, "Underwater wireless optical communication channel modeling and performance evaluation using vector radiative transfer theory," *IEEE J. Sel. Areas Commun.*, vol. 26, no. 9, pp. 1620-1627, 2008.

[99] Y. Dong, S. Tang, and X. Zhang, "Effect of random sea surface on downlink underwater wireless optical communications," *IEEE Commun. Lett.*, vol. 17, no. 11, pp. 2164-2167, 2013.

[100] C. Li, K. H. Park, and M. S. Alouini, "On the use of a direct radiative transfer equation solver for path loss calculation in underwater optical wireless channels," *IEEE Wireless Commun. Lett.*, vol. 4, no. 5, pp. 561-564, 2015.

[101] H. Zhang, Y. Dong, and X. Zhang, "On stochastic model for underwater wireless optical links," in *Proc. IEEE/CIC Int. Conf. Communications in China (ICCC'14)*, Shanghai, China, pp. 156-160, Oct. 2014.

[102] H. Zhang, and Y. Dong, "General stochastic channel model and performance evaluation for underwater wireless optical links," *IEEE Trans. Wireless Commun.*, vol. 15, no. 2, pp. 1162-1173, 2016.

[103] J. Liu, Y. Dong, and H. Zhang, "On received intensity for misaligned underwater wireless optical links," In *OCEANS 2016-Shanghai*, pp. 1-4, 2016.

[104] Y. Zhou, and Y. Dong, "Single scattering impulse response modeling of underwater wireless optical channels," In *OCEANS 2016-Shanghai*, pp. 1-4, 2016.

[105] C. Gabriel, M. A. Khalighi, S. Bourennane, P. Léon, and V. Rigaud, "Channel modeling for underwater optical communication," in *Proc. IEEE Global Communication Conf. (GLOBECOME'11)*, pp. 833-837, Dec. 2011.

[106] J. Li, Y. Ma, Q. Zhou, B. Zhou, and H. Wang, "Monte Carlo study on pulse response of underwater optical channel," *Opt. Eng.*, vol. 51, no. 6, pp. 066001-1, 2012.

[107] C. Gabriel, M. A. Khalighi, S. Bourennane, P. L´eon, and V. Rigaud, "Monte-Carlo-based channel characterization for underwater optical communication systems," *IEEE/OSA J. Opt. Commun. Netw.*, vol. 5, no. 1, pp. 1-12, 2013.

[108] S. Tang, Y. Dong, and X. Zhang, "On path loss of NLOS underwater wireless optical communication links," In *Proc. MTS/IEEE OCEANS (OCEANS'13)*, Bergen, Norway, pp. 1-3, 2013.

[109] V. Guerra, *et al.*, "Parallelization of a Monte carlo ray tracing algorithm for channel modelling in underwater wireless optical communications," *Procedia Technology*, vol. 7, pp. 11-19, 2013.

[110] V. Guerra, *et al.*, "Statistical study of the channel parameters in underwater wireless optical links," In *IEEE Int. Work Conf. Bio-inspired Intelligence (IWOBI)*, pp. 124-127, 2014.

[111] Y. Dong, H. Zhang, and X. Zhang, "On impulse response modeling for underwater wireless optical MIMO links," in *Proc. IEEE/CIC Int. Conf. Communications in China (ICCC'14)*, pp. 151-155, Oct. 2014.

[112] S. Tang, Y. Dong, and X. Zhang, "Impulse response modeling for underwater wireless optical communication links," *IEEE Trans. Commun.*, vol. 62, no. 1, pp. 226-234, 2014.

[113] W. Liu, D. Zou, P. Wang, Z. Xu, and L. Yang, "Wavelength dependent channel characterization for underwater optical wireless communications," in *IEEE Int. Conf. Signal Processing, Communications and Computing (ICSPCC'14)*, pp. 895-899, Aug. 2014.

[114] A. S. Fletcher, S. A. Hamilton, and J. D. Moores, "Undersea laser communication with narrow beams," *IEEE Commun. Mag.*, vol. 53, no. 11, pp. 49-55, 2015.

[115] C. J. Funk, "Multiple scattering calculations of light propagation in ocean water," *Appl. Opt.*, vol. 12, no. 2, pp. 301-313, 1973.

[116] F. Hanson, and S. Radic, "High bandwidth underwater optical communication," *Appl. Opt.*, vol. 47, no. 2, pp. 277-283, 2008.

[117] S. Arnon, J. Barry, G. Karagiannidis, R. Schober, and M. Uysal, *Advanced optical wireless communication systems*, Cambridge, U. K.: Cambridge Univ. Press, 2012.

[118] C. Mobley, "A numerical model for the computation of radiance distributions in natural waters with wind-roughened surfaces," *Limnol. Oceanogr.*, vol. 34, no. 8, pp. 1473-1483, 1989.

[119] R. W. Preisendorfer, "Eigenmatrix representations of radiance distributions in layered natural waters with wind-roughened surfaces," Technical Report, Paciffic Marine Environmental Laboratory-NOAA, Seatle, WA, Jan. 1988.

[120] T. S. Garrison, *Essentials of oceanography*, 5th ed., Cengage Learning, 2008.

[121] G. Karleskint, R. Turner, and J. Small, *Introduction to marine biology*, 3rd ed., Cengage Learning, 2009.

[122] C. D. Mobley, *Light and Water: Radiative transfer in natural waters*, Academic Press, June 1994.

[123] V. I. Haltrin, "Chlorophyll-based model of seawater optical properties," *Appl. Opt.*, vol. 38, no. 33, pp. 6826-6832, 1999.

[124] L. J. Johnson, R. J. Green, and M. S. Leeson, "Underwater optical wireless communications: depth dependent variations in attenuation," *Appl. Opt.*, vol. 52, no. 33, pp.7867-7873, 2013.

[125] A. Bricaud, M. Babin, A. Morel, and H. Claustre, "Variability in the chlorophyll-specific absorption coefficients of natural phytoplankton: analysis and parameterization," *J. Geophys.*, Res.100, pp. 13321-13332 1995.

[126] C. Pontbriant, *et al.*, "Diffuse high-bandwidth optical communications," *OCEANS*, pp. 1-4, 2008.

[127] C. Mobley, E. Boss, and C. Roesler, *Ocean optics web book*, 2010.

[128] T. Kameda and S. Matsumura, "Chlorophyll biomass off Sanriku, Northwestern Pacific, estimated by Ocean Color and Temperature Scanner (OCTS) and a vertical distribution model," *J. Oceanogr.*, vol. 54, no. 5, pp. 509-516, 1998.

[129] J. Uitz, H. Claustre, A. Morel, and S. B. Hooker, "Vertical distribution of phytoplankton communities in open ocean: an assessment based on surface chlorophyll," *J. Geophys.*, Res. 111, no. C8, 2006.

[130] L. C. Henyey, and J. L. Greenstein, "Diffuse radiation in the galaxy," *Astrophys. J.*, vol. 93, pp. 70-83, 1941.

[131] C. D. Mobley, *et al.*, "Comparison of numerical models for computing underwater light fields," *Appl. Opt.*, vol. 32, no. 36, pp. 7484-7504, 1993.

[132] B. Tian, F. Zhang, and X. Tan, "Design and development of an LED-based optical communication system for autonomous underwater robots,"

In *IEEE/ASME Int. Conf. Advanced Intelligent Mechatronics (AIM)*, pp. 1558-1563, 2013.

[133] J. Poliak, P. Pezzei, E. Leitgeb, and O. Wilfert, "Link budget for high-speed short-distance wireless optical link," In *8th IEEE Int. Symp. Communication Systems, Networks & Digital Signal Processing (CSNDSP)*, pp. 1-6, July 2012.

[134] P. Dangeti, *Statistics for machine learning*, Packt Publishing, 2017.

[135] S. Arnon, "Underwater optical wireless communication network," *Opt. Eng.*, vol. 49, no. 1, pp. 015001, 2010.

VITA

Farshad Miramirkhani received the B.Sc. and the M.Sc. degree with high honors in electronics and communication engineering from University of Isfahan, Isfahan, Iran, in 2011 and 2014, respectively. He joined Communication Theory and Technologies (CT&T) Research Group as a research assistant working toward his doctorate under supervision of Prof. Murat Uysal at Ozyegin University, Istanbul, Turkey, in 2014. He received his PhD degree in Electrical and Electronics Engineering in June 2018. His research interests include optical wireless communications, indoor visible light communications, underwater visible light communications, vehicular visible light communications and channel modeling.